ABSTRACT

Title of Thesis: FIREBRAND PILE THERMAL CHARACTERIZATION AND IGNITION STUDY OF FIREBRAND EXPOSED WESTERN RED CEDAR

Joseph Anthony Alascio, Master of Science, 2021

Thesis Directed By: Dr. Stanislav Stoliarov, Associate Professor, Department of Fire Protection Engineering

Over the past several decades, the severity of wildfires across the world has grown, resulting in increased number of structures in the Wildland–Urban Interface being destroyed, and lives lost. An ignition pathway that has been identified to contribute to most structures destroyed during a wildland fire is that of firebrand ignition. Firebrands are small burning pieces of vegetative material that are lofted ahead of the fire front. This study seeks to quantify thermal conditions experienced by building materials exposed to accumulated firebrands and to identify conditions that lead to ignition of these materials. A bench scale wind tunnel was used to house a decking material, western red cedar, on which the firebrands were deposited, which allowed for testing at different air flow velocities, while simultaneously analyzing the temperature of the solid substrate and gaseous exhaust flow constituents to identify trends in flaming and smoldering combustion. Higher peak temperatures and larger heating rates were found with the exposure of a higher air flow velocity. An increased air flow velocity also allowed for quicker, more frequent, and longer sustained flaming of the firebrand pile. A Modified Combustion Efficiency (MCE) value of 0.81 ± 0.02 for the firebrand pile across all testing conditions was quantified, which is indicative of a hybrid–smoldering/flaming combustion mode.

FIREBRAND PILE THERMAL CHARACTERIZATION AND IGNITION STUDY OF FIREBRAND EXPOSED WESTERN RED CEDAR

by

Joseph Anthony Alascio

Thesis submitted to the Faculty of the Graduate School of the
University of Maryland, College Park, in partial fulfillment
of the requirements for the degree of
Master of Science
2021

Advisory Committee:
Professor Stanislav I. Stoliarov, Ph.D., Chair
Professor Peter B. Sunderland, Ph.D.
Isaac T. Leventon, Ph.D.

Dedication

I dedicate this work to my ever–loving parents who supported me and were always proud, no matter how hard I was being on myself. Mom, you are an incredibly strong and caring woman who always puts others first. You taught me kindness, how to filter out distractions while staying focused on a goal, and how to stay goofy when I should not be. Dad, you taught me how to be a professional–mature child in a world full of adults. No matter how messed up a situation was, you showed me how to make the best out of it. I am overwhelmingly proud to call you the person that I look up to and wish that I become at least half the man you are.

You both deserve the universe. Thank you two for raising me exactly the way you did, I would not be who I am today without your guidance and love you have giving me over the past 24 years. I will always cherish the memories I have of us.

Acknowledgements

I would first like to acknowledge and thank the Department of Fire Protection Engineering for awarding me with the 2020 John L. Bryan Graduate Research Assistantship. This award allowed me to not only work on this project, but to also advance my education to a graduate level. The opportunity is something I will always be grateful for.

Secondly, I would like to thank Dr. Stanislav Stoliarov for giving me the privilege to work with him. He not only gave me insight and guidance throughout this study, but also had the patience to teach me what is just a sliver of the vast knowledge he possesses. He cares not only about the work he does, but also the people he is doing it with.

Thank you to my committee members, Dr. Isaac Leventon and Dr. Peter Sunderland for their time in reviewing this work. It is an amazing opportunity having you both as professors. Thank you to Dushyant, Conor, Ryan, Will, and Lucas for keeping the office a fun, engaging, and wholesome environment; at least for the little time that we were all together.

Another man who deserves his own personal acknowledgment is Jacques De Beer. Thank you for allowing me to work with you on this amazing project. You are a talented, driven young man who I am glad to call a colleague and a friend. Thank you for teaching me everything that you have and for not getting annoyed, at least noticeably, every time I leaned over and said, “Hey Jacques.”

Lastly, I would like to acknowledge all the professors I have had over my six–year collegiate journey between Anne Arundel Community College (AACC) and the University of Maryland, College Park (UMD). Before college, I was not one for academia. I was always late to high school classes, and never really cared for learning. After my first year at AACC, I fell in love with science and gained a passion for higher level learning. I still to this day do not know what jumped–started this infatuation; However, I do know for sure that the reason why my passion for learning will always be there, is because of every professor I have ever had.

Table of Contents

List of Tables

List of Figures

Nomenclature

Abbreviations

WUI	Wildland–Urban Interface
NIFC	National Interagency Fire Center
MC	Moisture Content
RH	Relative Humidity
O_2	Oxygen
WRC	Western Red Cedar
OSB	Oriented Strand Board
CO	Carbon Monoxide
CO_2	Carbon Dioxide
H_2O	Water
WC–HFG	Water–cooled Heat Flux Gauge
TSC	Thin–skin Calorimeter
TC	Thermocouple
HRR	Heat Release Rate
MCE	Modified Combustion Efficiency
NDIR	Non–Dispersive Infrared
IR	Infrared
CAPA II	Controlled Atmosphere Pyrolysis Apparatus II
Re	Reynolds number
N_2	Nitrogen
CH_4	Methane

Greek symbol

ϵ	Emissivity [–]
λ	Wavelength [nm]
ρ	Density [g m^{-3}]
ϕ	Volumetric Fraction [–]
χ	Molar Fraction [–]
Δ	Change in

Chapter 1: Introduction

1.1 Background

1.1.1 The Wildland–Urban Interface: Definition and Problem

The Wildland–Urban Interface (WUI) is defined as the zone of transition between developed community structures and undeveloped wildland areas including all the vegetative fuels found in these undeveloped areas [1]. The Federal Register of the United States delegates three types of communities within the WUI [2]. The first being an interface community with structures directly adjacent to wildland fuels, with a clear line of demarcation between structures and wildland fuels. Second, a more intermixed community where structures are scattered or secluded within the wildland area, with no clear line of demarcation, and wildland fuels are continuous in and outside of developed areas. Finally, an occluded community, which is one with a large amount of wildland fuels bordered by an urban landscape (i.e., large parks or grassy canyons). Due to the proximity of structures to the combustible–vegetative fuels [3], the building materials of these structures are susceptible to ignition during a WUI fire event [4].

Data studies by the National Interagency Fire Center (NIFC) indicate that, over the last 30 years, the number of annual wildfires in the United States of America has slightly decreased, however the number of acres burned have increased [5]. This increase can be attributed to the accumulation and over population of vegetative fuels due to fire exclusion movements, like Smokey the Bear [6]. The accumulation of the natural vegetative fuels then increases the fire load on the floor of these wildland areas, illustrated in Figure 1.

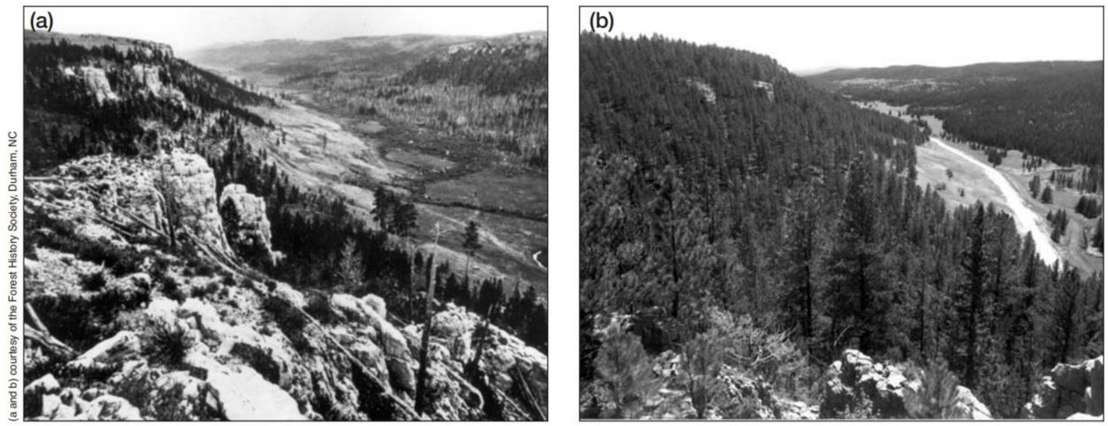

Figure 1: (a) Photograph by William H. Illingworth of Castle Creek Valley in South Dakota (1874). Held by the South Dakota State Historical Society. (b) Repeat photograph of Castle Creek Valley taken by Richard H. Sowell (1974) near the same position. These photos show an increase in natural vegetative fuels in a given area due to 100 years of fire exclusion [6].

The altered conditions can then increase the likelihood of a surface fire transitioning into a crown fire, examples shown in Figure 2, which can increase the amount of burned area when these fires occur [8]. Coupled with this increase in the number of burned acres of wildland vegetative fuels, the number of structures that have been destroyed during wildland fire events per year has increased [5]. Figure 3 depicts a map of structures lost to wildland fires in the United States, Alaska, and Hawaii from 1999 – 2011 reported in the ICS–209 database [9]. As of September 13th, 2021, the 'Dixie Fire' has burned over 960,470 acres, destroyed 1,329 structures, killed 1 person, and has become the second largest WUI fire in the state's history [10]. The 'Camp Fire' was the most destructive California fire to date, when considering the number of structures lost during a single wildland fire event. This fire resulted in 85 deaths, burned through 153,336 acres, and destroyed 18,804 structures [11]. In June 2012, the Waldo Canyon fire in Colorado Springs burned through 18,247 acres, destroyed 346 homes in the Mountain Shadows community, and killed two people, resulting in the worst fire in the history of Colorado State [12, 13].

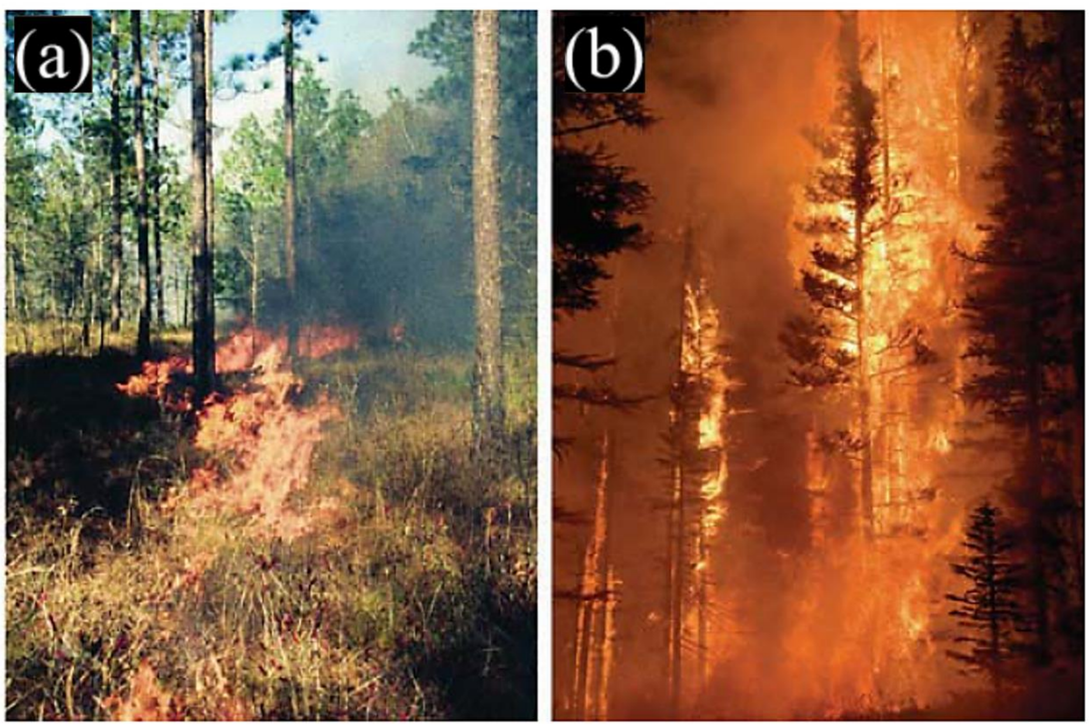

Figure 2: Photo examples of surface (a) and crown (b) fires found during Wildland–Urban Interface fires [7].

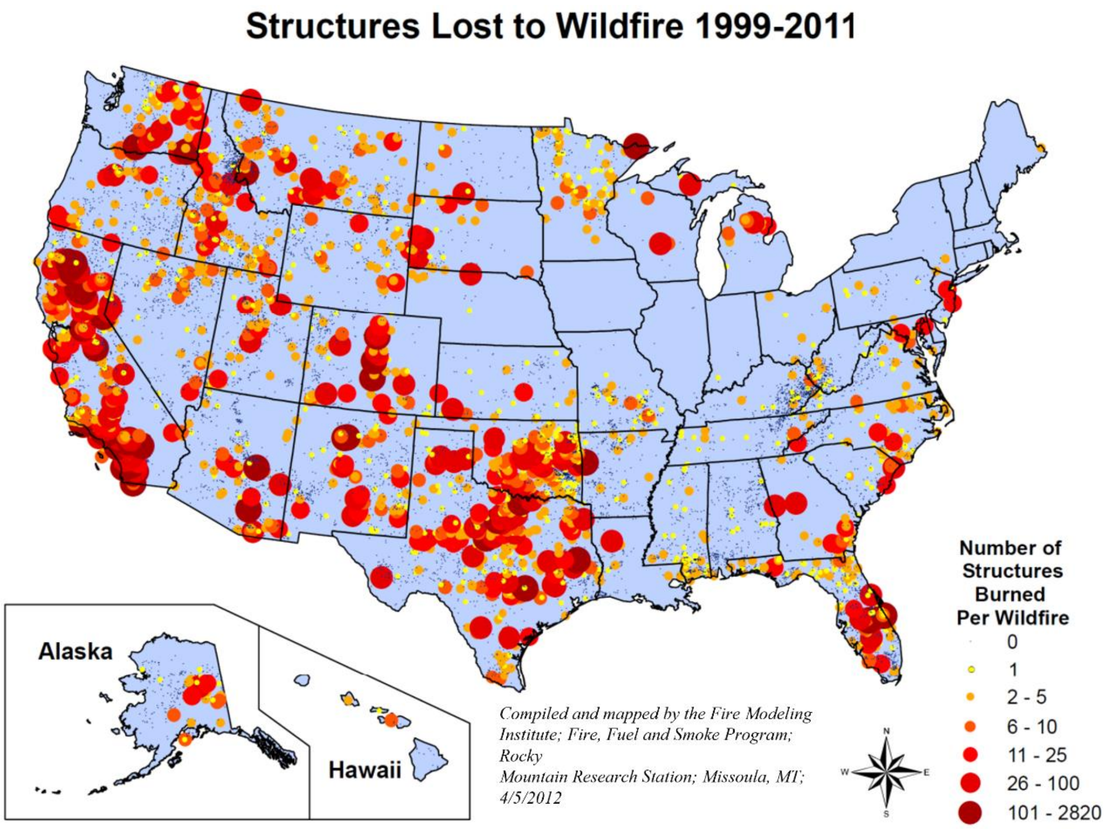

Figure 3: Map of structures lost to wildland fires in the United States, Alaska, and Hawaii from 1999 – 2011 reported in the ICS–209 database [9].

The 2007 Grass Valley fire in the San Bernardino Mountains destroyed 199 homes because of firebrand showers caused by intense 18 mph (8.05 m s^{-1}) winds that gusted to over 27 mph (12.07 m s^{-1}) [14]. Also in 2007, the California Firestorm, which was mostly dominated by the Witch Creek fire, burned a total of 197,990 acres while destroying 1,125 residential structures, 509 outbuildings, 239 vehicles, and damaging 102 other structures [15]. The estimated property damage of the California Firestorm was 1.8 billon U.S. dollars [16].

Although wildland fires are a yearly occurrence in the United States, cities such as Tokyo, Madrid, London, and Istanbul have experienced many major WUI fires in the past [17]. Specifically, places like South Korea, South Africa, and Portugal also experience these fires. Recently in April 2019, South Korea experienced, what government officials noted as the worst fire the country had seen, with a loss of 235 structures, 1,297 acres burned, and two deaths in the Goseong region where the 2018 Winter Olympics were held [18].

South Africa and other developing countries experience fires in what are known as informal settlements which generally consist of shacks on land that had not been surveyed or proclaimed as residential [19]. These fires still present a similar danger to humans and property, as well as spread similarly to those in a WUI setting. The city of Cape Town experiences about 500 deaths and 15,000 hospital admissions due to fires within the city [20]. In June 2017, the Western Cape town of Knysna suffered from multiple wildfires that burned about 37,000 acres near the area. This resulted in the death of seven people, and the destruction of 800 buildings and over 12,000 acres of forest plantations [8].

Recently in April 2021, flames swept across Cape Town's famed Table Mountain and damaged four buildings at the University of Cape Town [21]. One of these buildings was the historic Jagger library which held unique African books and manuscripts. Although some of these irreplaceable works were saved by fire–proof doors, many were lost from the event [21 – 23]. The temperature on this day peaked at 35 °C, and strong costal winds swept across the city overnight and into the day of the fire [21].

The Central Region of Portugal, between July 28th and August 19th of 2003, experienced six wildland fires that burned over 306,000 acres [24]. This 2003 wildfire season was identified as the worst season recorded for the area with a total burned area over 1.05 million acres, a 401% increase from the previous annual averages [24]. On June 17th, 2017, Portugal was suffering from a severe drought when two major fire events occurred that collectively destroyed over 116,140 acres of land, more than 250 houses, and resulted in 66 deaths. It was noted that during this event, most of these houses were ignited by glowing embers [25], also known as firebrands. As of August 10th, 2021, Greece, among other places in Europe and North Africa, has 586 WUI fires burning all over the country, forcing 63 organized evacuations of the local civilians [26]. The number of lost structures and burned area from each one of these fires can not only be attributed to the increase in WUI areas, but also to the many ignition pathways present during such large–scale events.

1.1.2 Role of Firebrands in Wildland Fires

Fire spread within WUI communities has been identified to occur via three main pathways [4, 27, 28]. First, radiant exposure from flames near structural elements. This can be caused by the radiant portion of the flames heating WUI structures resulting in the ignition of the combustible structural materials used [27]. Second, direct flame impingement from ignited nearby fuels. This occurs when flames in close proximity to the WUI structures exchange heat with flammable structural materials, possibly resulting in the ignition and flame spread across the virgin material [4, 29]. Third, transport and subsequent deposition of firebrands, which are generated and lofted ahead of the main fire front, onto combustible structural materials or wildland vegetation [28]. Firebrands are small pieces of smoldering or flaming material like wood or coal generated from the burning of vegetative fuels or structures during fires.

The deposition of firebrands onto combustible materials ahead of the fire front has been identified as being the prime means of fire spread during a wildland fire event [13 – 15, 25, 30 – 33], attributing to at least 50% of ignitions [34]. These glowing brands were found to be responsible for a majority of property loss during the Waldo Canyon fire, Grass Valley fire, California Firestorm, and the June 2017 Portugal fire mentioned in Section 1.1.1 [14, 25, 34]. The accumulation of firebrands was the cause of 2 out of 3 houses being destroyed in the 2007 Witch Creek fire [13, 15]. Also, Mark Potter states that close to 90% of the structures destroyed in Australian bush fires are a result of firebrand exposure [32].

Fire spread by firebrands comprises three main mechanisms [35], which can be seen illustrated in Figure 4:

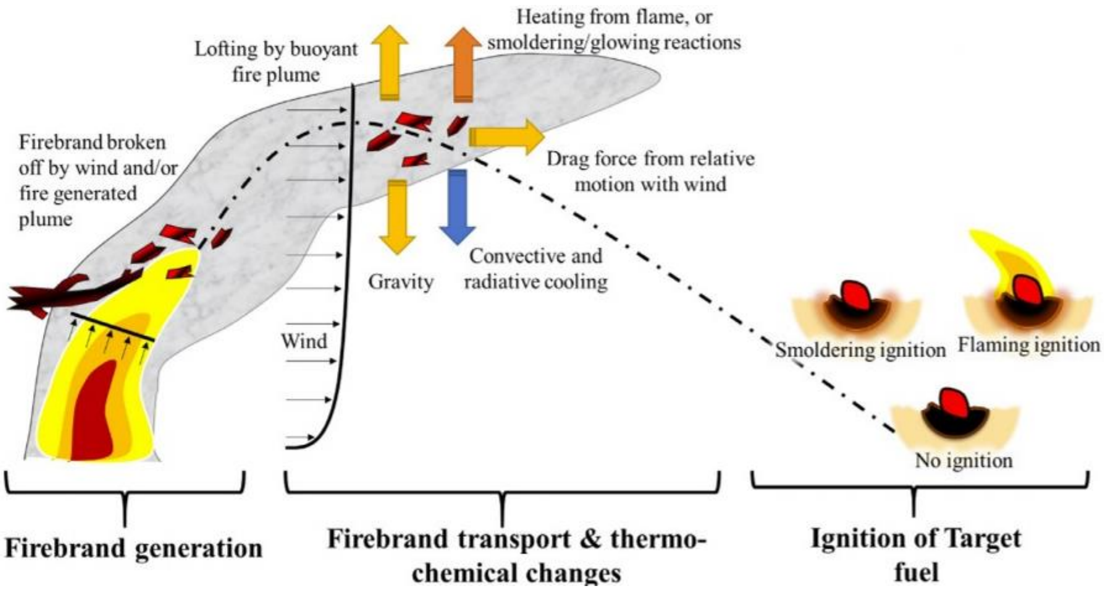

Figure 4: Firebrand sub–processes: (1) the generation of the firebrand(s), (2) coupled transport and thermo–chemical change, and (3) the potential target fuel ignition [35].

I. <u>Firebrand generation</u> from the burning of grasses, shrubs, and trees, as well as any wooden structures. These brands are made as the burning fuels break into smaller chunks due to structural changes from thermal decomposition processes. Firebrands can be either flaming or glowing and characteristics are dependent of fuel type, morphology of the fuel, and the intensity of the original fire [35].

II. <u>Firebrand transport</u> by ambient wind or the fire plume. This is caused by the strong buoyancy forces of the fire plume (vertical stack of smoke) lifting these light firebrands into the air and lofting them downwind of the fire front. These firebrands can be thrown as far as a mile (1.61 km) depending on fuel type and ambient windspeeds [36], causing what are known as spot fires. These spotting distances are short–distance (up to 500 – 750 m), medium–distance (1,000 –

5,000 m), and long–distance (over 5,000 m) [37]. These spot fires are a major mechanism for the spread of WUI fires, and under hot, dry, windy conditions can generate some of the most devastating fires [38].

III. Ignition of target fuel by firebrand deposition. When these firebrands land on virgin combustible substrates, they can be in a smoldering or flaming state. If the energy transferred from these brands to the target fuel is sufficient, the fuel may start to pyrolyze [35]. The entire heat transfer process of a firebrand on a virgin fuel is not fully understood, however is known that energy transfer happens by conduction and radiative heat transfer into the target fuel driven by the elevated temperatures of the firebrands [39]. If the brands can then continue to heat up the fuel, a transition of the fuel into a smoldering or even flaming combustion state may transpire. The likelihood of these transitions occurring are strongly dependent on target fuel characteristics like fuel type, density, temperature, and moisture content (MC), as well as environmental conditions like wind speed, ambient temperature, and relative humidity (RH) [35].

Although the firebrands can be generated and then transported large distances from the fire front, perhaps the most important mechanism is if the brands can ignite the new fuels. Warey investigated the influence of thermal contact between a glowing firebrand and a target fuel on the transient heat transfer into the fuel bed [40]. The study used a coupled zero– and two–dimensional explicit finite difference model for the firebrand and target fuel, respectively. A glowing disk–shaped firebrand and a glowing cylindrical shaped firebrand with poor contact on the fuel was modeled. Increased temperatures within the target fuel were observed when the relative contact pressure by the firebrand was increased in the disk–shape model under both the 0.5 m s^{-1} and 2.0 m s^{-1} wind speeds [40]. The cylindrical shaped firebrand with poor contact was modeled with a wind speed of 2.0 m s^{-1} and found to not pose any potential ignition sources. Warey notes that depending on the thermal state of the firebrand, the cylindrical dowel could provide a potential ignition source of the fuel bed [40]. Understanding how commonly used WUI building materials react to firebrand exposure can serve as a backbone for an approach to better improve the resilience of these vulnerable communities [41].

1.1.3 Ignition of Wooden Materials

A common target fuel in a WUI setting is an exterior–wooden deck [4, 40, 42, 43]. The organic composition of wood supports the different ways, described below, that a firebrand could interact when deposited on a vulnerable material. It was theorized that the ignition of these exterior decks was a major cause of property loss in the Waldo Canyon Fire [3, 13, 44]. If a deck was to ignite from the firebrand exposure, more of the deck can become involved and subsequently siding and soffit materials can ignite. Also, glass exposed to high amounts of heat can break and allow the fire to then spread into the structure [42].

The ignition process of wooden material contains many elementary chemical reactions involving both an oxidizer (oxygen (O_2) in the air) and a fuel (a wooden building material) [45]. Some wooden materials used in residential construction include, but are not limited to, Western Red Cedar (WRC), Japanese Cedar, Oriented

Strand Board (OSB), and Pressure–treated lumber. Chien *et al*. investigated the variations in the thermal decomposition kinetics of Japanese cedar [46] and provides an in–depth understanding of these processes, however, is beyond the scope of this study. Overall, the combustion reaction of a solid fuel, such as the wooden materials above, can be summarized by two chemical pathways [45, 47]:

I. <u>Pyrolysis:</u> The chemical decomposition of an organic–solid material by heating, in which a fuel–specific temperature is reached. This initiating a chain of endothermic reactions in which the long–hydrocarbon chemical constituents of wood break down into shorter chains [45]. Softwoods are generally 40 – 45% cellulose, 24 – 37% hemicellulose, and 25 – 30% lignin, while hardwoods contain 40 – 50% cellulose, 22 – 40% hemicellulose, and lignin as the remaining percentages [48]. Thermal decomposition occurs at temperature ranges of 230 – 330 °C for hemicellulose, 330 – 380 °C for cellulose, and 230 – 500 °C for lignin [49].

II. <u>Oxidation:</u> The exothermic oxidation reaction in which the carbon and hydrogen contained in the products of pyrolysis are stripped of electrons (oxidized) and ultimately form carbon monoxide (CO), carbon dioxide (CO_2) and water (H_2O) [50]. Oxidation at the surface of the fuel, known as smoldering, typically occurs at temperatures over 300 °C [47].

There are two types of combustion, flaming and smoldering. Smoldering is the slow, low–temperature, and flameless combustion by which oxidation of the fuel occurs on the surface of the fuel in the solid state [51]. Flaming combustion is the oxidation of the fuel in the gas phase, typically adjacent to the fuel bed [50]. Although flaming combustion is what many first think of when considering ignition, smoldering combustion was found to initiate under an incident heat flux of 7 kW m^{-2} versus 30 kW m^{-2} for flaming on a polyurethane [52]. Note that the thermal properties of polyurethane are different than that of the wooden materials found in the WUI, however this comparison illustrates how much easier smoldering combustion can begin on materials when compared to flaming.

1.2 Previous Firebrand Studies

Firebrands have been a major focus of research into the WUI fire problem. Studies have investigated the generation of firebrands to characterize the common sizes found in actual WUI fires. The knowledge of these firebrand characteristics has then been used to generate brands in an experimental setting to investigate common accumulation zones, as well as ignition propensity of combustible WUI vegetation/materials when exposed to these smoldering or flaming embers.

1.2.1 Firebrand Characterization

Previous studies have characterized physical attributes of firebrands like shape, size, and mass in actual urban fires [53 – 57]. These studies have recognized that many firebrands are cylindrical in shape when generated from burning vegetation. The mass distribution of firebrands produced from the burning of 2.4 m and 5.2 m Douglas–Fir trees of similar moisture content were found to be similar, with firebrand masses of 0.1 g being observed 70 – 80% of the time [54]. A Manzello *et al.* [55] study examined size distributions of firebrands generated during the 2007 Angora fire in California and found that most of these brands were < 0.40 cm^2 in surface area, and the largest was 2.02 cm^2 having dimensions of 0.64 cm by 3.18 cm. Vodvarka also found that from igniting five [56] and eight [57] full–scale residential houses, smaller brands, < 0.23 cm^2, were more commonly generated. Work was done by Suzuki and Manzello [53] to consolidate the brand characterization data from the above studies and numerous more. This study found that many firebrands from actual wildland fires are < 1 g, < 10 cm^2, and 1 – 3 cm in length. This knowledge has thus been used to create firebrands in a laboratory setting for small–scale studies on the thermal characterization of firebrands [43, 58 – 61].

The thermal characterization of these firebrand piles has been explored in past studies, however many used intrusive methods to measure heat flux and temperature of the brands. These methods include water–cooled heat flux gauges (WC–HFG), thin–skin calorimeters (TSC), and thermocouples (TC). For small or single firebrand piles, the diameter of the firebrand was found to have a significant effect on heat flux from the brand(s) [58]. Hakes *et al.* [58] used two set ups, one that utilized a WC–HFG imbedded in an inert substrate, and another that used sixteen TSCs in 4 x 4 array with a TC in the middle. For both set ups, 25.4–mm length cylindrical birch–wood dowels with 6.35–mm, 9.52–mm, and 12.7–mm diameters were dried in an oven at 103 °C for 24 hours, placed on an ignited propane burner to create the firebrands and then the non–flaming brands were deposited onto the flat measurement set up. These experiments found that the 6.35–mm diameter dowels yielded the largest peak heat fluxes from the deposited firebrand piles, when compared to the same pile mass created by the 9.52–mm, and 12.7–mm diameter dowels [58].

Another study by Salehizadeh *et al*. [59] used 12.7–mm birch–wood dowels to create firebrand pile masses of 4, 8, and 16 g and exposed these piles to wind speeds of 0 – 2.0 m s^{-1} inside of a contraction cone wind tunnel. From these three pile sizes, an 8 g pile yielded the largest peak heat flux over most wind speeds investigated. These heat flux measurements were made also with sixteen TSCs in 4 x 4 array like that in Hakes *et al*., however replaced the center TC with a WC–HFG all of which were imbedded in the same inert substrate. The study found that wind speed had a considerable effect on the duration of heating and the peak heat flux for a single firebrand size. The higher wind speeds yielded higher peak heat fluxes, but shorter heating durations [59].

More recently, Tao *et al*. [60] investigated the effects of firebrand size and geometry on heating from 4 g firebrand piles using a similar TSC and WC–HFG set up as the Salehizadeh *et al*. study. The different piles were created using small or large fluted cylindrical birch–wood dowels, thin or thick wooden disks, as well as more realistic fuels like pine bark flakes and eucalyptus stick of varying lengths. The study found that the geometry of individual firebrands, like cylindrical compared to wafer shapes, played a minimal role in heat fluxes and ignition probability. The bulk density, defined as the mass of the brands over the volume occupied by the brands, was found to play an important role in heat transfer from the pile. Tao states that this suggests the way a pile lands on a substrate would be important in the determination of ignition risk [60].

Bearinger *et al*. [62] used a non–intrusive technique of IR imaging to measure temperatures and subsequently heat fluxes from single firebrands. The study investigated surface heat fluxes from single–cuboid (6.35 mm by 6.35 mm by 38.1 mm) and cylindrical (6.35–mm diameter by 38.1–mm length) firebrands. Most of the tests were conducted with a wind speed of 1 m s^{-1}, however high localized heat fluxes of 80 – 105 kW m^{-2} for 1.0 – 2.1 m s^{-1} wind speeds were found from the single brands. These heat fluxes, when averaged over the size of the 12.5–mm HFG used in Hakes *et al*. [58] were about 7 – 25 kW m^{-2} [62]. These lower heat flux values agreed with those found in Hakes' study. The increase in wind speed was found to increase the heat flux levels, which was expected by the author given similar studies.

1.2.2 Firebrand Accumulation

When firebrands land on exterior decks, they can accumulate on top of the decking board surface, in–between the crevices of each board, within the gaps between a board and an exterior wall and within a reentrant corner [43, 63, 64]. Experiments using the NIST continuous–feed firebrand generator (NIST Dragon) have been conducted to identify the vulnerability of these common accumulation zones to firebrand showers [63, 65, 66]. Quarles *et al.* [40] ignited wooden cribs to test ignition potential of decks when exposed to firebrand showers in 4.5 m s^{-1} and 5.4 m s^{-1} wind speeds. The thicknesses of decking products ranged from ¾–inch (1.905 cm) to 1 ½–inch (3.81 cm) with ⅛–inch (0.3175 cm) gaps between each board. This study found that a common area for ignition from ember accumulation is within the gaps between decking boards above decking joists, which also agreed with the findings from a study by Dowling [67].

Manzello *et al*. [66] found that most of the firebrands generated and blown at a small decking assembly, collected within crevices and the small gaps between each decking board. Although firebrands more commonly accumulate inside of crevices configurations, proper understanding of the simple–flat accumulation zone is paramount to understanding the complex processes present during the ignition of these WUI materials when exposed to firebrand showers. This flat configuration would allow for identification of the primary driving forces for ignition of these common WUI materials when exposed to firebrands, without the complex effects of re–radiation that are present in the crevice configurations.

1.2.3 Ignition Studies

Hadden *et al*. [38] used hot spherical steel particles of varying diameters and initial temperatures to ignite cellulose fuel beds. This study integrated a hot–spot ignition theory to qualitatively describe a hyperbolic relationship of particle diameter with initial particle temperature on ignition propensity. This relationship can be seen in Figure 5. Note this study did not expose the hot inert particles to wind but was later replicated in studies which exposed these hot particles to wind speeds of 0.5 m s^{-1} [68 – 71]. Despite the qualitative validation, the hot spot theory used does not incorporate the chemical reactions of the hot particles that are present when considering glowing/flaming firebrand deposition. This ignition process of WUI target fuels by contributing firebrands has been explored in previous studies, however early investigation only focused on qualitatively characterizing the ignition of combustible substrates [72, 73].

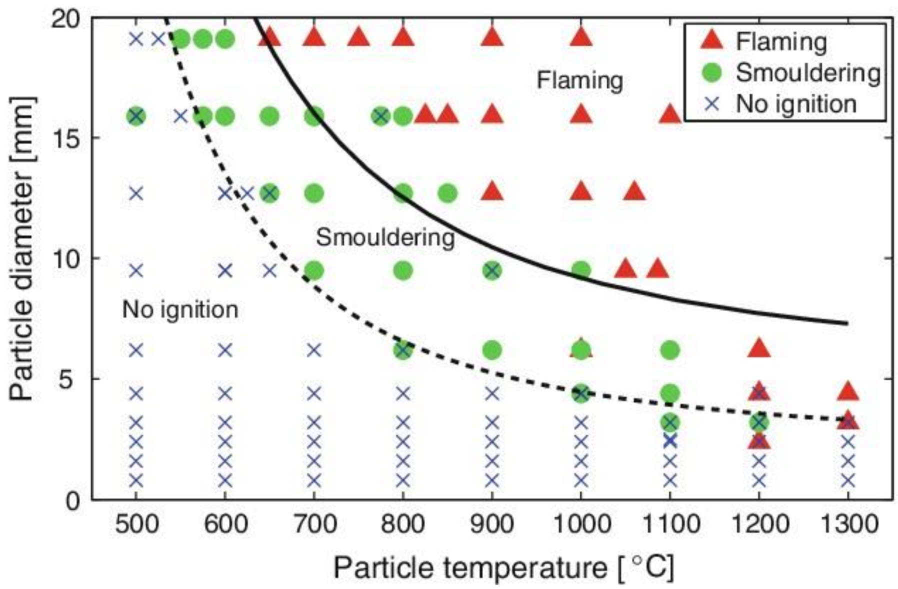

Figure 5: Ignition propensity of dry cellulose using heated steel spheres. The figure illustrates the hyperbolic relationship between particle diameter and initial particle temperature on the tendency for ignition [38].

Manzello *et al*. [72] examined the deposition of one or four, glowing or flaming firebrands in ignition propensity tests of pine needles, shredded paper, and crevices comprised of cedar shingles installed in a V–shaded duct. The study exposed the fuel beds to the selected number of firebrands made of ponderosa pine. The study found that a single glowing firebrand was not able to ignite any of the fuel beds considered. A single flaming brand, however, was able to ignite all the fuel beds except the hardwood at a MC of 11%. Four, 50–mm diameter 6–mm thickness disk, glowing firebrands ignited the pine needles into a flaming state under a 1.0 m s^{-1} environment. An interesting finding from this study is that the cedar–crevice configuration never ignited when exposed to multiple smoldering or flaming firebrands under both the 0.5 m s^{-1} and 1.0 m s^{-1} wind speeds [72].

Another set of similar ignition tests by Manzello *et al*. [73] on shredded hardwood mulch, pine straw mulch, and cut grass found that a single brand was not able to ignite these fuel beds. Three flaming brands, created from 25–mm and 50–mm diameter disks, were able to ignite the cedar crevice configuration under 0.5 m s^{-1} and 1.0 m s^{-1} wind speeds.

Manzello *et al*. [74] deposited two, three, or four glowing firebrands into crevices of 60°, 90°, and 135° angles made of either plywood or OSB. After the deposition, the brands were exposed to a wind speed of 2.4 m s^{-1}, note one test was conducted at 1.3 m s^{-1}. The study only observed flaming ignition in the four firebrands, 2.4 m s^{-1}, 60° tests of both materials. This 60° angle was tightest (i.e., the two boards were closest to facing each other) of the three, illustrating possible re–radiation effects of the two board faces with each other.

Manzello *et al*. [66] investigated the vulnerability of decking assemblies made of WRC, Douglas–Fir, and Redwood to continuous wind–driven firebrand showers. A wind speed of 6 m s^{-1} was used and each one of the decking materials were observed to have flaming ignition by the firebrands that accumulated on the deck's surface when exposed to a firebrand mass flux of 17.1 ± 1.7 g m^{-2} s^{-1} every 15 seconds. The average time to flaming ignition for the WRC deck was the quickest at 437 s as opposed to the 934 s and 756 s for Douglas–Fir and Redwood, respectively [66].The study also found that the mass required to reach flaming ignition of the decking materials varied from about 6 ± 2 g to 10 ± 3 g. Dowling [67] observed that 7 g of firebrands were able to initiate smoldering ignition of the wood members, however it was not stated if the brands were in a glowing or flaming state.

Hakes *et al*. [58] also conducted an ignition study on OSB and an inert substrate. The ignition tests used 12.7–mm firebrands to create 5 g and 10 g pile masses and exposed these brands to a wind speed of 1.84 m s^{-1}. This study did find that when the firebrand piles were first deposited onto the recipient fuel, flaming of the firebrands occurred very briefly due to the abrupt exposure to the external air flow. It was noted that this flaming was observed on both the inert and OSB substrates, however, was not sustained. Salehizadeh *et al*. [59] used marine–grade plywood and cedar shingles, as well as OSB. These ignition experiments found that for about 50% of the tests, the transition from smoldering to flaming occurred around 1.2 m s^{-1} for the 16 g and 1.4 m s^{-1} for the 8 g deposited pile masses [59]. Smoldering ignition was assumed to be present when any of the TCs pinned 0.5–mm below the top surface of the sample reached 200 °C. While flaming ignition was defined as any flames being present on top of the fuel bed, found by observing video recordings of the tests [59].

1.3 Motivation

Previous studies have investigated the vulnerability of decking materials when exposed to a single, or an accumulated pile of firebrands. Despite the thermal characterization of different firebrand sizes, shapes and pile masses, few studies focused on quantifying ignition criteria or the thermal response profiles for decking materials when exposed to different air flow velocities. Ignition studies of decking materials exposed to firebrand piles have been conducted separately from thermal characterization studies. These studies that have attempted to thermally characterize firebrand piles and solid wooden material surrogates exposed to these firebrand piles have made use of intrusive measurement methods such as thermocouples (TC), water–cooled heat flux gauges (WC–HFG), or thin–skin calorimeters (TSC). These methods can interfere or disrupt the heat transfer mechanisms present during the firebrand exposure and subsequent decomposition of these decking materials. Also, these techniques provide local–spot measurements, and do not allow for an accurate spatial quantification of temperature or heat flux. Thus, a more accurate and less intrusive quantification of the thermal characteristics of firebrand pile masses and decking materials exposed to these firebrands under different wind environments is required to ensure accurate modeling and prediction of flame spread across the material. IR thermal imaging has been used as a non–intrusive method for thermal characterization of a single firebrand when exposed to air flow velocities, however accumulated firebrand piles have been attributed to the increased propensity of flaming ignition of decking materials.

Western red cedar, a low–density commercial wood, has been investigated as a WUI material in previous large–scale firebrand ignition studies, however, has not been studied in smaller scale experiments. Properly understanding the complex processes present during the ignition of this WUI material when exposed to firebrand showers in the simple–flat decking accumulation zone will allow for more precise investigations into the more common yet multifaceted crevice and corner accumulation zones. This flat configuration would also allow for identification of the primary driving forces for ignition of these common WUI materials when exposed to firebrands, without the complex effects of re–radiation that are present in the other configurations.

1.4 Objective

The ignition probability of a common WUI decking material, WRC, in a simple–flat decking accumulation zone, aims to be quantified under two different glowing firebrand pile masses and different air flow velocities within the same bench–scale wind tunnel used in the Salehizadeh *et al*. [59], Tao *et al*. [60], and Duarte *et al*. [61] studies. The conditions leading to the smoldering and flaming ignition of this wooden decking material when exposed to the glowing firebrands in the flat accumulation zone will be studied with the goal of accurately quantifying the thermal response of the material.

This study seeks to quantify the spatial and temporal temperature profiles of the two firebrand pile masses more accurately under different wind speeds, as well as the thermal insult of a representative WUI decking material when exposed to the same firebrand pile masses and wind speeds. The study aims to quantify the temperature profiles using non–intrusive measurement methods as opposed to the TC methods used in previous studies [58 – 61]. These temperature profiles could then be used in an inverse heat transfer analysis to quantify incident–heat flux profiles, also generally found using intrusive methods like WC–HFGs or TSCs, from the brands to the deposited surface.

Gas analysis of the exhaust flow inside of the wind tunnel will be used to quantify the combustion mode (i.e., smoldering or flaming) present and heat release rate (HRR) profiles of the decking material when exposed to the firebrand pile masses and air flow velocities. Quantities indicative of smoldering, such as the Modified Combustion Efficiency (MCE) are fuel dependent; therefore, the study will couple the gas analysis measurements with visual confirmation of smoldering or flaming conditions for the proceeding experiments with standard video recordings. All measurements in this study will be made simultaneously, to allow for a more comprehensive comparison of the quantifications being made and to investigate possible influence one may have on another.

Chapter 2: Experimental Methodology

2.1 Experimental Setup

2.1.1 Wind Tunnel Setup

The wind tunnel apparatus used in this study was similar to that used in the Salehizadeh *et al.*, Tao *et al.*, and Duarte *et al.* studies [59 – 61], however small modifications were made to accommodate apparatuses used for this study. A three–dimensional drawing of the entire wind tunnel setup can be seen in Figure 6.

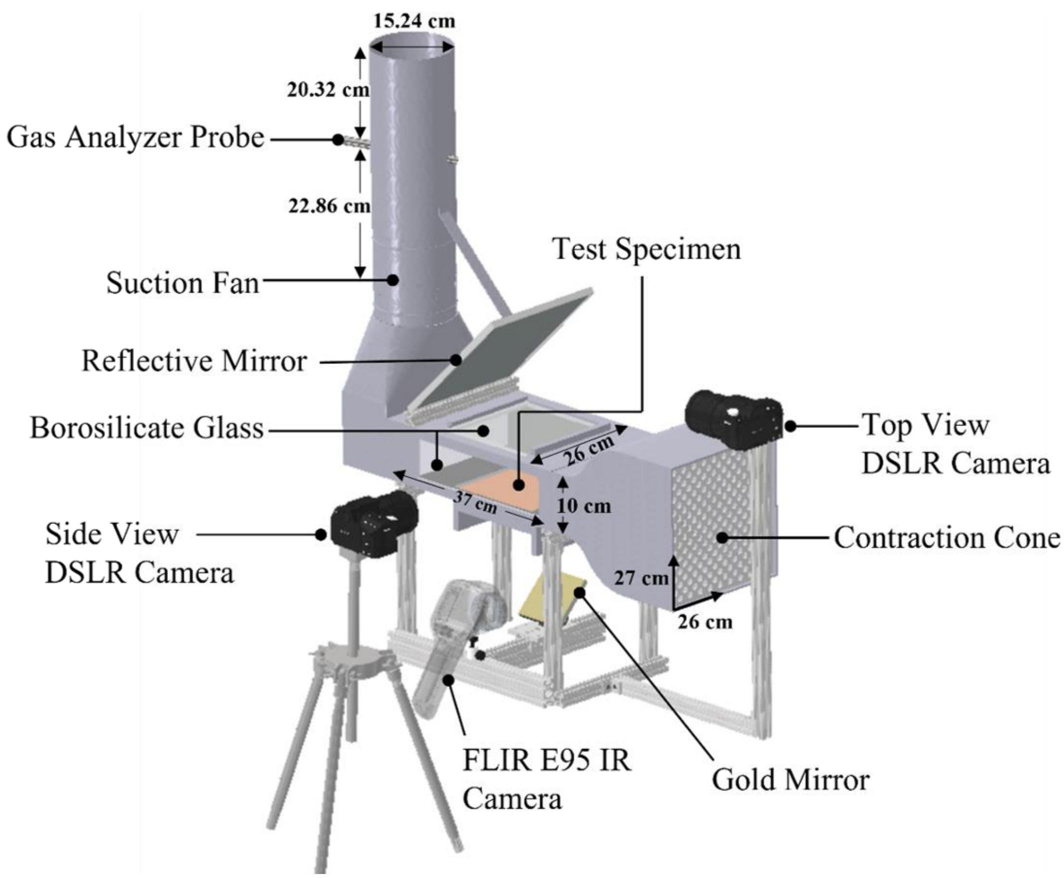

Figure 6: Three–dimensional drawing of entire wind tunnel setup used for all tests.

The tunnel consisted of a 27–cm high by 26–cm wide contraction cone with a multi–layer honeycomb mesh which reduced to a stainless–steel 37 cm by 26 cm by 10 cm test section. The internal surfaces of the test section were coated with Tempil Pyromark 2500 Flat Black high temperature paint to reduce the amount of reflection from the stainless–steel metal. The contraction cone and honeycomb design created a uniform–straightened developing flow across the test section. This flow profile downstream of the contraction cone is characterized in Section 2.3.1.

A 90° vertical bend was placed downstream of the test section and was connected to a 6–inch (15.24 cm) diameter exhaust duct where a TerraBloom DBF6 high–temperature suction fan was located. A Hydrofarm Active Air Fan Speed Adjuster was connected to allow for control of the air speed within the tunnel. The fan was able to generate wind conditions in a range of 0.5 – 3.5 m s^{-1}. Three air flow velocities were selected for this study, 0.9, 1.4, and 2.4 m s^{-1}. Previous studies have noted that these velocities are representative of wind speeds during real WUI fire events [55, 74 – 78]. The 1.4 m s^{-1} air flow velocity has been used in previous studies in the same wind tunnel [59 – 61].

A sample holder was located at the underside, 18.5–cm length by 18.5–cm width, opening of the test section with the capability of being removed. This allowed for the height to be adjusted so that the top surface of test specimens would be kept flush with the bottom of the tunnel, despite varying thicknesses. The sample holder had an open back such that mounting the specimen did not interfere with the IR measurement system, described in Section 2.1.3. The roof of the test section contained a 20 cm by 19 cm opening which allowed for a metal 10 cm by 5 cm firebrand deposition funnel to be placed onto the surface of the test specimen. This 50 cm^2 deposition area was selected considering the square 7 cm by 7 cm (49 cm^2) deposition area used in a previous firebrand characterization and ignition study using the same wind tunnel [60].

The test section contained a 20 cm by 6 cm borosilicate glass side window to allow for a side–profile video recording of the test specimen with a tripod mounted Nikon D7100 DSLR camera. A second–removeable 20.5 cm by 20.5 cm piece of borosilicate glass covered the top opening of the wind tunnel and a standard 29 cm by 24 cm mirror was lowered to a 45° angle to reflect a top view of the mounted test specimen. This top–profile was recorded using a Sony Alpha SLT–A55V DSLR camera. Both of these video recordings were used to visually identify flaming ignition of the firebrands or representative WUI decking material.

2.1.2 Gas Analysis System

The gas analysis system was implemented to measure the percentages of CO and CO_2 within exhaust flow of the wind tunnel. The system comprised a 9–inch (22.86 cm) long, ⅝–inch (1.6 cm) O.D., 0.065–inch. (0.165 cm) wall thickness 304 stainless steel smooth–bore seamless tube inserted 1.5 diameters, 9 inches (22.86 cm), above the variable fan. This gas analyzer probe height was also 8 inches (20.32 cm) below the top of the exhaust duct. This sampling probe contained two rows of 36 (72 in total), 1–mm holes spaced 2 mm on–center both vertically and horizontally from each other. The probe was designed considering a previous study where a similar gas probe was designed to sample an exhaust flow [79]. Two holes were drilled straight through the 6–inch (15.24 cm) diameter wind tunnel exhaust duct and the probe was inserted such that 1 cm was protruding from the outer face of the duct on the opposite side from which the probe was inserted. The 72 probe holes were now centered with the exhaust duct and faced downwards, opposite the exhaust flow. The protruding end of the probe and both insertion holes in the duct were sealed with a –65 °C to 343 °C rated RTV Silicone gasket maker.

The unsealed end of the probe was connected to 150–cm long ¼–inch (0.635 cm) O.D. Coilhose Pneumatics NC0435 red nylon tubing which carried the sampled flow to a 316 L stainless–steel Headline Filters Model 126 soot filter. After the soot filter, the sampled gas was pulled via an 8 LPM supply vacuum pump towards the gas analysis system. Once past the pump, Drierite was used to remove any moisture from the sampled gas before being fed into the CAI ZPA Non–Dispersive Infrared (NDIR) Gas Analyzer. This NDIR analyzer was used to measure the volumetric percentages of CO and CO_2. A majority of the flow was purged out of a needle valve so that only 1.5 LPM of the final gas sample was sent into the analyzer.

The NDIR analysis method is based on the infrared absorption characteristics of gasses. A single infrared beam of light is modulated by a chopper system and passed through a sample cell of known length containing the gas sample. The attenuated beam emerges from the cell and is then introduced to the front chamber of the two–chamber infrared microflow detector. The voltage output measurements from this analyzer for both the CO and CO_2 vol.% concentrations were obtained with a National Instruments

NI–9215 analog voltage output module (0 – 10 Volts) at a frequency of 10 Hz and processed via a LabVIEW script. The calibration of this gas analysis system can be found in Section 2.3.2.

2.1.3 IR Temperature Measurement System

Infrared (IR) radiation is the band in the electromagnetic radiation spectrum with wavelengths of 780 nm – 1 mm, which is slightly higher than that of red visible light [80]. IR sensors detect the frequency and intensity of the IR radiation and converts it into a temperature reading. Some IR thermal imaging cameras utilize a focal plane array sensor which creates a spatial temperature image. IR thermal imagery is commonly used in the Controlled Atmosphere Pyrolysis Apparatus II (CAPA II) to measure the back surface temperature of test specimens [81]. The back surface is coated uniformly with a high temperature paint of known emissivity (ϵ) to ensure the accuracy of the spatially resolved temperature measurements. The IR camera is typically pointed at a gold mirror to direct the view onto the bottom of the sample. Gold, with an average reflectance of 0.96, is specifically used as it keeps this high reflectance constant over 700 – 10,000 nm wavelengths, as opposed to its silver and enhance–aluminum mirror counter parts. Although the CAPA II test apparatus is a gasification instrument specific to material flammability studies, the techniques of using IR imaging was used by the Bearinger *et al.* [62] study mentioned in Section 1.2.1.

The IR temperature measurement system in this study was used to non–intrusively measure the back–surface temperatures of the wind tunnel mounted test specimen. The entire apparatus was constructed with 80/20 T–slot Aluminum brackets and can be seen in Figure 7.

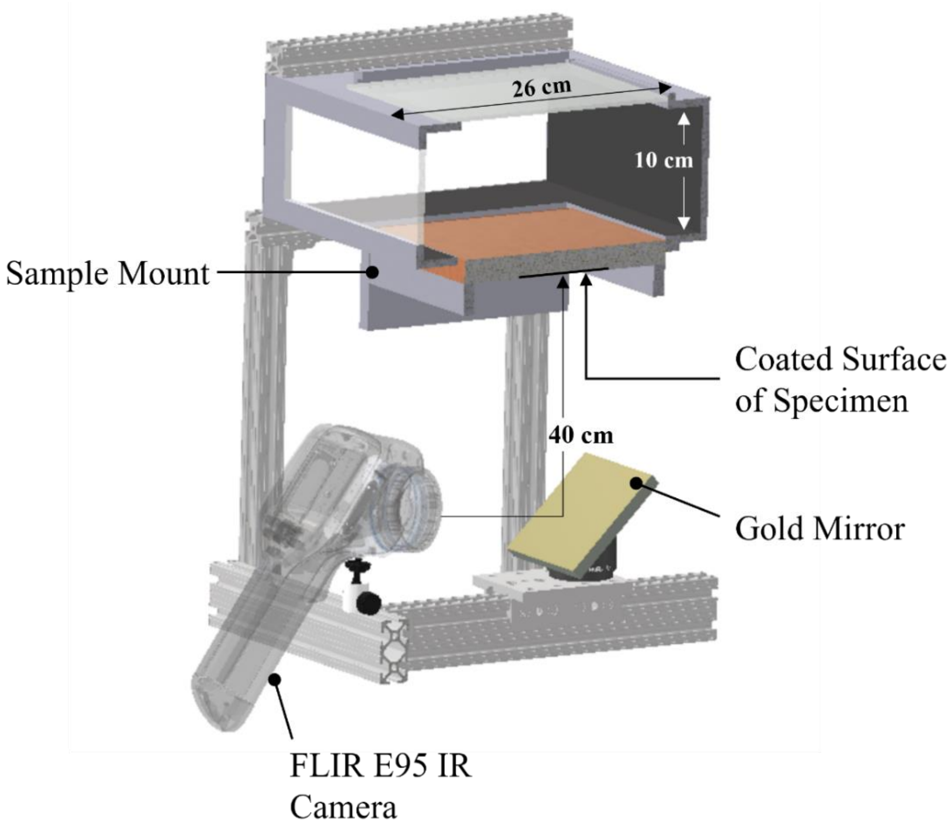

Figure 7: FLIR E95 IR camera and gold mirror apparatus used for back surface temperature measurements.

The system consisted of a FLIR E95 thermal imaging camera with an IR resolution of 464 by 348 pixels, image frequency of 30 Hz, and spectral range of 7.5 – 14.0 µm. This camera measured temperatures in the range of 0 – 650 °C and was mounted with a panoramic ball head camera mount, directly facing an Edmund Optics 100 mm square Protected Gold coated λ/10 mirror. The apparatus used the IR camera and gold mirror set up similar to that in the CAPA II set up [81]. The total distance, from the lens of the camera to the mirror then from the mirror to the back surface of the substrate, was 40 cm. The gold mirror was mounted in a Thorlabs 45° optical mount such that the mirror reflected the back surface of a wind tunnel mounted specimen into the view of the IR camera. This back surface was sprayed with a Medtherm Corporation optical black coating, described in Section 2.2.1. This optical coating is used because of its known and constant emissivity (ϵ) at elevated temperatures. The 45° mount was epoxy glued onto an 80/20 Aluminum T–slot track slider which allowed for the mirror to be slid underneath the sample mount, while keeping the 40 cm distance consistent for all tests. The use of 80/20 brackets also allowed for the entire setup to be detached from the wind tunnel for emissivity calibrations described in Section 2.3.3. The gold mirror was selected for its constant–high reflectance over the spectral range, mentioned above, of the IR camera. Also, gold is the material used in the CAPA II apparatus and has been shown to accurately reflect IR–thermal insult [81].

2.2 Material Selection

2.2.1 Substrate Selection and Preparation

The inert substrate selected for the thermal characterization of the firebrand piles in this study was ⅛–inch (0.3175 cm) thickness Kaowool PM ceramic fiber board fabricated by Morgan Advanced Materials. This insulation board is similar to the inert species used in the previous studies mentioned in Chapter 1 of this report [58, 59]. This thickness was chosen to justify the assumption of one–dimensional heat transfer through the insulation board (i.e., length and widthwise thermal diffusion was assumed negligible) [82]. Also, this thickness allowed for the assumption that the IR temperature measurements can be spatially resolved to an accuracy up to that of the thickness of the sample, ⅛–inch (0.3175 cm) [83]. Western red cedar (WRC) boards of ¾–inch (1.91 cm) thickness were selected as the representative WUI decking material. Thermophysical properties of both the Kaowool PM and WRC substrates can be found in Table 1.

Table 1: Thermophysical properties of Kaowool PM and WRC specimens. Note that heat capacity and thermal conductivity of WRC were taken at 25 °C and 15% MC.

Test Specimen	Density [kg m^{-3}]	Heat Capacity [J g^{-1} K^{-1}]	Thermal Conductivity [W m^{-1} K^{-1}]
Kaowool PM	256 [84]	1.07 [84]	$0.052 - 4 \times 10^{-5}$ T $+ 1 \times 10^{-7}$ T^2 [84]
WRC	368 [85]	1.7 [86]	0.11 [85]

WRC is one of the lightest commercial softwoods [85]. This low density is due to the high portion of cell cavities containing air. Due to air's high thermal insulation properties (i.e., a low thermal conductivity of 4.97×10^{-2} W m^{-1} K^{-1} at 375 °C [87]), WRC is one of the best wooden thermal insulators [85] and would not efficiently dissipate intense heat applied to it. This could cause a fast rise in surface temperature of the WRC, which may increase the chances of ignition. Note that WRC's thermal properties are relatively close to that of the Kaowool PM insulation board, confirming that WRC has strong insulation properties. Due to these properties, WRC is commonly investigated as a WUI material in large–scale tests [88 – 90] and was found to have an ignition temperature range of 350 – 450 °C [91] and 354 °C over an irradiance range of 15 – 45 kW m^{-2} [92]. It is important to note, that WRC has been investigated in large–scale experiments, however, has not been investigated in bench scale flammability studies. Pictures of fully prepared Kaowool PM and WRC specimens for wind tunnel tests can be seen in Figure 8.

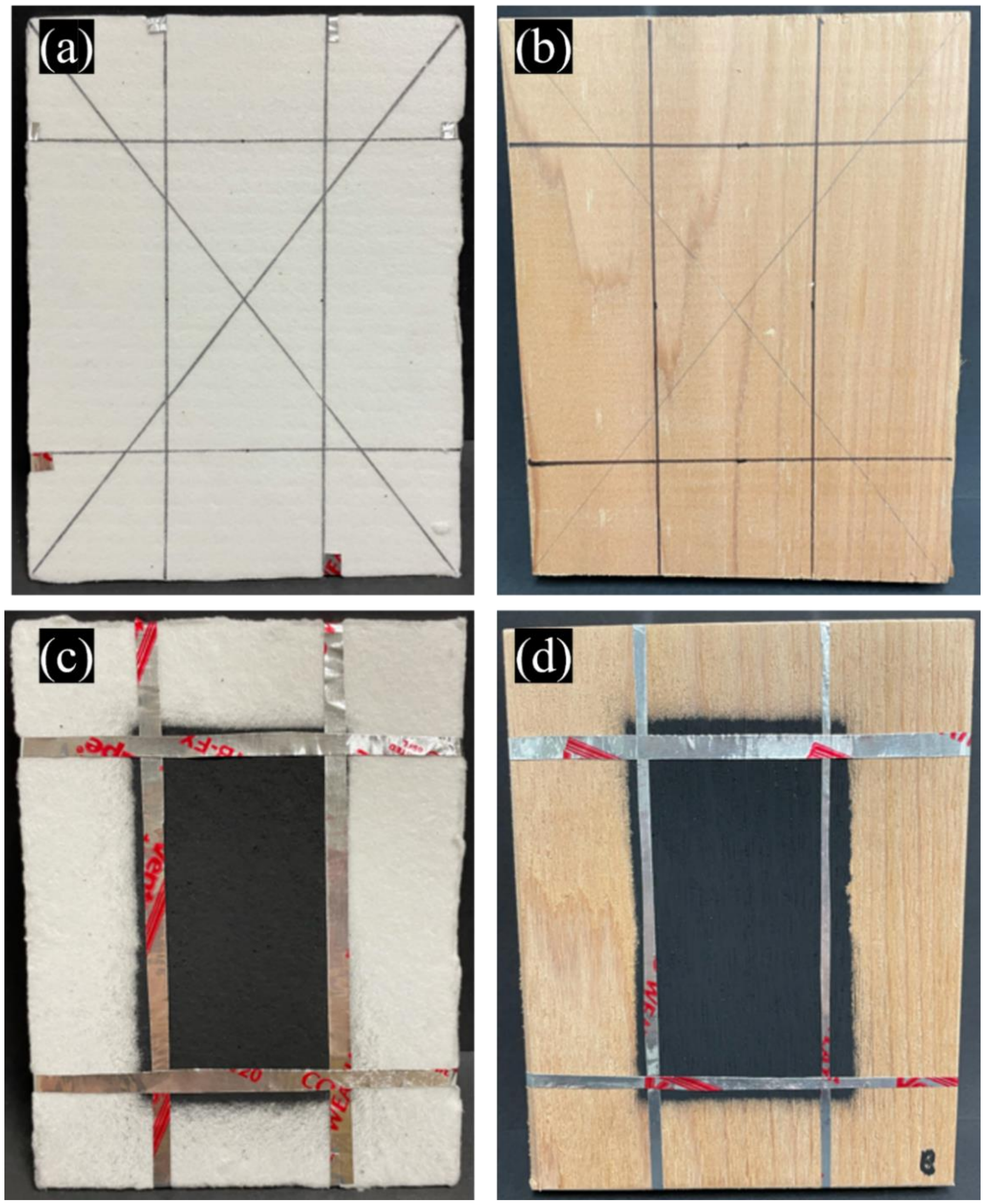

Figure 8: Fully prepared Kaowool and WRC test specimens; frontside (a) – (b) and backside (c) – (d). The aluminum foil tape outlined the 50 cm^2 deposition area onto the backside of the specimen for the IR camera to see.

Both substrates were machined into 18–cm length by 14–cm width rectangles as these dimensions allowed for the samples to be securely placed within the wind tunnel sample mount. Note that the WRC boards were cut such that the 18–cm length was with the grain of the wood. For both materials, there was a smooth–finished frontside and a rough–unfinished backside. The backside of the WRC specimens were lightly sanded with P80 grit sandpaper to remove large imperfections of the surface that could flake off after the surface had been coated with an optical black coating. Sanding the surface of the WRC sample also increased the roughness which allowed for better contact of the paint onto the WRC. The perimeter of the 10 cm by 5 cm deposition area was then centered and traced onto each substrate's frontside which allowed accurate deposition of the firebrand pile in the same area where the optical black coating was applied on the opposed face.

The substrates were then sprayed with an optical black coating, Medtherm Corporation with average absorptance of 0.95 from 0.3 – 15 µm, covering a 12 cm by 7 cm area centered on the backside. Section 2.3.3 describes the temperature range that this optical coating operated. The paint was applied using a template such that a thin–uniform layer covered the exposed area (12 cm by 7 cm). After the paint was applied, the substrates were left in a fume hood for 24 hours to allow for the paint to dry. Thinly cut, roughly 5 mm in width, strips of aluminum foil tape were then wrapped from the four lines on the frontside onto the painted backside. The tape now outlined the perimeter of the 10 cm by 5 cm deposition area onto the substrate's backside where the optical black coating was applied. Since the metal tape had a different reflectance than the substrates, the tape outlined the firebrand deposition area for the IR camera during tests. The WRC specimens were placed in a desiccator held at a humidity level of 22 ± 2 % with fresh Drierite, for 48 hours to lower the moisture content (MC) of the boards to 5.1 ± 0.2 % (dry basis), 4.9 ± 0.1 % (wet basis). Equation (1) and (2) give the expressions used to calculate these MCs.

$$MC_{dry} = \frac{m_{wet} - m_{dry}}{m_{dry}} \; x \; 100\% \tag{1}$$

$$MC_{wet} = \frac{m_{wet} - m_{dry}}{m_{wet}} \; x \; 100\% \tag{2}$$

Where m_{wet} is the mass of the board before being placed into the desiccator and m_{dry} is the mass after. Both masses were measured with an AWS PN–2100A precision balance (± 0.1 g). The variation for all quantities reported in this study was represented using Equation (3).

$$Variation = \pm \frac{2\sigma}{\sqrt{n}} \tag{3}$$

where σ is the standard deviation of the sample, and n being the number of individual values considered.

2.2.2 Firebrand Selection and Preparation

Previous studies have noted that size, shape, and initial mass of a single firebrand influences heating intensity and duration [39, 60], however, to minimize complexity of this study, only cylindrical dowels of a single diameter were used. Birch–wood cylindrical dowels, 6.35 mm in diameter and 25.4 mm in length, were used to prepare the glowing firebrands that are deposited on the substrate within the wind tunnel. Glowing firebrands were selected, as opposed to flaming, because firebrands tend to land on target fuels in a glowing state [35]. These cylindrical dowels have been found to produce piles with the largest peak heating rates and increased heating durations, compared to the same pile mass created by 9.52–mm, and 12.7–mm diameter dowels [58]. Also, these birch wood surrogates were selected as they could be easily supplied as the experiments needed and were used in previous bench–scale firebrand experiments [58, 60, 61]. It should be noted however, that the density of these undried dowels is slightly higher (580 ± 30 kg m^{-3}) than that of softwoods commonly found in the WUI that these firebrands are generated from (350 – 530 kg m^{-3}) [86].

The dowels were dried in a Quincy Lab, Inc. Mechanical Convention Oven at 103 ± 2 °C, per ASTM Standard D4442 [93], for 24 hours [39]. The initial MC of the dowels prior to being dried was 10 ± 0.1 %. After the 24 hours, the dowels were placed in one–gallon plastic bags with four silica gel desiccant packets. These bags remained closed until the dowels were needed for firebrand generation. The two firebrand pile masses used in this study were 3 g and 8 g. The 3 g pile was selected as this was found to be the minimum mass required to cover the selected deposition area with one layer of firebrands, approximately 1 cm in height. Tao *et al*. [60] noted an 8 g pile as being the upper critical firebrand pile mass in which any larger pile mass resulted in a decrease in the measured peak heat flux of the pile, therefore 8 g was selected as the second pile mass. This 8 g pile was approximately 2.5 cm in height. Figure 9 shows the heights of the two firebrand piles.

Figure 9: Heights of 3 g, 0.06 g cm^{-2} coverage density (a) and 8 g, 0.16 g cm^{-2} coverage density (b) firebrand piles placed in the 10 cm by 5 cm test deposition area. Note the ruler in the figure shows units of mm.

To generate the glowing firebrands, a wire mesh pan was placed onto an AWS PN–2100A precision balance (± 0.1 g). 108 g of the dried dowels for an 8 g (coverage density of 0.16 g cm^{-2}) test, or 48 g for a 3 g (0.06 g cm^{-2} coverage density) test was placed into the mesh pan such that it formed a mound pile as depicted in Figure 10(a) and (b). The coverage density is defined as the mass of firebrands over the area on which they were deposited (50 cm^2). A propane burner was ignited, and the flow rate of the fuel was adjusted so just the tips of the blue flames were past the burner's top surface, shown in Figure 10(c). This flame height correlated to a propane flow rate of 1.83 ± 0.06 SLPM. Keeping the dowels in a pile instead of covering the entire pan allowed for all dowels to be exposed to the burner flame at the same time, which more consistently yielded the excepted firebrand pile mass. The dowels were exposed to the flames for 40 seconds, and then allowed to burn until the flames extinguished, which was about an additional 141 ± 15 seconds and 221 ± 31 seconds for the 48 and 108 g piles, respectively. Once the dowels were no longer flaming, they were considered glowing firebrands, and were ready to be deposited onto the substrate mounted within the wind tunnel.

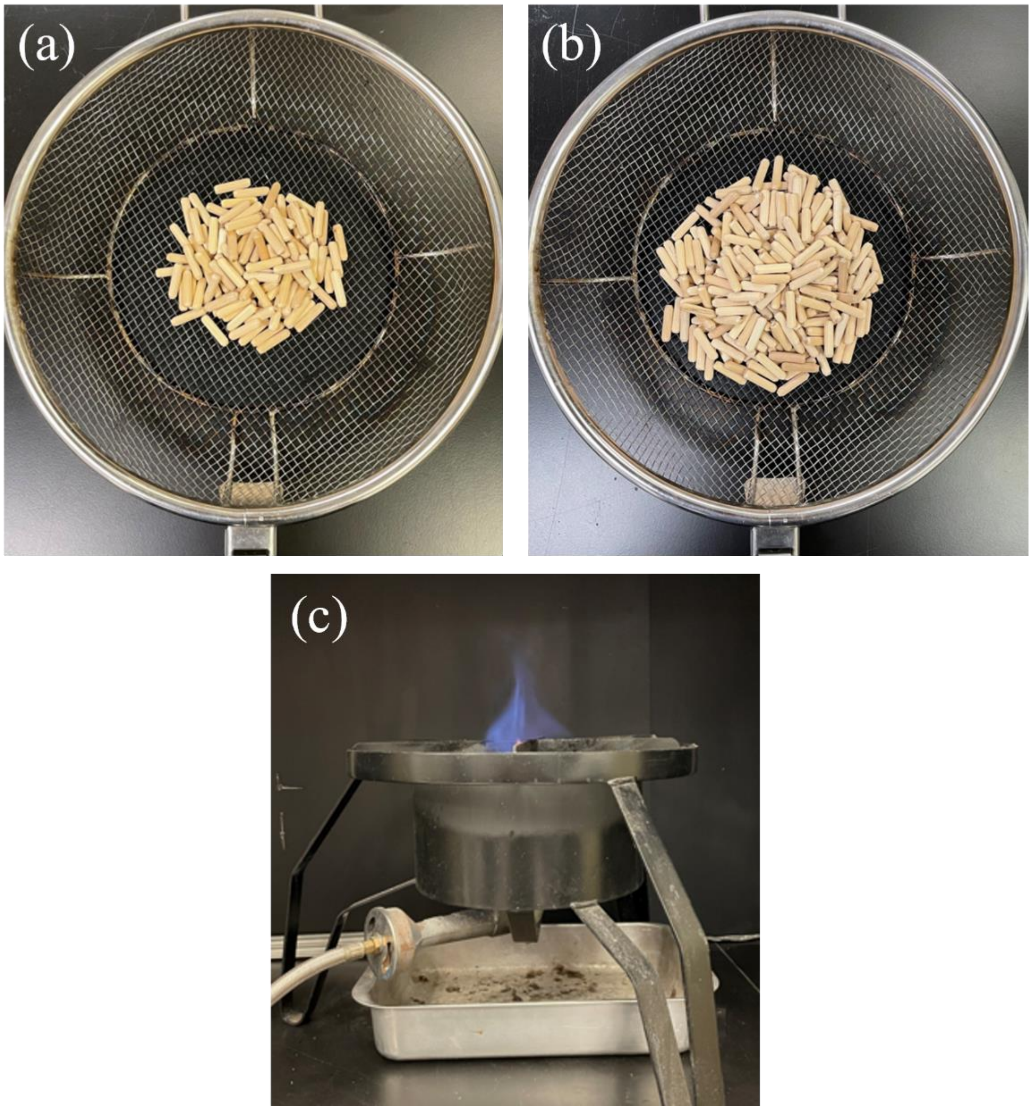

Figure 10: Dried birch–wood cylindrical dowel pile in wire mesh pan for firebrand preparation: 48 g (a) and 108 g (b). Flame height of propane burner for firebrand preparation (c). Note the flame tip was intermitted, however the wider region seen closer to the burner surface was constant at this height.

Two representative batches of both 3 g and 8 g piles can be seen in Figure 11. After these glowing brands were generated, smoldering was quenched with water and then dried in the conventional oven for 24 hours. Ten randomly selected brands from each batch were removed and their respective masses were measured with an A&D BM–22 Ion Micro Balance having a variability of ± 0.01 mg. The lengths and diameters of each brand were also recorded with precision calipers. The projected area of each brand was calculated as that of a rectangle. These masses and areas were found to be 41.3 ± 10.7 mg, 0.63 ± 0.10 cm^2 for the 3 g piles and 47.6 ± 11.5 mg, 0.62 ± 0.11 cm^2 for 8 g piles. Note that the variations were represented using Equation (3).

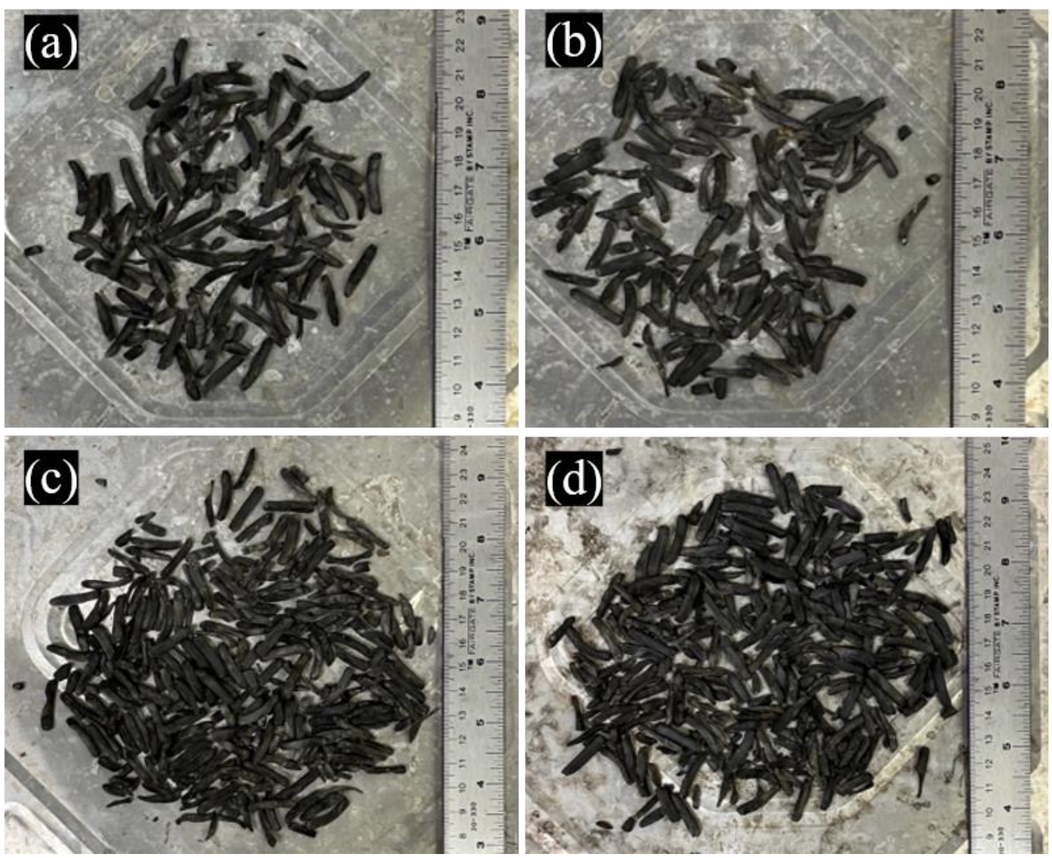

Figure 11: Representative batches of glowing firebrands for 3 g (a) – (b) (0.06 g cm^{-2}) and 8 g (c) – (d) (0.16 g cm^{-2}) tests.

These masses and projected areas aligned with the range of firebrand data consolidated from numerous studies and investigations [35]. Figure 12 shows the mass and projected area of firebrands collected from the Beppu–city and Itoigawa–city WUI fires. The glowing firebrands generated in this study are representative of observations during real WUI fire events [53, 55] and it has been noted that most glowing brands in real fire events were found to have areas smaller than 10 cm^2 [35, 53]. Manzello *et al.* [55] noted that 80% of firebrands found in the 2007 Angora Fire had projected areas less than 0.5 cm^2. Also, Manzello *et al.* [35] consolidated firebrand mass data from the burning of 4.0 m Korean Pine, 2.6 m Douglas–fir, and 5.2 m Douglas–fir trees; This study found that about 85% of firebrands collected had a mass less than 0.1 g.

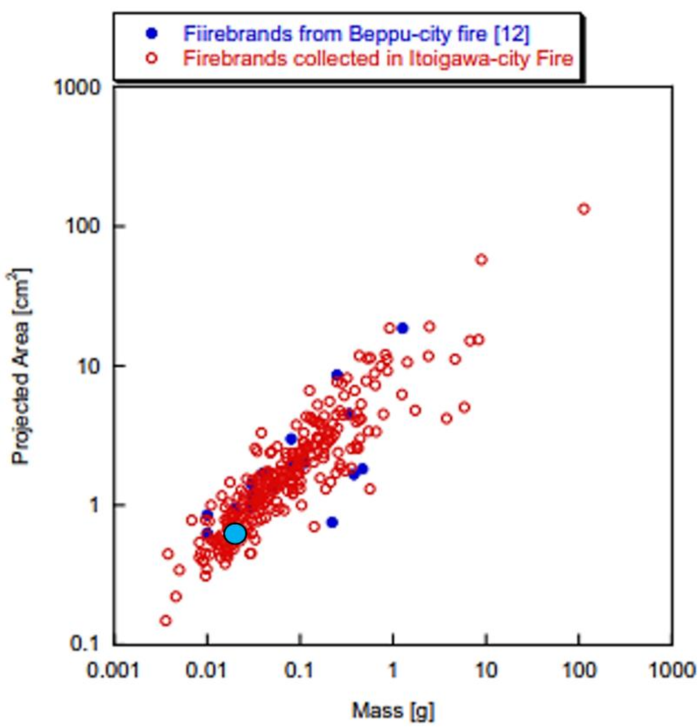

Figure 12: Mass and projected area of firebrands collected from the Beppu–city and Itoigawa–city WUI fires [53]. The light blue dot on the graph represents the range of glowing firebrands generated in this study.

2.3 Setup Characterization and Calibration

2.3.1 Wind Tunnel Flow Characterization

The wind tunnel flow profile was characterized by measuring the wind speed with a calibrated Omega HHF–SD1 Hot Wire Anemometer (0.2 – 20 m s^{-1}). Figure 13 shows a 5 by 5 array used to insert the anemometer resting on top of the wind tunnel.

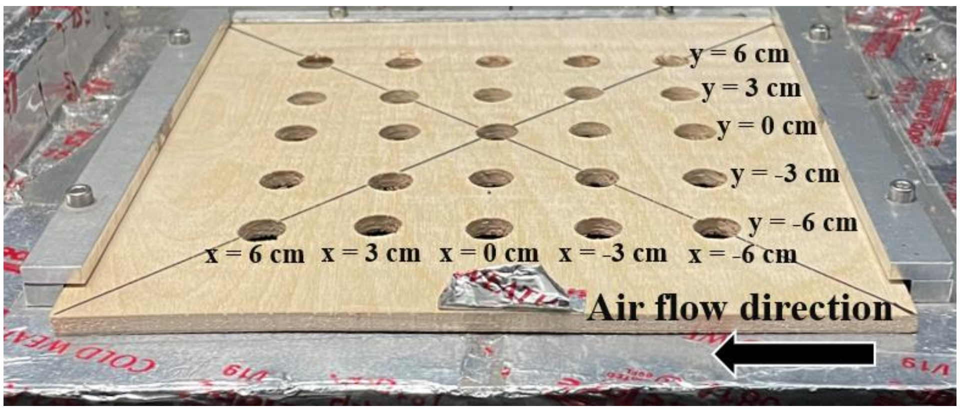

Figure 13: 5 by 5 array (25 locations) used to insert an anemometer through the top opening of the wind tunnel test section for flow characterization.

Measurements were taken at 1 cm, 3 cm, 5 cm, 7 cm, and 9 cm heights above the surface of a test substrate in 5 locations, spaced 3 cm on–center, along the length of the test specimen, parallel to air flow (x–axis in Figure 13). This was done for 5 discrete locations spaced 3 cm apart along the width of the substrate, perpendicular to air flow (y–axis in Figure 13), creating a 5 by 5 (12 cm by 12 cm) array centered about the test section. Note that x = 0 cm represents the lengthwise center of the mounted specimen, and a negative position indicates a distance away from this center against the air flow. Also, y = 0 cm represents the widthwise center of the specimen, and a negative position indicates a distance to the left of this center when looking with the direction of the air flow. For each of the 25 locations, the wind speed was averaged along the 5 height measurements, for simplicity of reporting. This full process was done for the 0.9, 1.4 and 2.4 m s^{-1} wind speeds and the height averaged flow profiles across the width of the wind tunnel for each x–axis position can be seen in Figure 14.

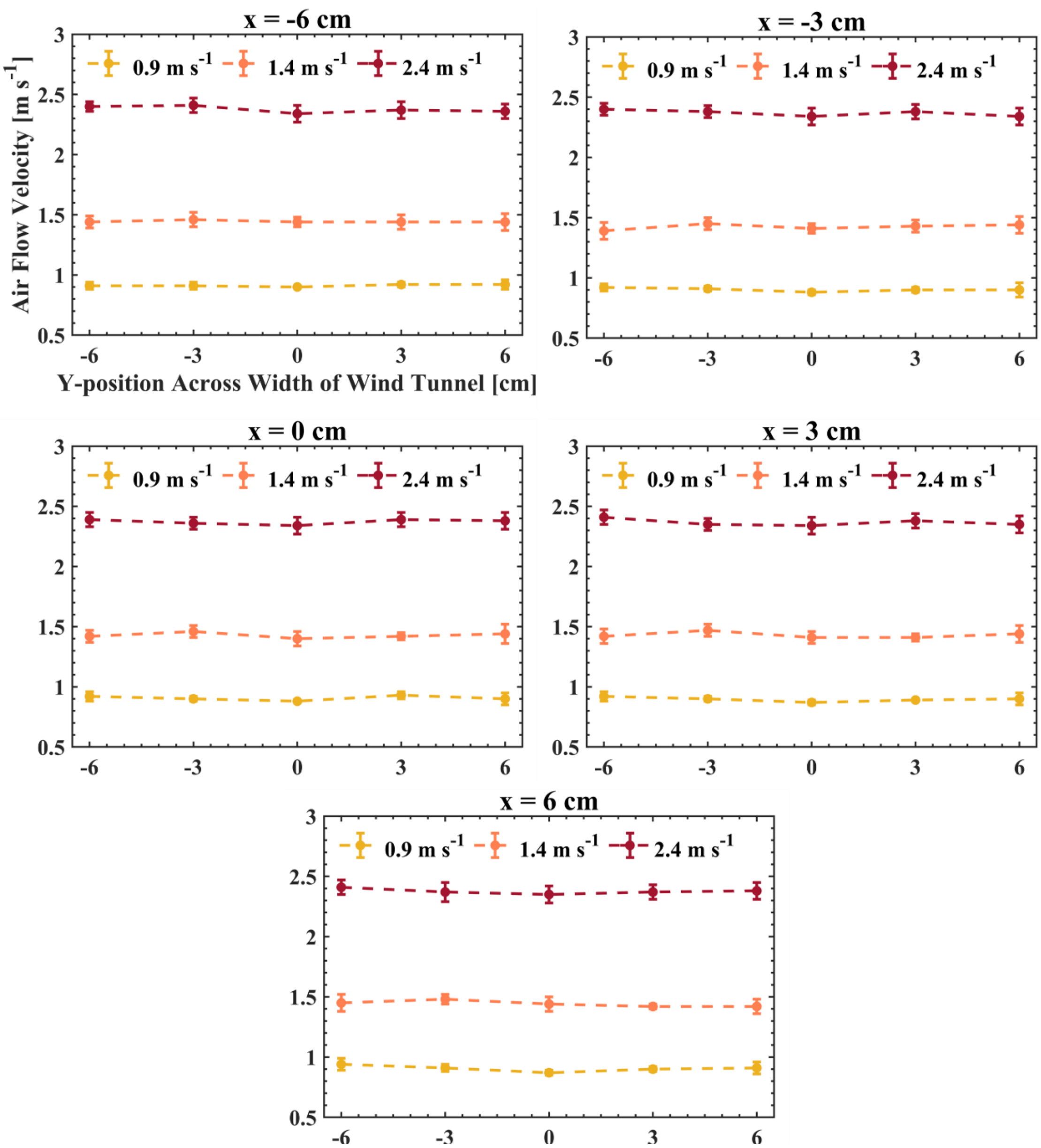

Figure 14: Height averaged flow profiles across the width of the wind tunnel at 0.9 m s^{-1}, 1.4 m s^{-1}, and 2.4 m s^{-1} wind speed settings for x = –6, –3, 0, 3, and 6 cm.

From Figure 14, the flow profile is uniform across the width of the wind tunnel at all three wind speeds. Although this was done with no firebrand pile present in the wind tunnel, this confirms the assumption that the entire leading edge of the pile is exposed to the set wind speed during tests. The wind profile varied in height by 6%, 5%, and 3% at most for the 0.9 m s^{-1}, 1.4 m s^{-1}, and 2.4 m s^{-1} wind speeds, respectively. This variation is largely due to the increased boundary effects at the surface of the test specimen, thus vastly decreasing the wind speed readings at the 1 cm height. Figure 15 provides the height variation of the wind tunnel flow profile for all three wind speed settings at the geometric center of the firebrand deposition area (x = 0 cm, y = 0 cm).

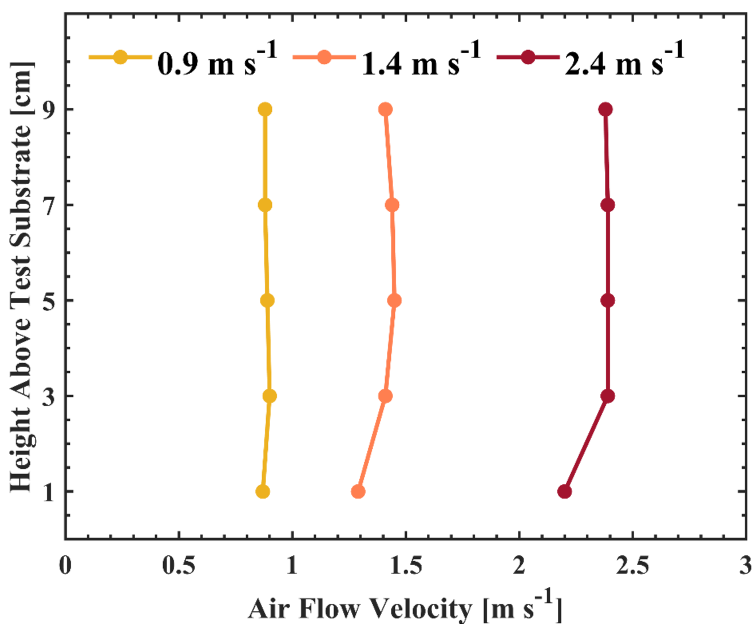

Figure 15: Height variation of air flow velocity at geometric center of firebrand deposition area (x = 0 cm, y = 0 cm).

The Reynolds number (Re) is a dimensionless quantity that represents the ratio of inertial forces to viscous forces within a flowing fluid and is defined in Equation (4) [94]. The Re represents if a flow has large inertial forces that can cause random and rapid fluctuations of the fluid, known as being turbulent, or if the viscous forces are large enough to suppress these fluctuations, known as being laminar. For flow in a circular tube, a flow is generally laminar for Re < 2300, fully turbulent for Re > 10,000, and translational in between these bounds [94].

$$Re = \frac{\rho v D_h}{\mu} \tag{4}$$

Where ρ is the density of the fluid, v is the average velocity of the fluid, D_h is a hydraulic diameter, and μ is the dynamic viscosity of the fluid. The Re of the flow within the test section was calculated using the 0.9, 1.4, and 2.4 m s^{-1} air flow velocities, ρ and μ as the density and viscosity of air at 25 ˚C (1.184 kg m^{-3} and 1.849×10^{-5} kg m^{-1} s^{-1} [94]) and the D_h calculated for a rectangular duct, found in Equation (5) [94].

$$D_h = \frac{2ab}{a + b} \tag{5}$$

With a being the height of the rectangular duct (10 cm) and b as the width of the duct (26 cm). The Re for flow in the wind tunnel at the 0.9, 1.4, and 2.4 m s^{-1} air flow velocities were 8.33×10^3, 13.0×10^3, and 22.2×10^3, respectively. Therefore, the flow in the wind tunnel is transitional for the 0.9 m s^{-1} air flow velocity and would be fully turbulent for the 1.4 and 2.4 m s^{-1} velocities provided that the turbulence has time to develop.

Despite the presence of the contraction cone, an engineering rule–of–thumb for the entry length of a turbulent flow is 10 hydraulic diameters [94], which the geometric center of the firebrand deposition area is about 1.5 diameters. Given this, the flow is still developing inside of the test section of the wind tunnel, however, is uniform (shown in Figure 14) and is straightened with lowered turbulent intensity from the contraction cone and multi–layer honeycomb mesh design [95, 96].

2.3.2 NDIR Gas Analyzer

To convert the voltage output of the NI–9215 module to a volumetric percentage, a calibration curve is required to capture the relation between these two–unit measurements. To obtain this curve, a 3 SLPM flow of known vol.% CO, CO_2, and Nitrogen (N_2) was passed into a 1 L plastic bottle chamber. Note this 3 SLPM rate was representative of rates produced and subsequently sampled by the gas probe during a test. The flow was passed through one end of the chamber and the red nylon tubing, originally attached to the open end of the gas sampling probe, was attached to the other end which still used the suction pump to sample the constituents of the chamber. This bottle–chamber setup accounted for any disturbances from the pump or soot filter during the calibration process. The flow was, by volume, 8.0% CO_2, 0.8% CO, and 91.2% N_2 controlled by an Alicat Scientific MC–500SCCM–D/5M mass flow controller which was diluted by a flow of 100% N_2 controlled by an Alicat Scientific MC–10SLPM–D/5M mass flow controller to obtain a range of about 0 – 0.04 vol.% for CO and 0 – 0.4 vol.% for CO_2. A MesaLabs Definer™ 220 series air flow calibrator was used to validate the flow rates controlled by the MC–500SCCM–D/5M and a MesaLabs Defender™ 530+ series air flow calibrator was used for the MC–10SLPM–D/5M.

For each vol.%, recording on LabVIEW of the voltage outputs for CO and CO_2 began and 100% N_2 was introduced into the analyzer for 40 seconds to purge the system. A pre–determined flow rate of the CO/CO_2 was then introduced for 100 seconds so an average voltage output value for these concentrations could be gathered. The supply of the CO/CO_2 was closed and the 100% N_2 continued to purge the system. This process was done at the ranges of 0 – 0.04 vol.% for CO and 0 – 0.4 vol.% for CO_2 and repeated on three separate days to ensure that this curve was repeatable. Figure 16 shows the average voltage to vol.% curves used in all tests for CO and CO_2, respectively. Note that both curves follow a linear trend for large voltages, however, begin to follow a nonlinear trend for voltage signals less than 0.05 V for CO and less than 0.03 V for CO_2.

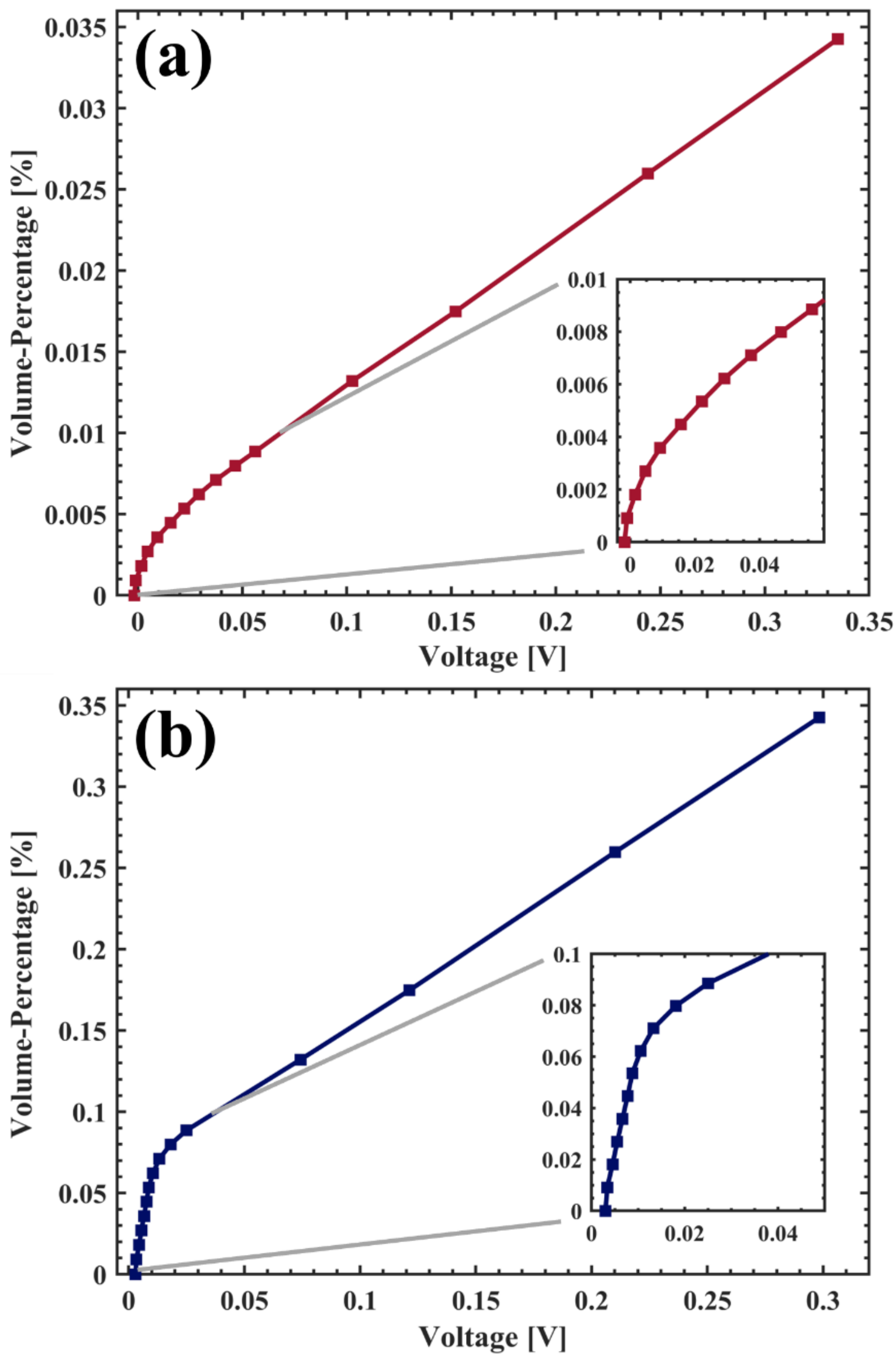

Figure 16: Average voltage to vol.% curves for CO (a) and CO_2 (b) used in this study to measure wind tunnel exhaust flow constituent concentrations.

2.3.3 IR Measurement System

To analyze temperature data gathered from the FLIR IR camera, the FLIR Tools software was used. This program required two inputs before data could be accurately processed, the total distance from the IR camera's lens to the back surface of the substrate (0.4 m) and the emissivity (ϵ) of the black optical coating after being applied to the respective test specimen.

The process of finding the emissivity for each canister of the optical black coatings used, began with preparing one Kaowool specimen and one WRC specimen for each canister. After the samples were painted and dried, a 0.127–mm diameter bead K–type thermocouple was placed on the same face of the calibration specimen that the optical black coating was applied, as depicted in Figure 17. The thermocouple was connected to a NI–9213 C Series Temperature Input Module (± 78 mV) which read the voltages from the thermocouple at 6 Hz and was collected using LabVIEW.

The IR camera and gold mirror design described in Section 2.1.3 allowed for the entire apparatus to be detached from the wind tunnel and placed under a conical heater. This heater was used to produce temperature at the top surface while the back–surface temperature of the substrate was monitored using both the 0.127–mm thermocouple and the IR camera. An 18 cm by 14 cm piece of the Kaowool insulation with a 2.5 cm by 2.5 cm square hole cut out in the center was placed on top of the calibration specimen, shown in Figure 17, to minimize the length of the thermocouple wiring exposed to the radiant heat source. This allowed for only the small section where the thermocouple bead and IR measurements were taken on the backside to be completely exposed to the heater.

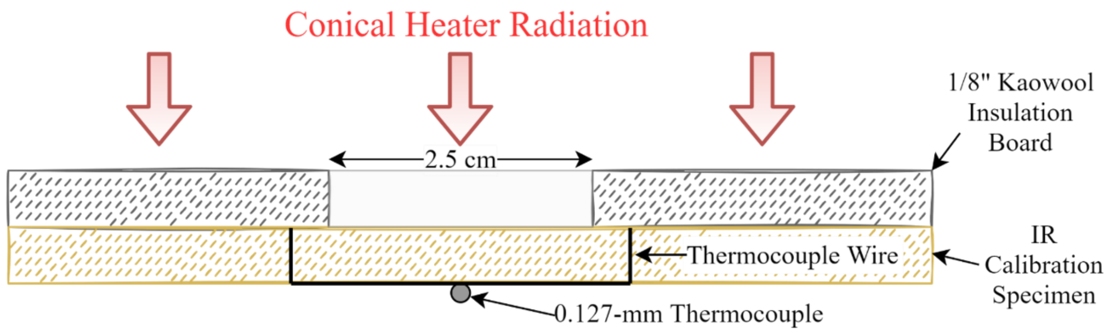

Figure 17: Side view–diagram of IR calibration specimen (not to scale). Note that the hatching represents that the diagram is cut halfway through the specimen.

The calibration specimen was mounted so that the coated back surface was 40 cm away from the FLIR IR camera, which was consistent with that of the wind tunnel setup. The calibration apparatus was raised until the distance from the top surface of the specimen to the bottom of the conical heater was 2 cm. This distance correlated to a heat flux of 85 kW m^{-2}, measured separately with a Smith–Boelter water–cooled heat flux gauge, when the heater was at a temperature setting of 891 °C. For the Kaowool specimen calibrations, three temperature settings were tested, 300 °C, 600 °C and 891 °C. This was done to establish whether the emissivity of each canister was temperature dependent. Also, the 300 °C, 600 °C, and 891 °C heater settings corresponded to 100 °C, 250 °C, and 390 °C back surface temperatures, respectively. Although some preliminary tests yielded back surface temperatures > 400 °C, 891 °C was the highest heater setting that could be safely controlled. Therefore, the quantified–operating range of each calibrated canister of the optical coating was 100 – 390 °C.

For a calibration test, the specimen was shielded by the shutter while the heater was allowed to stabilize at a temperature of 300 °C. Once this setting was reached, recording on LabVIEW and the IR camera began. After 35 seconds, the shutter was removed, exposing the substrate for 165 seconds. The shutter was then re–inserted, temperature data gathering was stopped, and the cone was set to 600 °C. The process was repeated at the 600 °C setting and then again at 891 °C. This process was completed for each Kaowool specimen coated with the optical coating from different canisters.

The FLIR Tools program was used to take four spot measurements (3 x 3–pixel array, 9 pixels total per measurement) around the thermocouple bead, using a set emissivity. These four measurements were averaged and compared to the thermocouple readings for the same temperature setting. The emissivity was modified until the IR and thermocouple temperature measurements agreed per temperature setting. Figure 18 shows the IR temperature data using an $\epsilon = 0.94$ compared to the respective thermocouple data for canister 1. The emissivity for each optical black coating canister used when applied to Kaowool, was found, and used for all tests as 0.94. This value slightly changed from the 0.95 value listed on each canister, however, did not change over the temperature range considered, or over the multiple canisters of the optical coating used throughout this study.

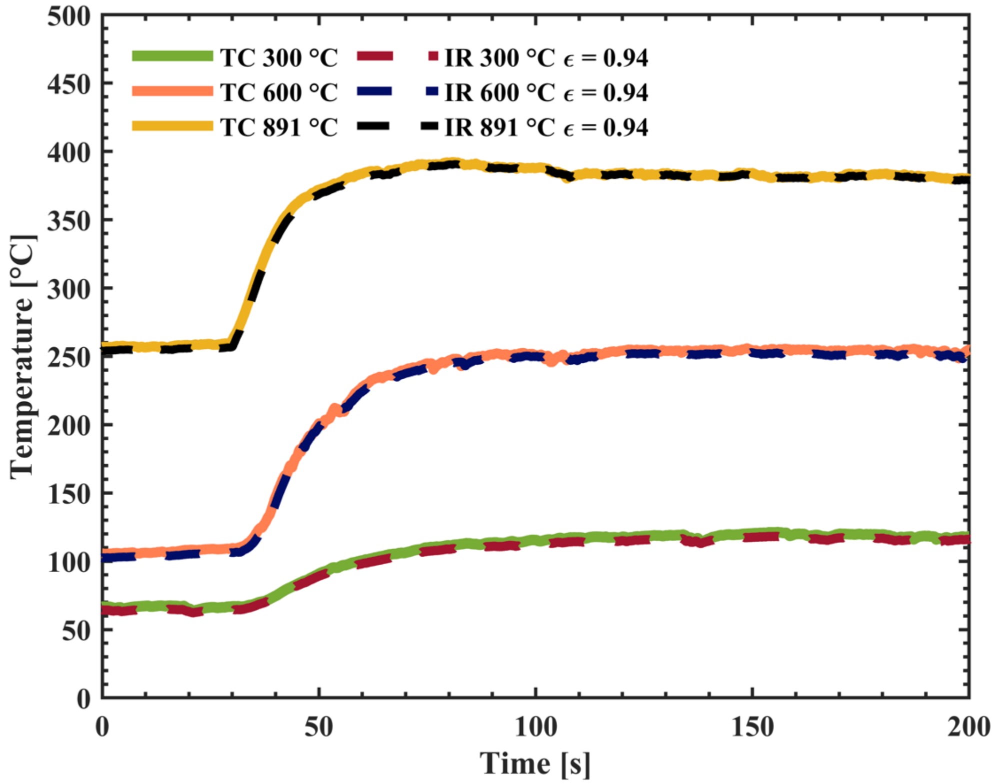

Figure 18: Back surface temperature data for IR calibration tests of canister 1 applied onto Kaowool substrate. Note that each temperature setting's TC and ϵ = 0.94 IR profiles follow closely together.

The same process was used for the WRC calibration samples, however only the 891 °C setting was used. Only one temperature setting was considered because the specimen's top surface would eventually ignite for each of the three settings considered for the Kaowool samples. This ignition would not allow for multiple temperature settings to be investigated on a single specimen. The emissivity for all canisters, when applied to WRC, was found, and used for all tests as 0.92. This method of calibrating IR cameras by comparing IR temperature measurements to surface imbedded thermocouple readings has been done in previous studies [97, 98] and is also done in calibration for CAPA II experiments [81].

2.4 Test Procedure

At the beginning of all test days, the CAI ZPA NDIR gas analyzer was span calibrated and zeroed using the 8.0% CO_2, 0.8% CO bottle and the 100% N_2 bottle, respectively. This was done to provide a consistent baseline across all test days and to account for any drift of the NDIR sensors when not in use, prior to the voltage to vol.% curves, found in Figure 16, being applied. After the height of the sample holder was correctly adjusted such that the substrate would be flush with the inside of wind tunnel, the specimen was placed into the sample holder. The sample was then mounted within the wind tunnel as depicted in Figure 19. The gold mirror and IR camera were placed into their respective locations. The wind tunnel fan was then switched on and the top opening that is covered by the piece of borosilicate glass during tests, see Figure 6, was covered with a piece of plywood with a single hole drilled through it such that an Omega HHF–SD1 Hot Wire Anemometer could be inserted into the middle of the test chamber and the air flow velocity was measured about 3 cm above the surface of the substrate.

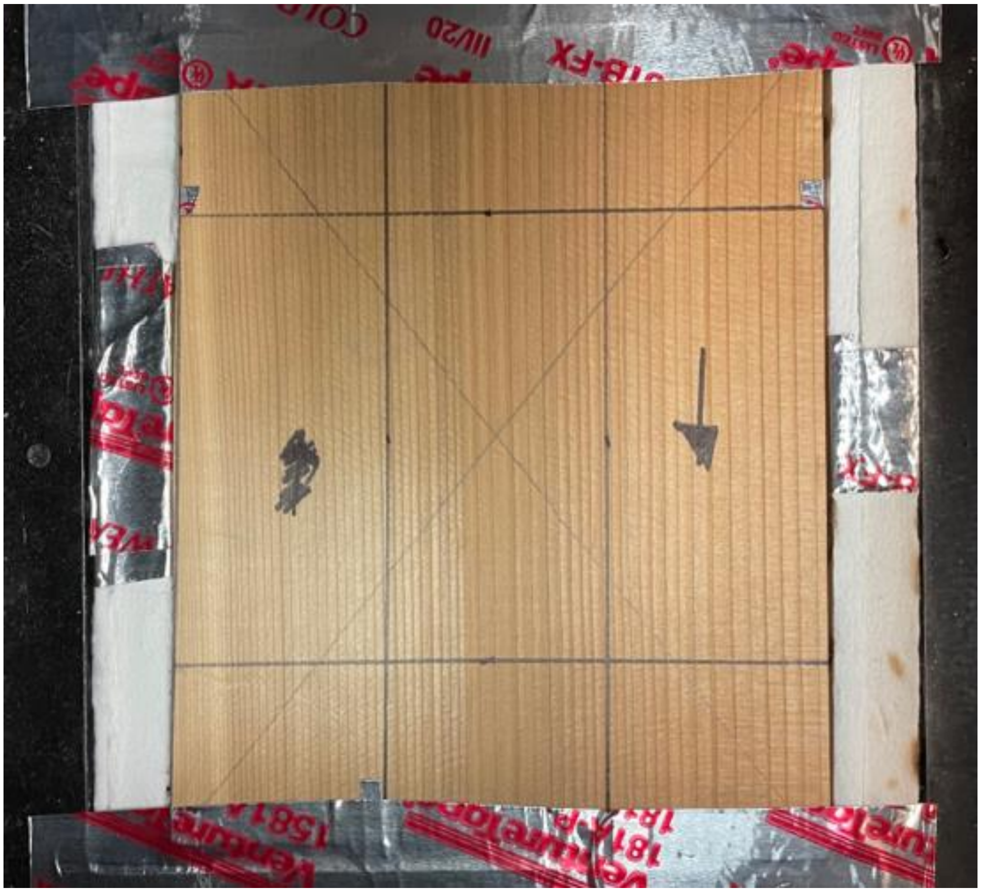

Figure 19: Top view of wind tunnel mounted WRC specimen. Note the use of Kaowool spacers and aluminum foil tape to cover openings in the sample mount. Before each test, foil tape was also added to cover the gaps the Kaowool spacers could not fill.

Roughly two minutes after the air flow velocity was set to either 0.9 m s^{-1}, 1.4 m s^{-1}, or 2.4 m s^{-1}, the anemometer was inserted a second time to ensure the flow velocity did not drift and was still at the predetermined condition. The cover was removed, and the fire brand deposition funnel was placed within the marked deposition area. This Omega anemometer was also used to record the wind speed at varying points of the contraction cone's inlet, over multiple tests, to monitor if there was a change in the wind speed when the wind tunnel is first sealed at the beginning of a test or throughout the entire duration of the test. None of these possible changes were observed.

Data acquisition of the gas analysis system was initiated as the dowels were placed onto the ignited–propane burner. The firebrand preparation steps explained in Section 2.2.2 were then followed. While the dowels were in a flaming state, recording on the side–profile Nikon D7100 camera, the Sony Alpha SLT–A55V top view camera, and FLIR IR camera was initiated. The firebrands in the mesh pan were deposited, through the deposition funnel, onto the substrate mounted in the wind tunnel. Once the firebrands were deposited, the funnel was lifted vertically out of the wind tunnel and the top mirror was lowered into place. The borosilicate glass was then slid over the top opening, thus sealing the wind tunnel, and exposing the firebrand pile to the set air flow velocity. This indicated the start of the respective wind tunnel test, and a time of zero seconds. Figure 20 shows the entire experimental set up during a WRC 0.16 g cm^{-2} coverage density, 1.4 m s^{-1} air flow velocity test.

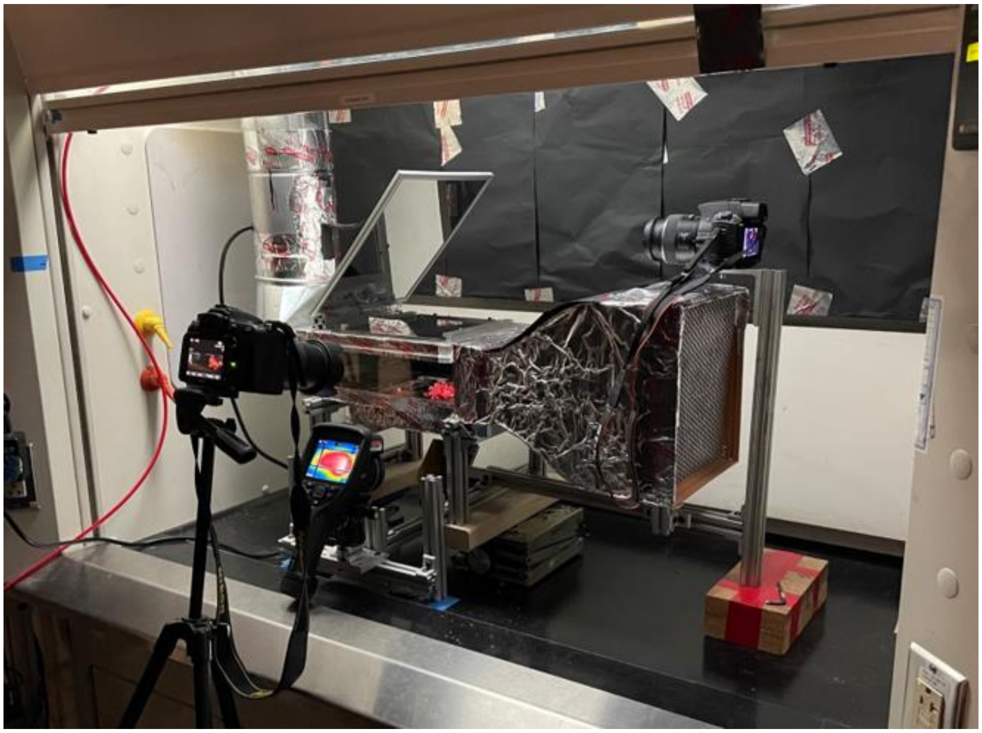

Figure 20: Full experimental setup during a WRC 0.16 g cm^{-2}, 1.4 m s^{-1} test. The setup was placed inside of a fume hood for all tests for proper ventilation of the exhaust duct constituents. Note the red tubing on the left side of the picture is leading from the gas sampling probe to the NDIR gas analysis system described in Section 2.1.2.

Chapter 3: Results and Analysis

For the presentation and analysis of the results from this study, the 3 g and 8 g firebrand pile tests were labeled as their respective coverage densities, 0.06 g cm^{-2} and 0.16 g cm^{-2}. These 0.06 and 0.16 g cm^{-2} coverage densities are similar to those investigated in the Salehizadeh *et al*. [59] and Tao *et al*. [60] studies. Table 2 provides the test matrix from this study considering both the coverage densities and the different air flow velocities set in the wind tunnel. It should be noted that the 0.16 g cm^{-2}, 0.9 m s^{-1} testing condition was investigated to validate ignition trends found during the ignition study considering the 1.4 m s^{-1} and 2.4 m s^{-1} air flow velocities. Also, the "Common Flaming Ignition Zone Tests" were conducted to better quantify the thermal conditions experienced in the region where flaming ignition frequently occurred.

Table 2: Test matrix from this study. A total of 90 wind tunnel tests were conducted.

Test Substrate	Coverage Density [g cm^{-2}]	Air Flow Velocity [m s^{-1}]	# of Firebrand Deposition Area Tests	# of Common Flaming Ignition Zone Tests
Kaowool PM	0.06	1.4	6	3
		2.4	6	3
	0.16	0.9	6	3
		1.4	6	3
		2.4	6	3
WRC	0.06	1.4	6	3
		2.4	6	3
	0.16	0.9	6	3
		1.4	6	3
		2.4	6	3
		Total	**60**	**30**

3.1 Thermal Analysis of Firebrand Deposition Area

3.1.1 Analysis Procedures

Six tests for the five different testing conditions (30 Kaowool and 30 WRC tests, 60 in total) were conducted to gather back surface temperature profiles. The temperature data recorded by the FLIR IR camera was processed in the FLIR Tools software mentioned in Section 2.3.3. From the Kaowool tests, it was noted that the hot spot of the firebrand pile traveled from the front edge of the firebrand pile to the middle of the deposition area as the test progresses (i.e., from right to left in Figure 21).

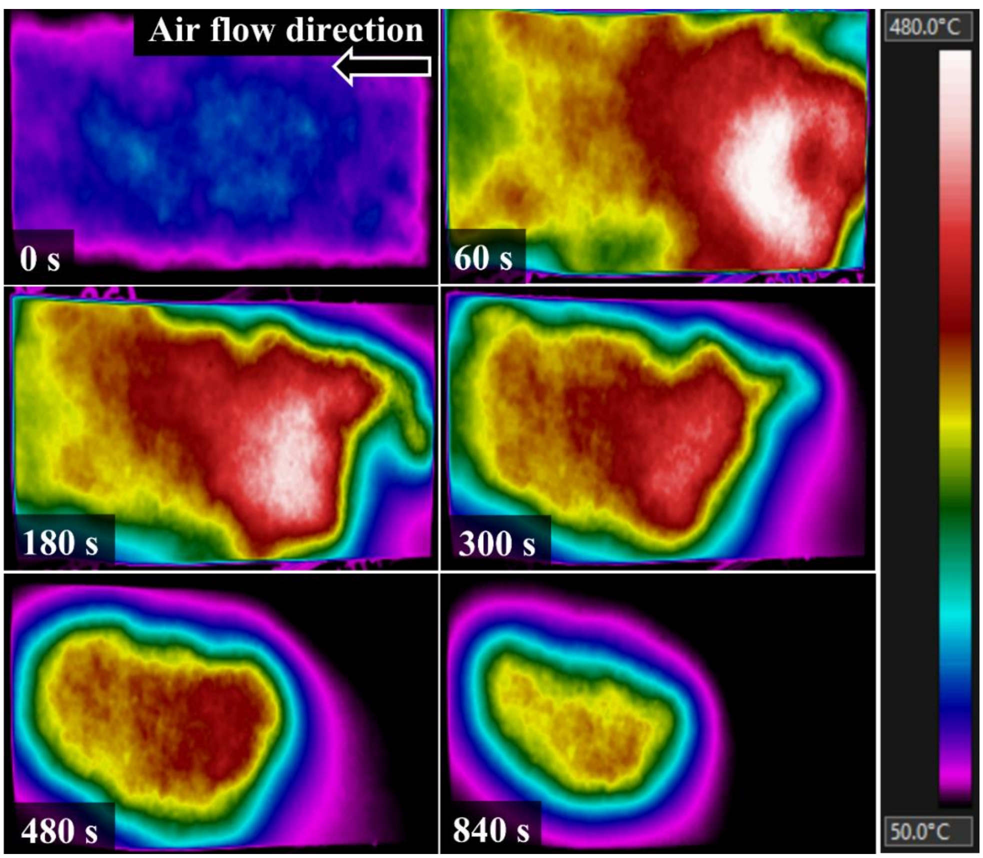

Figure 21: Thermal footprint timeline of firebrand pile during a 0.16 g cm^{-2} coverage density, 2.4 m s^{-1} air flow velocity Kaowool substrate test.

The hot spot temperature of the firebrand pile moved in the direction of the air flow velocity as the test progressed. From this observation, the 50 cm^2 firebrand deposition area outlined in the aluminum foil tape on the back surface of the substrate was divided into a leading and middle 4 cm by 3 cm zone. The edges of the pile were not considered for this analysis due to variations in the loading size at the edge of each firebrand pile. Therefore, the leading and middle zones were centered about the width of the area outlined by the foil tape, with 0.5 cm on each side. The leading–edge zone was placed 0.5 cm from the right–hand side vertical foil tape that represented the leading edge as shown in Figure 22. Inside each zone, 30 spot measurements were taken as shown in Figure 22. Each spot measurement considered a 3 x 3–pixel array, with 9 pixels in total.

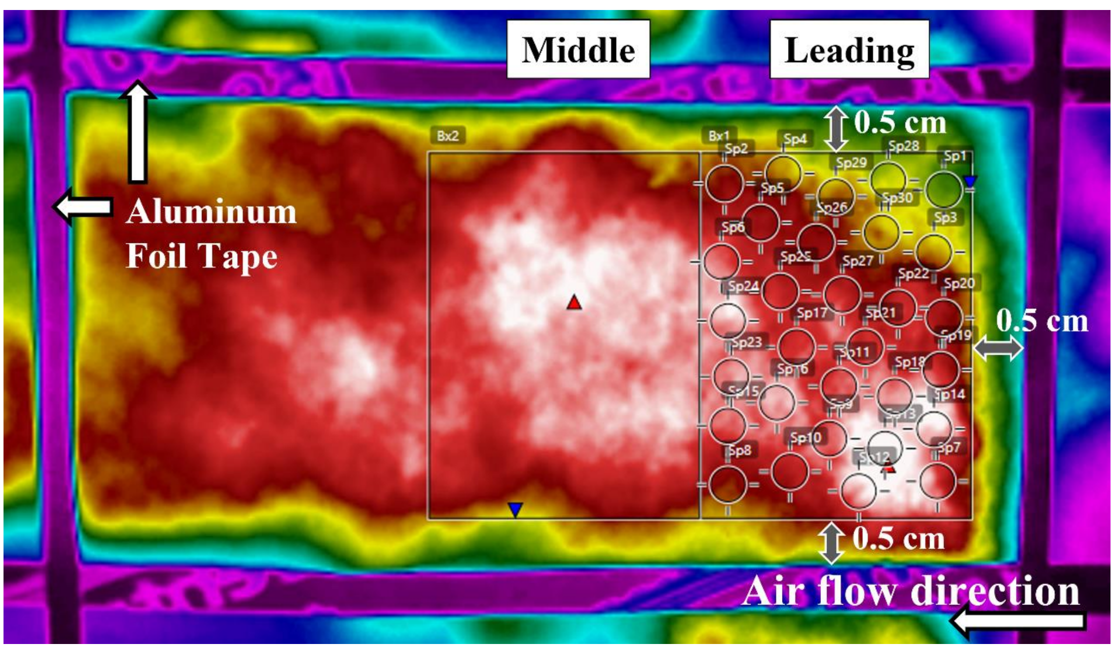

Figure 22: Screenshot from the FLIR Tools software highlighting both the leading and middle zones for a representative Kaowool sample, and the spot measurement placement within the deposition area outlined in aluminum foil tape.

To minimize the processing time used to generate temperature data while still accurately representing the two zones, an analysis on the number of spot measurements used to represent a leading zone was conducted. Figure 23 shows a comparison of selecting 10, 20, and 30 spot measurements to represent the average back surface temperature for the same leading zone from a 0.16 g cm^{-2} coverage density, 2.4 m s^{-1} air flow velocity Kaowool substrate test. Note that the 30–measurement average lies in–between the 10 and 20 averages. Thus, 30 spot measurements best represented the temperature profile of the zone, while the 10 over– and the 20 under–predicted the average. Similar plots were made for the minimum and maximum temperature readings of this zone. Both the minimum and maximum profiles did not change when selecting 20 or 30 points, therefore the absolute difference from the maximum and minimum values began to converge at 30 points. As a result of these findings, 30 spot measurements were selected when measuring the back–surface temperature of the leading and middle zones for both the Kaowool and WRC substrates.

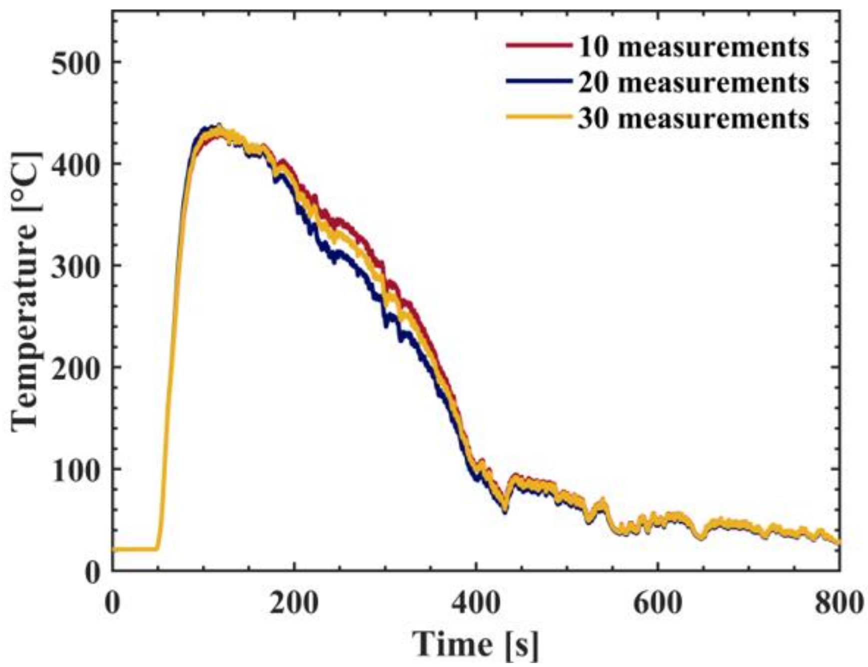

Figure 23: Average temperature profiles from 10, 20, and 30 spot measurements taken from the leading zone of a 0.16 g cm^{-2}, 2.4 m s^{-1} Kaowool substrate test.

The temperature data from each individual test was binned every 12 seconds to smooth out the profiles. The average back surface temperature profile for each set of conditions was taken as the average back surface temperature considering each individual back surface temperature profiles (i.e., six in total for each testing scenario). The variation for all average temperature profiles was represented using Equation (3), with n being the number of individual tests considered for the average profile.

3.1.2 Firebrand Pile Thermal Characterization Results and Discussion

The average leading and middle zone temperature profiles with their respective variation for the 0.06 and 0.16 g cm^{-2} coverage densities at an air flow velocity of 1.4 m s^{-1} on the Kaowool substrate can be seen in Figure 24 and Figure 25, respectively. Similar plots for the other three conditions can be found in Figures A.1 – A.3 in

Appendix A. Note that a time of zero seconds was defined as the time when the top piece of borosilicate glass was slid over the top of the wind tunnel, completely sealing the tunnel, and exposing the firebrand pile to the predetermined air flow velocity.

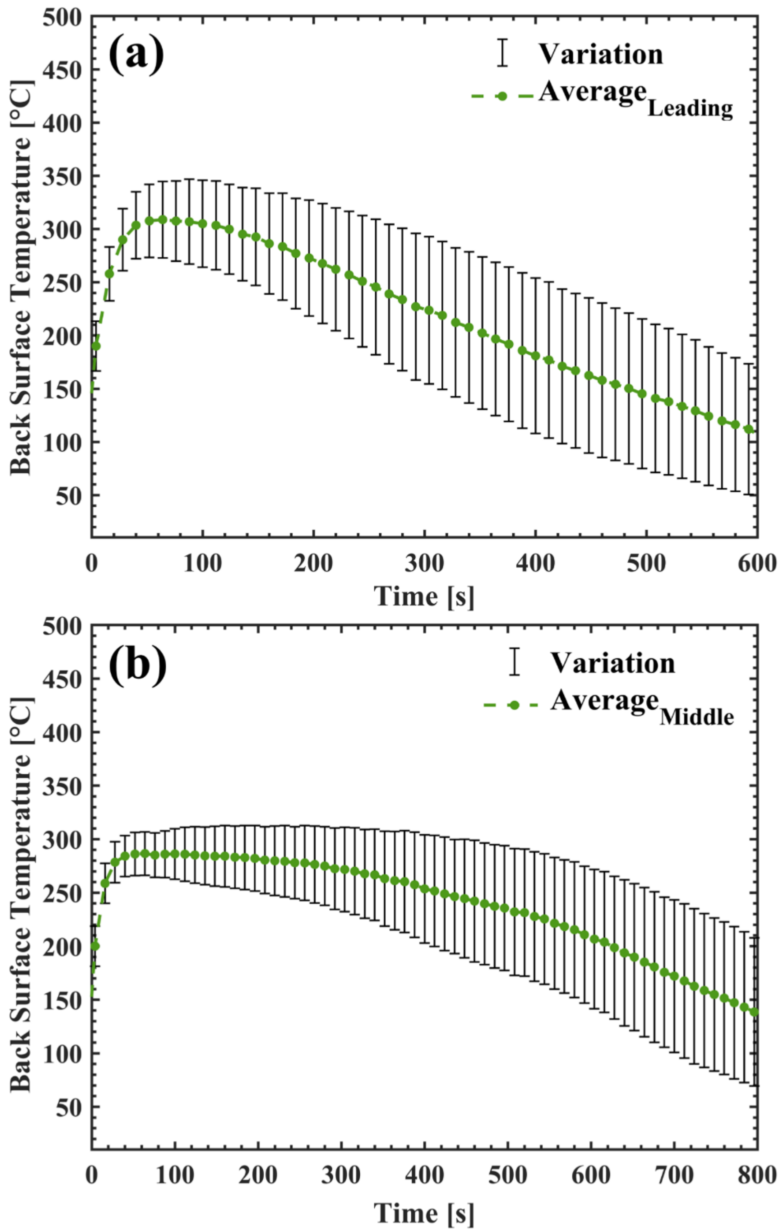

Figure 24: Average leading (a) and middle (b) zone temperature profiles for the 0.06 g cm^{-2} coverage density at the 1.4 m s^{-1} air flow velocity on the Kaowool substrate. These average curves consider six tests.

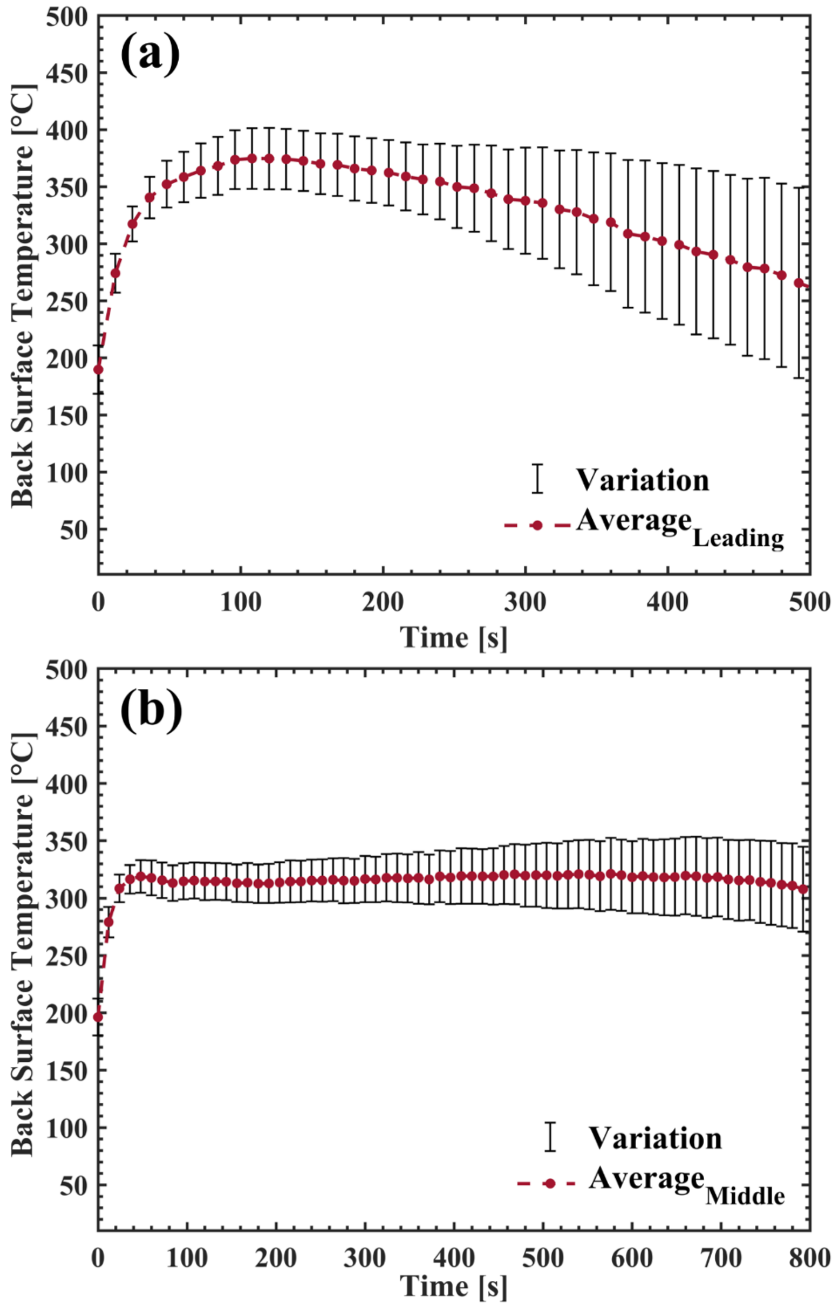

Figure 25: Average leading (a) and middle (b) zone temperature profiles for the 0.16 g cm^{-2} coverage density at the 1.4 m s^{-1} air flow velocity on the Kaowool substrate. These average curves consider six tests.

For all five testing conditions on the Kaowool substrate, the average leading and middle zone temperature profiles rapidly increased soon after the firebrands were deposited, and the wind tunnel was sealed. The temperature of the leading zone rapidly increased to a peak value then gradually decreased, while the back–surface temperature of the middle zone peaked at a lower temperature and decayed at a lower rate than that of the back surface temperature of the leading zone. The average leading and middle back surface temperature profiles from the two conditions shown in Figure 24 and Figure 25 validate the observation that the leading zone rapidly increases to an elevated peak value, and then gradually decreases shortly after the peak is reached. Also seen from both testing conditions (more apparent in Figure 25), the middle zone stays at a slightly lower peak temperature for a longer duration, when compared to the leading zone profile.

After deposition of the firebrands, it was noted that a layer of ash started developing on the surface of the firebrand pile, as shown in Figure 26. Wood ash has been found to have low thermal conductivity [99], which allows for it to be a good thermal insulator. Therefore, this ash layer possibly could have acted as a thermal insulator and a flow obstruction, both shielding the glowing firebrands in the middle zone from the air flow, as well as containing the heat produced by the firebrand pile. This layer typically began to form around 300 seconds into a test, which could explain why the middle zone temperature profiles remain at an elevated temperature for an extended duration (i.e., the firebrands in the middle of the pile loss heat at a slower rate when this ash layer formed, thus keeping the elevated temperature for a longer time).

Figure 26: Side view image from a 0.16 g cm^{-2} coverage density, 1.4 m s^{-1} air flow velocity Kaowool substrate test showing the formation of an ash layer over the pile.

As mentioned above, the average leading zone back surface temperature profile for all five conditions reached a visibly higher peak than that of the respective conditions average middle zone profile. To better quantify this comparison, an average peak temperature was taken as the mean of all peak back surface temperatures across each individual test at that set of conditions, for both the leading and middle zone. The variation was calculated using Equation (3). Table 3 provides the average peak back surface temperatures of the leading and middle zones for all five conditions from the Kaowool substrate tests.

Table 3: Average peak back surface temperatures of leading and middle zones from the Kaowool substrate tests for all five sets of conditions.

Testing Condition	Average Back Surface Peak Temperature [˚C]	
	Leading	Middle
0.06 g cm^{-2}, 1.4 m s^{-1}	309 ± 18	291 ± 10
0.06 g cm^{-2}, 2.4 m s^{-1}	353 ± 36	330 ± 14
0.16 g cm^{-2}, 0.9 m s^{-1}	332 ± 10	308 ± 6
0.16 g cm^{-2}, 1.4 m s^{-1}	378 ± 15	330 ± 12
0.16 g cm^{-2}, 2.4 m s^{-1}	417 ± 18	377 ± 12

From Table 3, the average peak back surface temperatures for the leading zone across all five testing conditions were 31 ± 11 ˚C higher than that of the respective middle zone's average peak temperature. An increase in either the coverage density or air flow velocity increased the average back surface peak temperature of a respective zone. An increase in the coverage density, by a factor of ⁸⁄₃, at the same air flow velocity increased the peak back surface temperature by 55 ± 14 ˚C, whereas an increase in the air flow velocity, by a factor of ¹²⁄₇, for the same coverage density increased the peak temperature by 42 ± 4 ˚C. From comparing these quantitative increases, air flow velocity seems to have the stronger influence on the peak back surface temperature of the inert substrate when exposed to the firebrand piles (i.e., doubling the air flow velocity would see a larger increase in the average back surface peak temperature than doubling the coverage density). Given the thin insulating Kaowool material, the dependence the peak back surface temperatures have with coverage density and air flow velocity is indicative of the heat exposure from the firebrand pile under these respective testing conditions.

3.1.3 Western Red Cedar Thermal Response Results and Discussion

The average back surface temperature profiles for the leading and middle zones with their respective variation for the 0.06 and 0.16 g cm^{-2} coverage densities, at the 1.4 m s^{-1} air flow velocity WRC substrate tests can be seen in Figure 27 and Figure 28, respectively. Similar plots for the other three conditions can be found in Figures B.1 – B.3 in Appendix B.

For all five testing conditions on the WRC substrate, the leading and middle zone back surface temperature profiles took in the range of approximately 100 – 200 seconds after the wind tunnel was sealed to start increasing from the ambient room temperature. Similar to the leading zone back surface temperature profiles of the firebrands on the Kaowool substrate in Section 3.1.2, the leading zone for these WRC tests reached a peak temperature and began to gradually decrease. In the Kaowool substrate tests, the leading zone peak was higher than that of the middle, however for these WRC tests, the middle zone reached a peak back surface temperature equal to or slightly higher than that of the leading edge. This is likely due to a longer heating duration in the middle zone, compared to the leading, due to the delayed exposure to the air flow. This increased duration allows for the heat of the firebrands in the middle zone to thermally penetrate the WRC board, long after the leading–edge firebrands have decomposed.

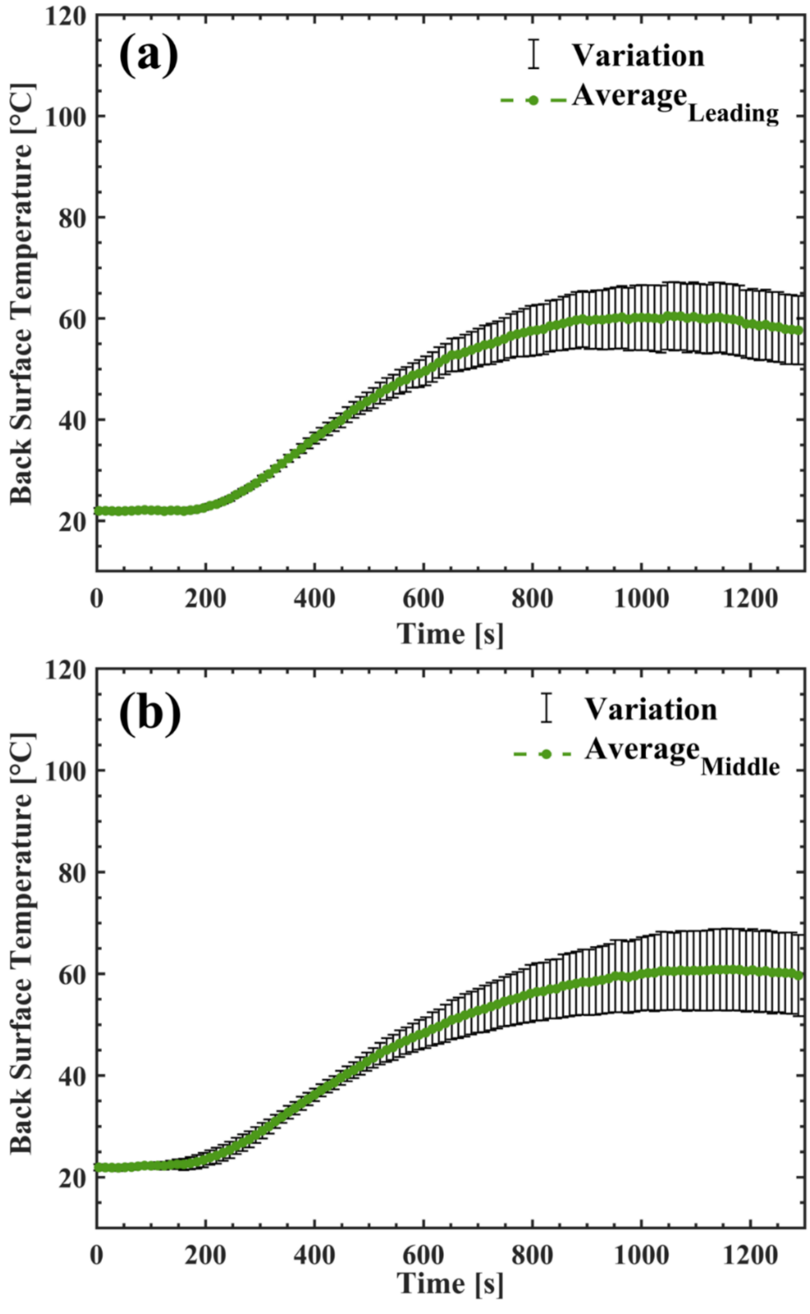

Figure 27: Average leading (a) and middle (b) zone temperature profiles for the 0.06 g cm^{-2} coverage density at the 1.4 m s^{-1} air flow velocity on the WRC substrate. These average curves consider six tests.

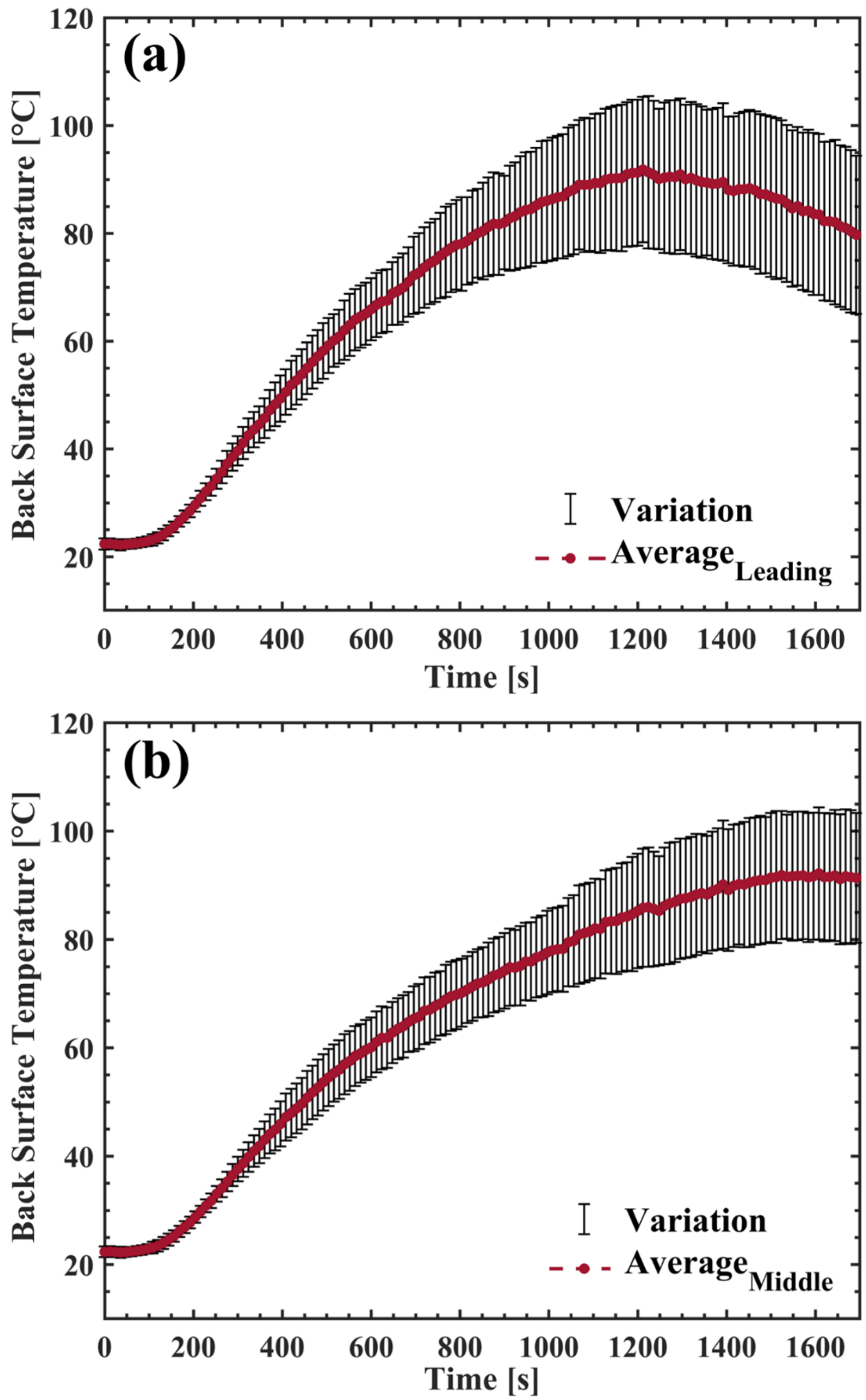

Figure 28: Average leading (a) and middle (b) zone temperature profiles for the 0.16 g cm^{-2} coverage density at the 1.4 m s^{-1} air flow velocity on the WRC substrate. These average curves consider six tests.

The average leading and middle zone back surface temperature profiles from these two conditions are representative of the observations made for all five testing conditions. These observations were that the leading zone slowly increases to a peak temperature, and then gradually decreases after this peak is reached. Also, as represented in both testing condition's middle zone back surface temperature profile, the middle zone profile reaches a peak value later in the test compared to the leading zone. Also, for a specific testing condition, the average peak value of the middle zone was higher than the respective leading zone. These peak temperatures visibly increased with an increase in both coverage density and air flow velocity.

Similar to that shown in Figure 26, the firebrands formed an ash layer over the top of the pile late into these WRC substrate tests. This observation can be seen in Figure 29. This ash layer again could have acted as an insulation barrier, shielding the glowing firebrands in the middle zone from the air flow, decreasing the heat losses from the firebrands, and allowing for more heat to penetrate through the substrate.

Figure 29: Side view image of a 0.16 g cm^{-2}, 1.4 m s^{-1} WRC substrate test showing the full formation of an ash layer over the pile 500 seconds after closing of the wind tunnel.

Given the thickness and thermal properties of the WRC, the time scale of heat transfer through this substrate is much larger than the time scale of combustion events occurring at the surface. Therefore, the peak temperatures from the WRC profiles would not be indicative of the heating intensity occurring at the surface where the firebrands are sitting. An average heating rate would better represent the thermal exposure at the surface of the WRC board and could allow for better comparison of the results from each set of testing conditions. The average heating rate was calculated using the central difference theorem considering the temperature data between when the respective average back surface temperature profile reaches 30 ˚C and 144 seconds after the temperature exceeded 30 ˚C. This temperature starting point was selected due to all average back surface temperature profiles following a linear trend in this region, shown in Figure 30. Table 4 provides the average heating rates of the leading and middle zones for all five conditions on the WRC substrate.

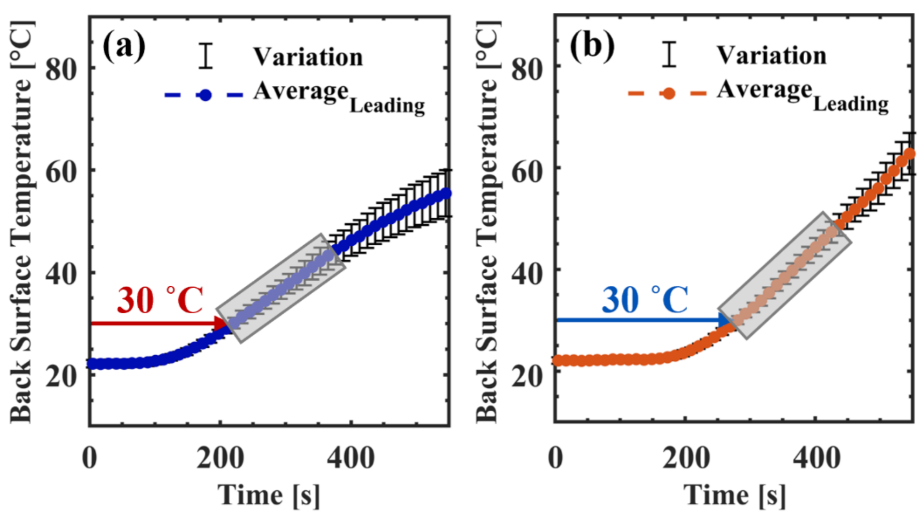

Figure 30: Representation of temperature and time range considered for calculating average heating rates from all five testing conditions on WRC. Average leading zone profiles from 0.06 (a) and 0.16 g cm^{-2} (b), 2.4 m s^{-1} testing conditions.

Table 4: Average heating rates of the leading and middle zones from the average back surface temperature profiles of WRC substrate tests for all five sets of conditions.

Testing Condition	Average Heating Rate [˚C s^{-1}]	
	Leading	Middle
0.06 g cm^{-2}, 1.4 m s^{-1}	$(81 \pm 3) \times 10^{-3}$	$(70 \pm 3) \times 10^{-3}$
0.06 g cm^{-2}, 2.4 m s^{-1}	$(92 \pm 3) \times 10^{-3}$	$(93 \pm 3) \times 10^{-3}$
0.16 g cm^{-2}, 0.9 m s^{-1}	$(76 \pm 2) \times 10^{-3}$	$(66 \pm 2) \times 10^{-3}$
0.16 g cm^{-2}, 1.4 m s^{-1}	$(103 \pm 6) \times 10^{-3}$	$(91 \pm 3) \times 10^{-3}$
0.16 g cm^{-2}, 2.4 m s^{-1}	$(120 \pm 5) \times 10^{-3}$	$(105 \pm 4) \times 10^{-3}$

From Table 4, the average heating rate from the back–surface temperatures for the leading zone across all five testing conditions were $(9 \pm 5) \times 10^{-3}$ ˚C s^{-1} higher than that of the respective middle zone's average heating rate. An increase in either the coverage density or air flow velocity increased the average heating rate of a respective zone. An increase in the coverage density, by a factor of ⁸⁄₃, at the same air flow velocity increased the heating rate by $(21 \pm 7) \times 10^{-3}$ ˚C s^{-1}, whereas an increase in the air flow velocity, by a factor of ¹²⁄₇, at the same coverage density increased the heating rate by $(16 \pm 5) \times 10^{-3}$ ˚C s^{-1}. From comparing these quantitative increases, air flow velocity seems to have the stronger influence on the average heating rate of the WRC board from the firebrand pile, with the leading zone being heated slightly faster than the middle zone.

3.2 Flaming Ignition Study

3.2.1 Analysis Procedures

All 90 tests were used to gather ignition statistics related to the ignition time as well as the burn duration for each test if ignition was visually noted. Ignition was defined as the visual presence of a sustained flame, and flame extinction was identified as the first absence of a visual flame from the top or side view DSLR video recordings. During the visual analysis of the video recordings from the two DSLR cameras, three flaming ignition scenarios were observed. These scenarios were labeled as "Firebrand Ignition on Kaowool," "Firebrand Ignition on WRC," and "WRC Surface Ignition." Examples of each scenario can be found in Figure 31, Figure 32, and Figure 33, below.

The "Firebrand Ignition on Kaowool" scenario, Figure 31, was the easiest to identify and was defined as any blue colored flame originating at the exterior surface of the firebrand pile during the Kaowool substrate tests. The "Firebrand Ignition on WRC" scenario, Figure 32, was defined similar to that on the Kaowool substrate as a flame originating on top of a firebrand or the pile. These flames looked similar to the firebrand ignitions of Kaowool, however transitioned from a blue color at the base of the flame to an orange tip. Finally, the "WRC Surface Ignition" scenario, Figure 33, was defined as a flaming ignition event originating and spreading along the surface of the WRC substrate and away from the initial deposition area. These flames were easily identified if the flame traveled away from the original ignition location either laterally or against the air flow. Also, these flames from a WRC ignition were typically more orange/yellow in color and were visibly brighter compared to the flames in the other two ignition scenarios. Note that in Figure 32, although the flame on the side of the pile at 15 s (see arrows) looks to be on top of the WRC board and char forms on the board, this was still considered a "Firebrand Ignition on WRC" as the flame did not transition into the bright orange/yellow color seen in the "WRC Surface Ignition" scenario, nor detach from the firebrand it originated from.

The ignition events that occurred first (i.e., primary ignitions) were considered for the time to ignition and burn duration data. These primary ignitions generally occurred within the first 70 seconds after the borosilicate glass was slid into place. Secondary ignitions would generally occur well after this time and would artificially shift ignition statistics like time to ignition. Time to ignition and burn duration are two flammability parameters that represent how quickly a combustible material will ignite, and how long it can sustain a flame. Instances where a material can ignite quickly and sustain flaming for an extended duration pose a large risk of igniting secondary nearby fuels like siding and soffit materials of homes, described in Section 1.1.3. It should be noted that some tests had more than one ignition event in different locations within 5 seconds of one another, and both were recorded as two separate ignition events. The ignition probability was established as the percentage of one occurrence of a given ignition event per test, over the total amount of tests considered at that set of conditions. Ignition probability represents the likelihood for ignition to occur for a given testing condition. Whereas the time to ignition and burn durations only considered the total number of occurrences of the respective ignition scenario, allowing for multiple times to be gathered from one test. Also, the time to ignition and burn duration did not consider tests where no occurrence of the respective ignition scenario was observed.

The variation in the average times to ignition and average burn durations was calculated considering Equation (3). Where n was taken as the number of ignition events that were noted for a specific testing condition.

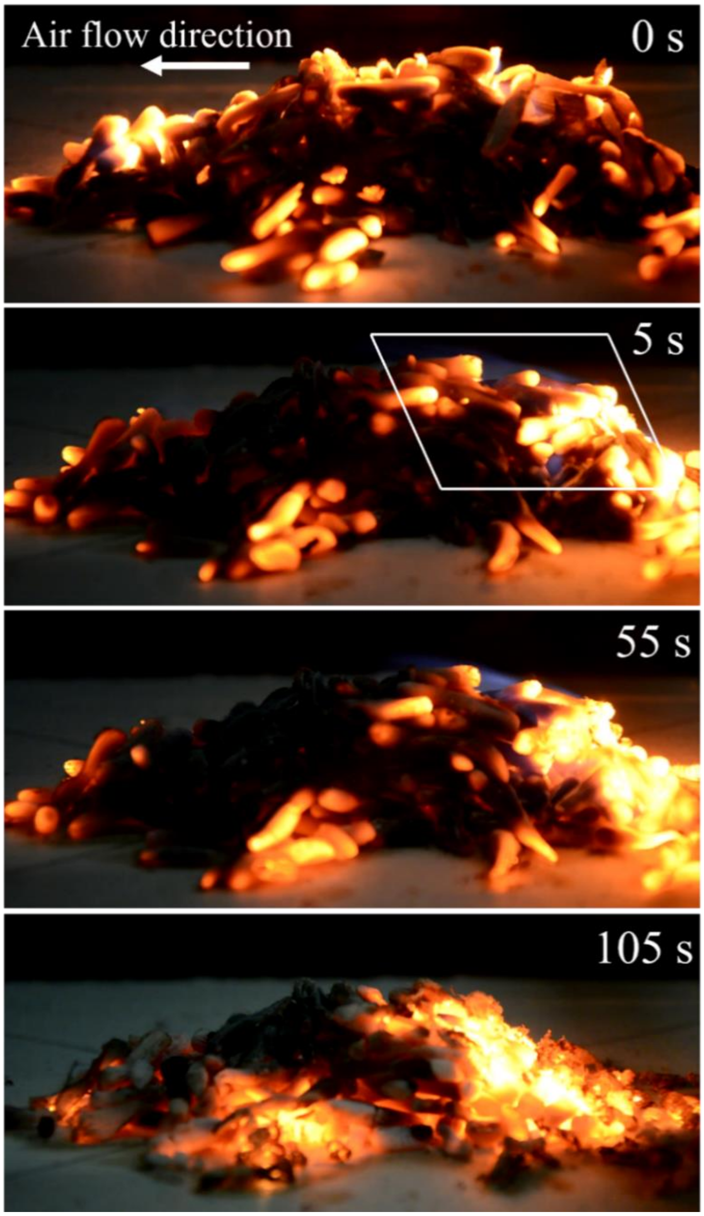

Figure 31: Example of "Firebrand Ignition on Kaowool" scenario. Note the formation of the entirely blue flame on top of the firebrand pile at the leading edge at 5 s. The flame for this 0.16 g cm^{-2}, 2.4 m s^{-1} test remained for 100 s before extinguishing.

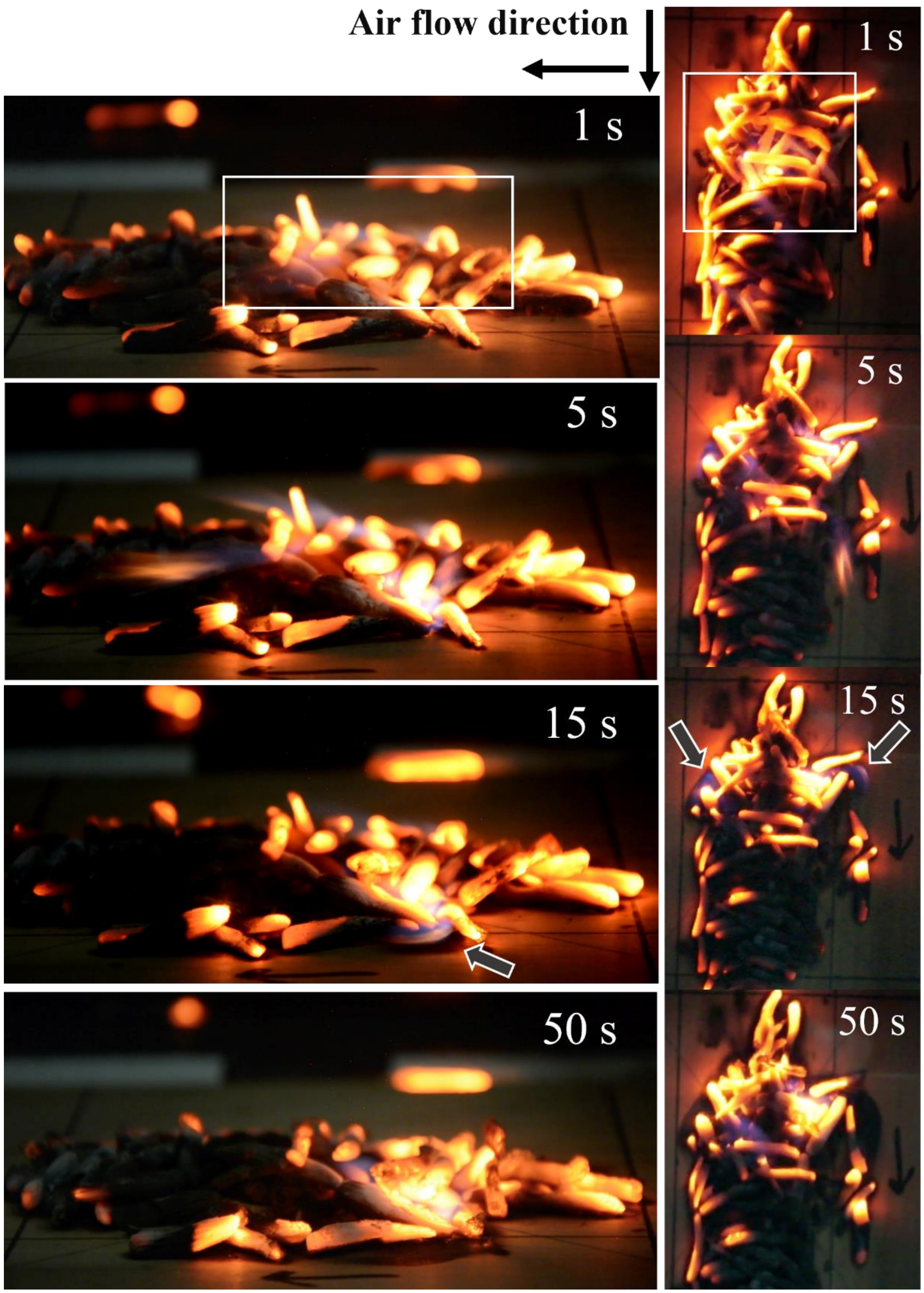

Figure 32: Example of "Firebrand Ignition on WRC" scenario. Note the formation of flames on top of the pile at 1 s. Brightness of the flame increased and the orange tips arose at 5 s during this 0.06 g cm^{-2}, 2.4 m s^{-1} test.

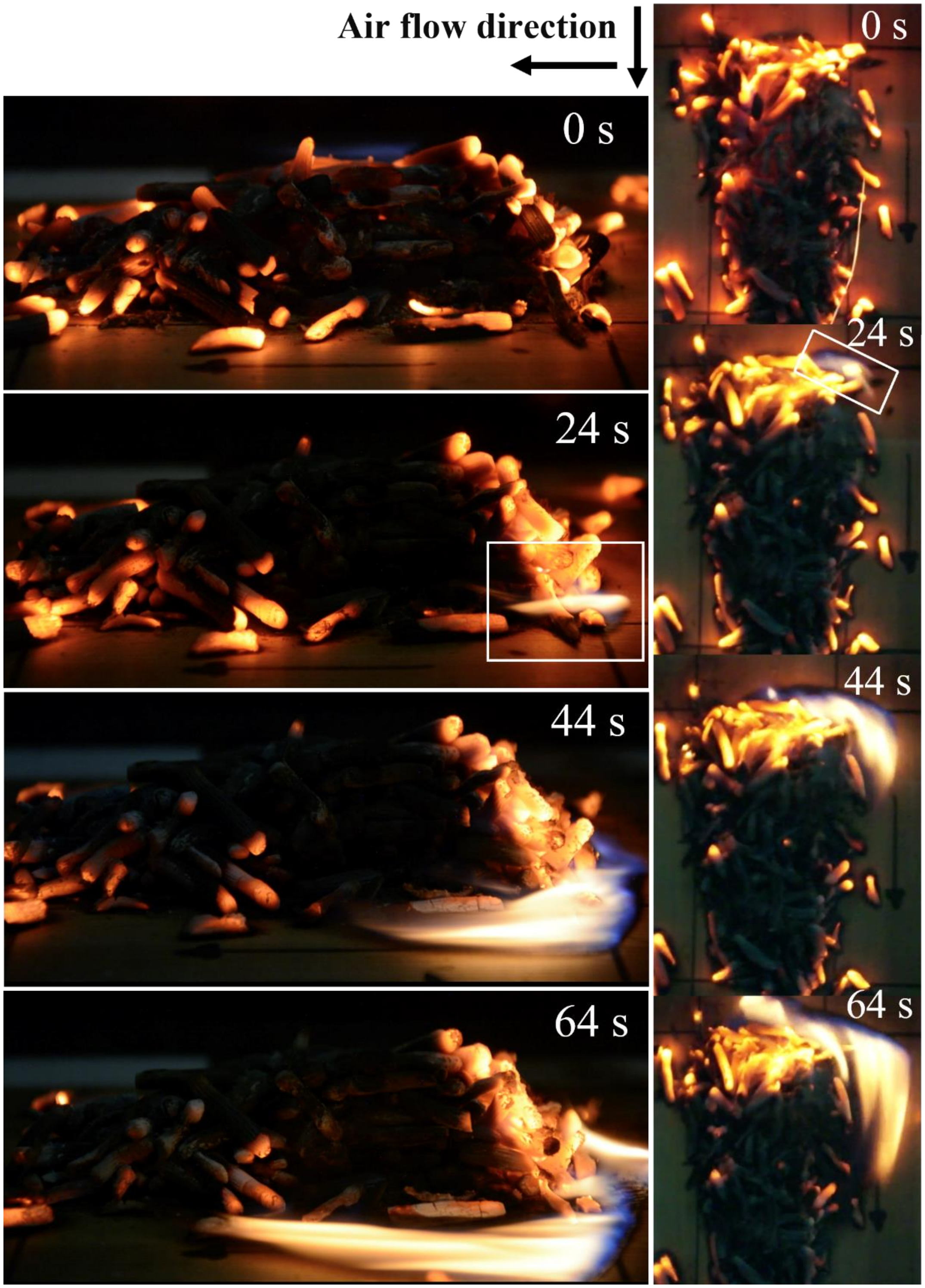

Figure 33: Example of "WRC Surface Ignition" scenario. Note the formation of the mostly orange/yellow flame on the WRC specimen at 24 s during this 0.16 g cm^{-2}, 1.4 m s^{-1} test.

3.2.2 Kaowool–Inert Substrate Tests

The “Firebrand Ignition on Kaowool” scenario was the only ignition scenario observed for the Kaowool tests. This was expected as the insulation board was selected for its strong inert properties and would not contribute to any thermal activity such as decomposition. The locations of these ignition events, with respect to the firebrand deposition area, were documented and consolidated to investigate common areas where a respective ignition scenario occurs. Figure 34 shows the locations of these ignitions for each set of testing conditions. The black lines represent the 50 cm^2 deposition area. There were no firebrand ignitions for the 0.16 g cm^{-2}, 0.9 m s^{-1} condition. Most of the ignitions occurred at the leading edge of the pile, which is expected as this is the first location where the continuous fresh oxidizer is driven into the glowing firebrand pile, generating the high peak temperatures in the back surface temperature profiles of the leading zone found in Section 3.1.2. Figure 35 shows the ignition probability considering a total of nine tests for each set of testing conditions, as well as the average time to ignition and burn duration of the “Firebrand Ignition on Kaowool” scenario, for the conditions where this ignition occurred.

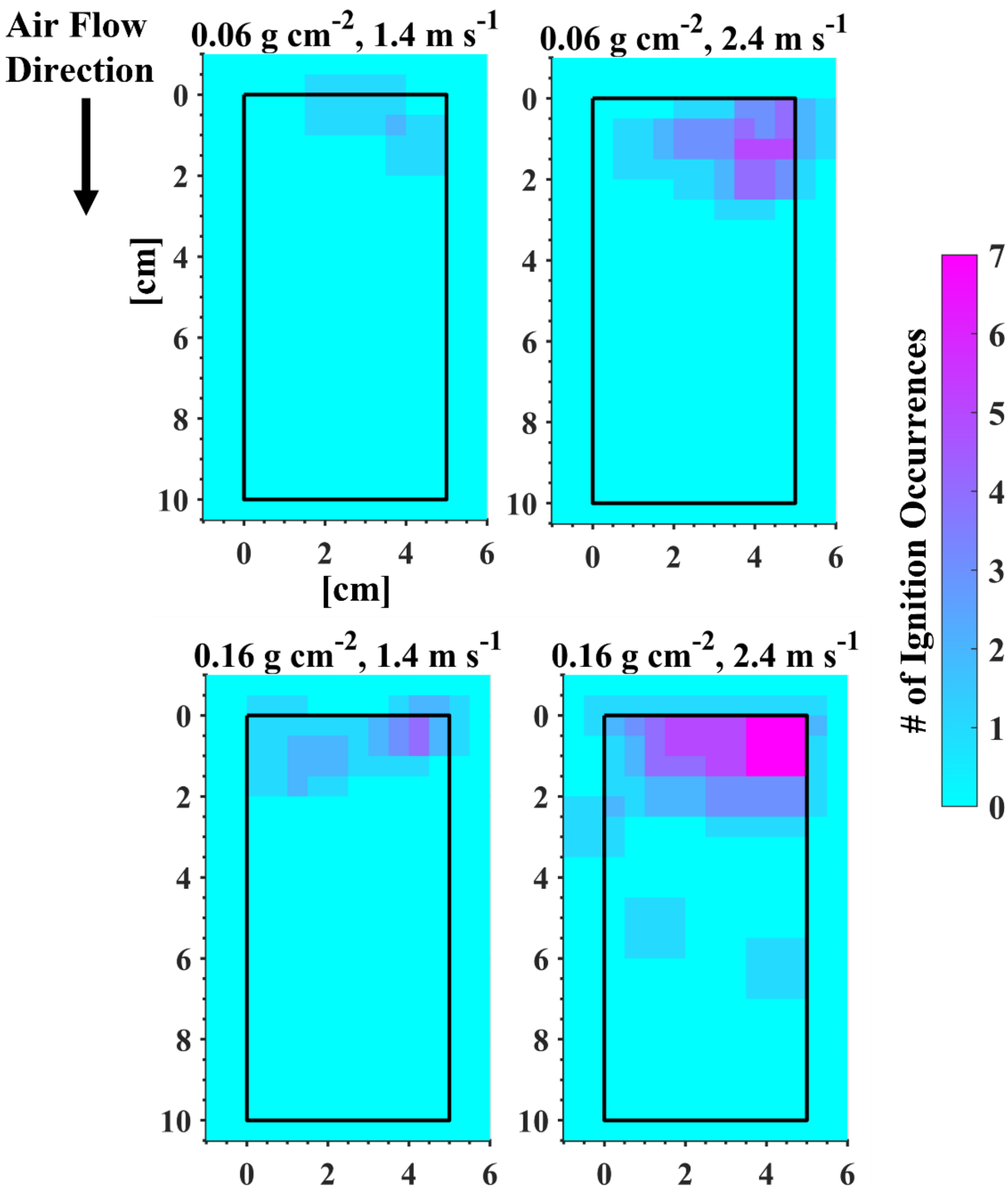

Figure 34: Locations of "Firebrand Ignition on Kaowool" scenario considering a total of nine tests for each of the respective testing conditions. The black lines represent the 50 cm^2 deposition area. There were no firebrand ignitions for the 0.16 g cm^{-2} coverage density, 0.9 m s^{-1} air flow velocity condition.

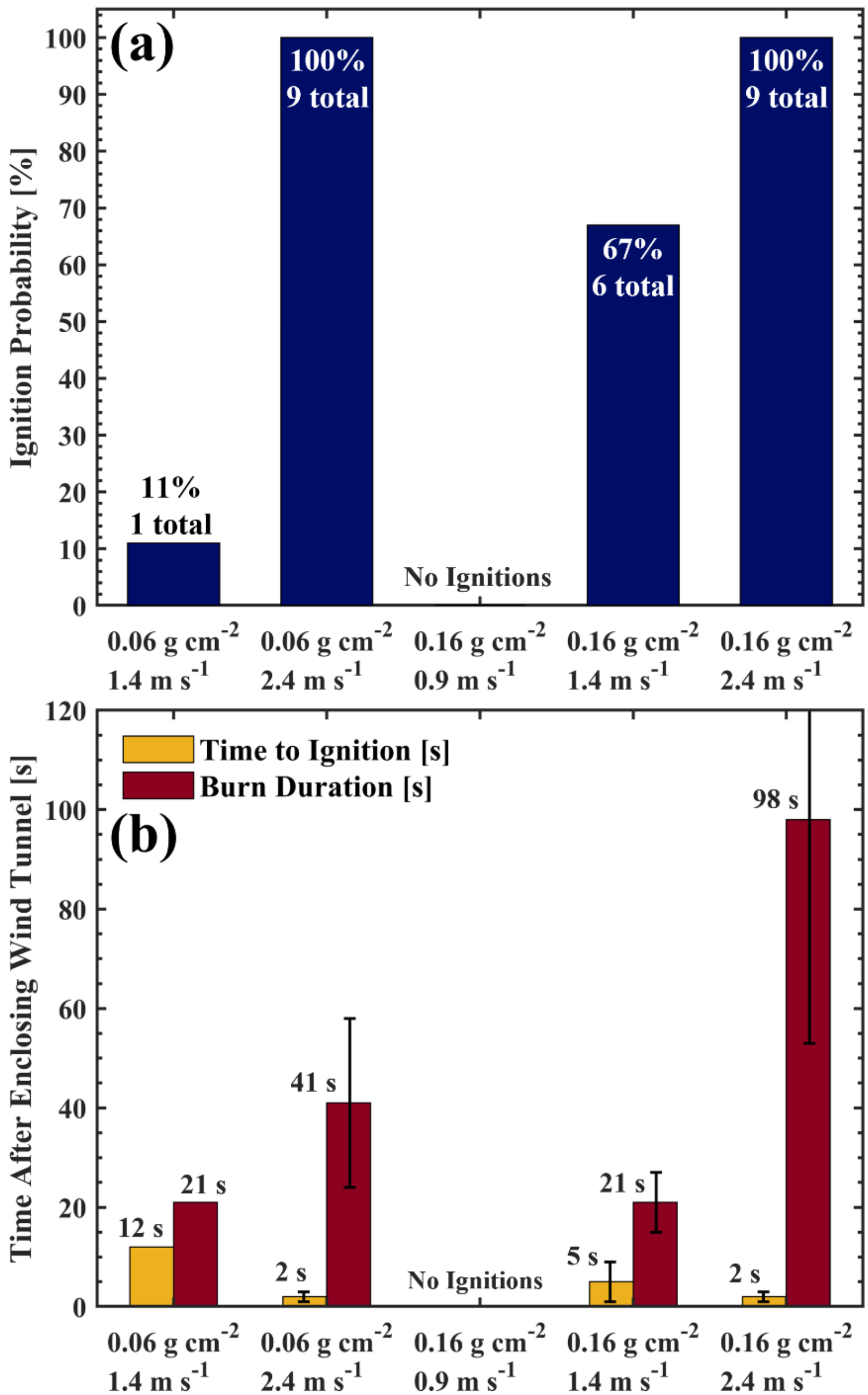

Figure 35: Ignition Probability (a), time to ignition and burn duration (b) for the "Firebrand Ignition on Kaowool" scenario considering a total of nine tests for each of the respective testing conditions.

The ignition probability was found to increase with an increase in both the air flow velocity and coverage density, however the increased air flow velocities had a more apparent effect, in that increasing the air flow velocity, by a factor of $^{12}/_{7}$, increased the ignition probability by 61 ± 56%; Whereas an increase in coverage density, by a factor of $^{8}/_{3}$, increased the probability by 56% at the 1.4 m s^{-1} air flow velocity, and no increase for the 2.4 m s^{-1}. This suggests that the air flow velocity is the primary driving force for ignition of these firebrands, and the coverage density is a secondary. Faster ignition times and longer burn durations were also found when the air flow velocity was increased for the two pile masses. An increase in air flow velocity results in an increased rate of fresh oxidizer being delivered to the smoldering firebrands. This could then increase the amount of heat generated in the pile, which increases the temperature of the firebrands, as seen in the leading zone peak temperatures in Section 3.1.2, thus presenting an increased chance of a hybrid–smoldering/flaming ignition of the firebrands and longer sustained flame burn duration. The burn duration also increased for the larger coverage density, at a respective air flow velocity. This is expected because as more firebrands are deposited, the longer gaseous pyrolyzates are produced in the region, allowing for longer sustained burning flames.

During all the Kaowool substrate tests, the smoldering front of the pile was found to shift from the leading edge to the middle of the deposition area as the test continued, also observed in Section 3.1. This is likely due to the increased decomposition rate of the firebrands from the increased temperatures seen in Section 3.1.2. Once the air flow velocity had forced enough of the firebrands at the leading edge to combust, more of the middle section of the pile was exposed to the wind tunnel air flow thus increasing the decomposition rate of the brands at the middle of the pile.

3.2.3 Western Red Cedar Substrate Tests

The WRC tests had both firebrand ignition, and surface ignition of the WRC board. The locations of these ignition events, with respect to the firebrand deposition area, were also documented and consolidated to investigate common areas where the respective ignition scenario occurs. Figure 36 shows the locations of the “Firebrand Ignition on WRC” scenario, defined as a flame originating on top of a firebrand or the pile. The black lines represent the 50 cm^2 deposition area. No firebrand ignitions occurred for the 0.06 g cm^{-2}, 1.4 m s^{-1} condition. Similar to the Kaowool tests, the firebrand ignitions occurred at the leading edge of the pile. Figure 37 shows the ignition probability, average time to ignition, and average burn duration of the “Firebrand Ignition on WRC” scenario.

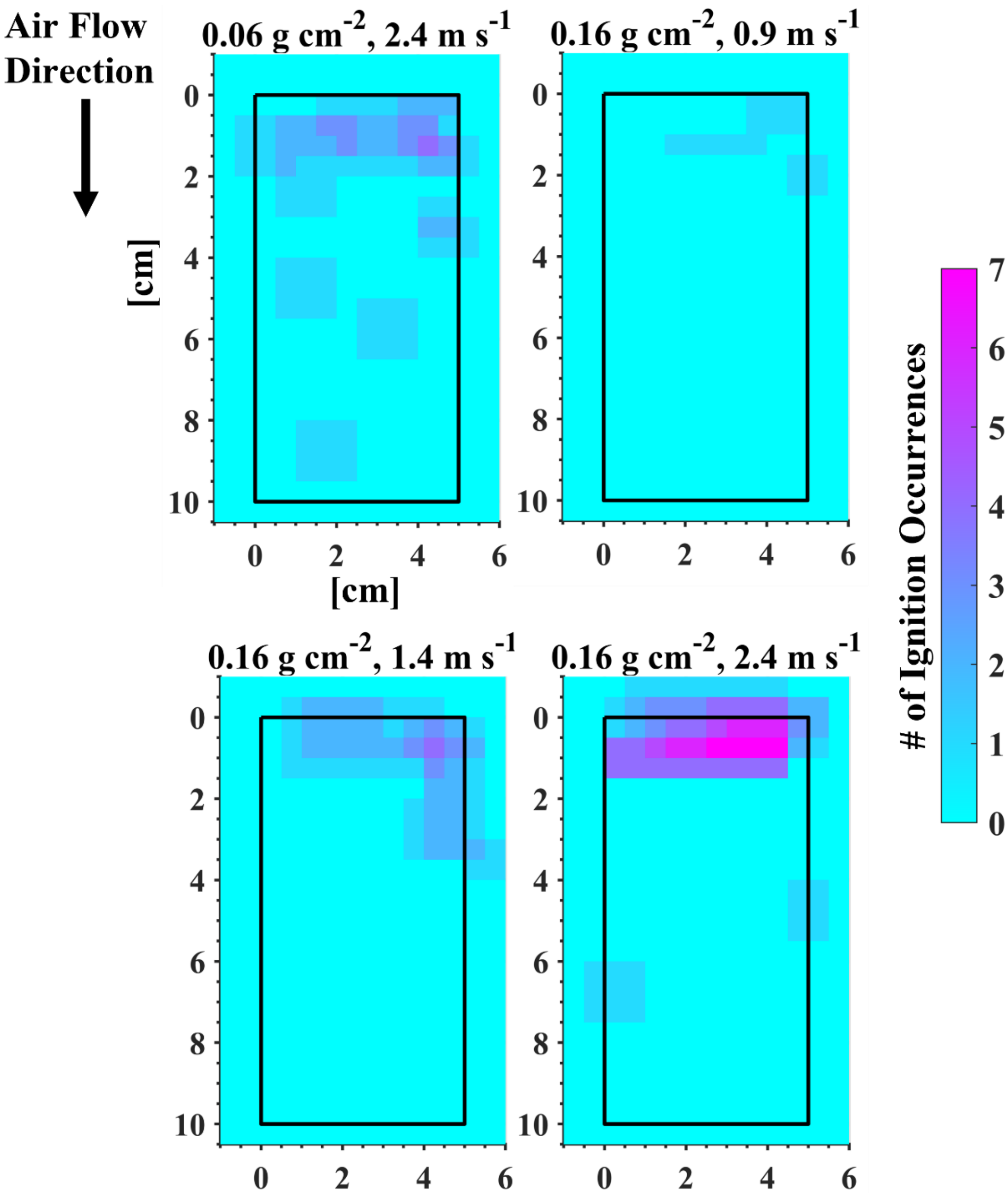

Figure 36: Locations of "Firebrand Ignition on WRC" scenario considering a total of nine tests for each respective testing condition. The black lines represent the 50 cm^2 deposition area. There were no firebrand ignitions that occurred for the 0.06 g cm^{-2} coverage density, 1.4 m s^{-1} air flow velocity condition.

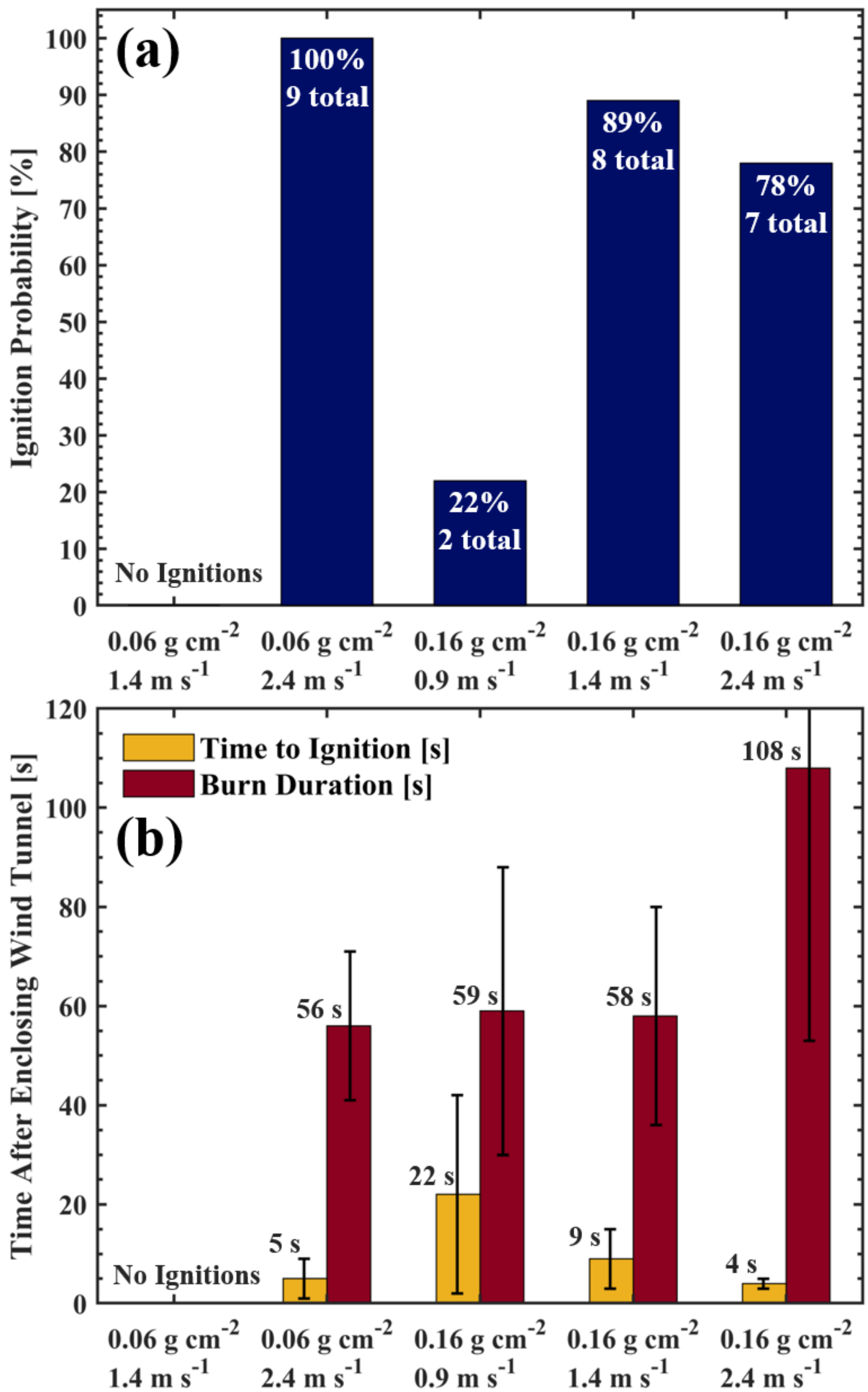

Figure 37: Ignition Probability (a), time to ignition and burn duration (b) for the "Firebrand Ignition on WRC" scenario considering a total of nine tests for each of the respective testing conditions.

Similar to the firebrand ignition during the Kaowool tests in Section 3.2.2, the ignition probability of firebrand ignition was found to increase by 100% with an increase in the air flow velocity by a factor of $^{12}/_{7}$ for the 0.06 g cm^{-2} coverage density, however decreased for the 0.16 g cm^{-2} coverage density. It was difficult to quantitatively compare the effects of both coverage density and air flow velocity on the ignition probability of these firebrands when deposited on the WRC, as there were no systematic trends found when analyzing the video recordings of this study. Despite this inability for a comparison of ignition probability, faster times to ignition and longer burn durations were found with an increase in air flow velocity when considering the 0.16 g cm^{-2} coverage density. Although trends in the ignition probability could not be identified, the air flow velocity could still be the primary driving force for the ignition of these firebrands, however more wind tunnel tests are likely required to uncover this conclusion.

Similar trends were found for the ignition of firebrands on both substrates, however the quantitative values varied across the testing material. Table 5 shows a comparison of the firebrand ignitions on the Kaowool substrate found in Section 3.2.2, and on the WRC substrate.

Table 5: Comparison of firebrand ignitions on Kaowool versus WRC substrates for all five testing conditions.

Testing Condition	Probability [%]		Time to Ignition [s]		Burn Duration [s]	
	Kaowool	WRC	Kaowool	WRC	Kaowool	WRC
0.06 g cm^{-2}, 1.4 m s^{-1}	11	0	12	No Ignitions	21	No Ignitions
0.06 g cm^{-2}, 2.4 m s^{-1}	100	100	2 ± 1	5 ± 4	41 ± 17	56 ± 15
0.16 g cm^{-2}, 0.9 m s^{-1}	0	22	No Ignitions	22 ± 20	No Ignitions	59 ± 29
0.16 g cm^{-2}, 1.4 m s^{-1}	67	89	5 ± 4	9 ± 6	21 ± 6	58 ± 22
0.16 g cm^{-2}, 2.4 m s^{-1}	100	78	2 ± 1	4 ± 1	98 ± 45	108 ± 55

From Table 5, there was no clear systematic change in ignition probability, and the firebrands took about 3 ± 1 seconds longer to ignite when deposited on the WRC specimen. This is likely due to the thicker WRC board having a thermal inertia about 4 times larger, and more significant conductive heat losses thus requiring more time to heat up (i.e., acted almost as a heat sink), as opposed to the thin inert Kaowool substrate. These longer ignition times of the firebrands deposited on the WRC, suggest that the initial smoldering of the pile is reduced. The firebrand piles also sustained the flames for about 30 seconds longer when the WRC specimen was present, which suggest that the WRC likely contributed gaseous fuel to this form of flaming combustion.

The "WRC Surface Ignition" scenario also frequently occurred near the leading edge of the pile, as shown in Figure 38. Most of these board ignitions occurred at the leading edge of the pile, however some ignitions did occur along the side of the pile during the 0.16 g cm^{-2}, 2.4 m s^{-1} test. These few instances were caused by firebrands falling off of the pile and igniting the substrate in the localized area. The ignition probability, average time to ignition, and average burn duration of the WRC Surface Ignition scenario under each condition can be found in Figure 39.

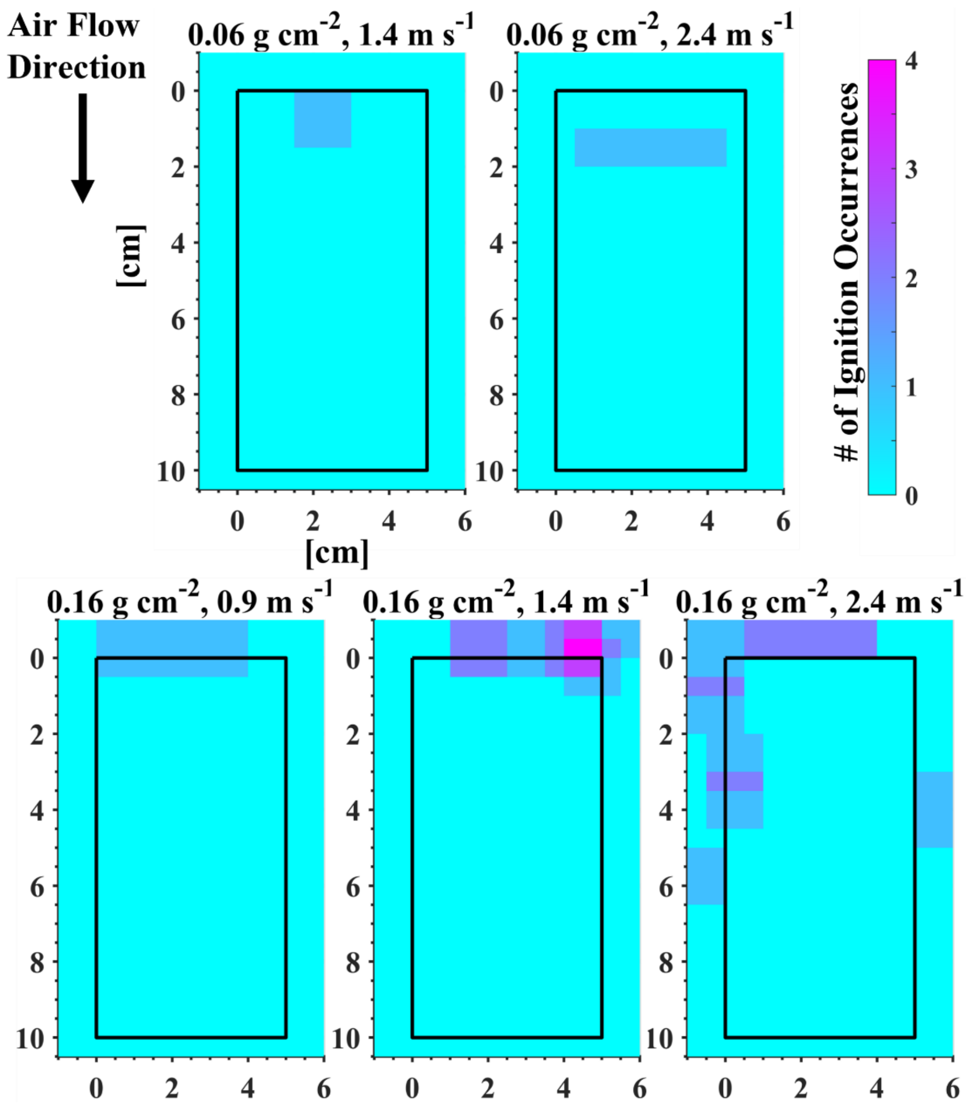

Figure 38: Locations of "WRC Surface Ignition" scenario considering a total of nine tests for each respective testing condition. The black lines outline the 50 cm^2 deposition area.

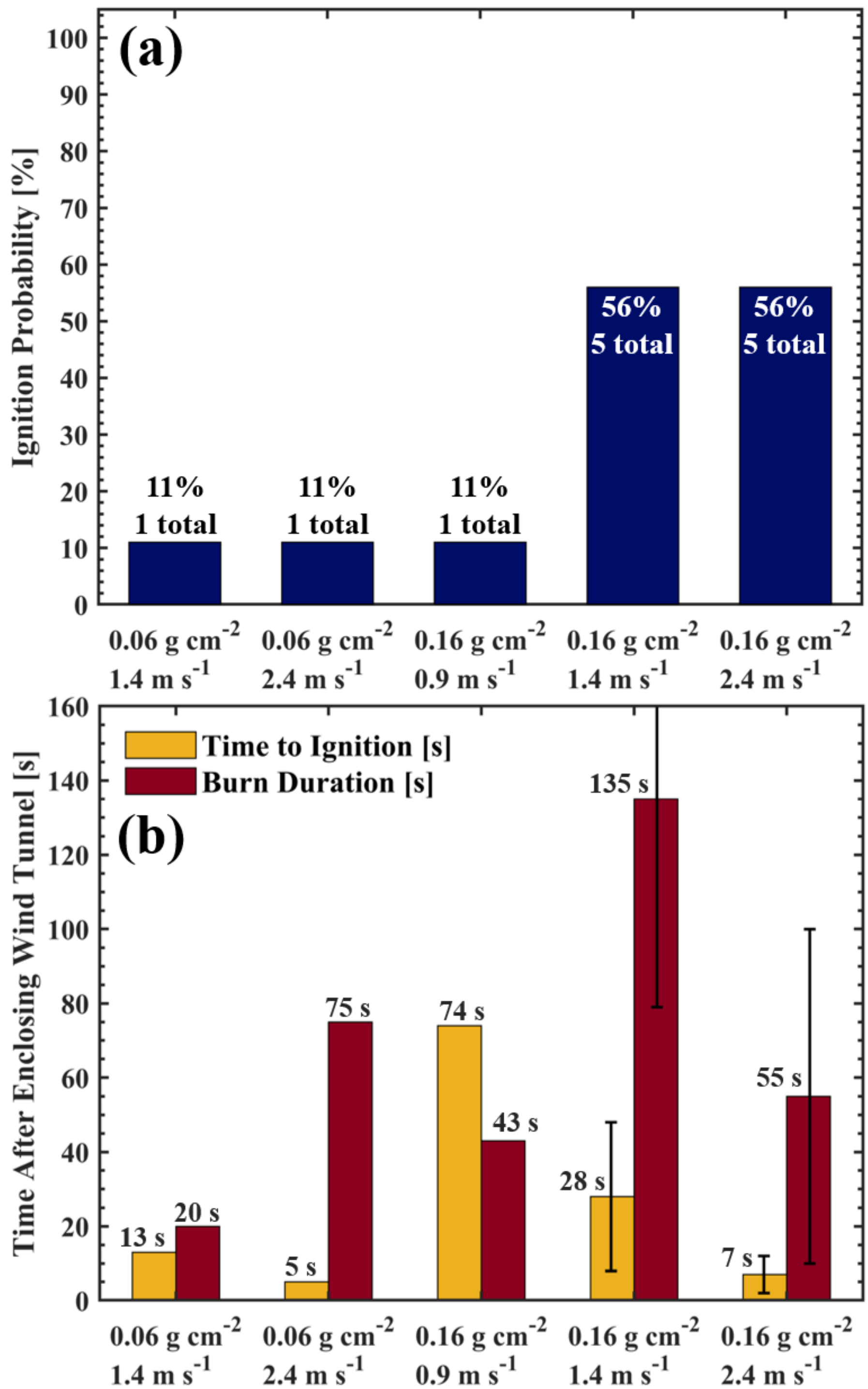

Figure 39: Ignition Probability (a), time to ignition and burn duration (b) for the "WRC Surface Ignition" scenario considering a total of nine tests for each of the respective testing conditions.

The ignition probability increased with an increase in coverage density and, excluding the 0.16 g cm^{-2}, 0.9 m s^{-1} condition, did not increase with an increase in air flow velocity. This is likely due to the overall larger heating rates of the WRC board associated with the larger coverage density found in Section 3.1.3. A faster heating rate of the WRC from the firebrand pile presents more thermal insult onto the combustible wooden specimen, which can increase the rate of gaseous pyrolyzate production and the probability of ignition. The ignition probabilities did not change when increasing air flow velocities for a given coverage density, excluding the 0.16 g cm^{-2}, 0.9 m s^{-1} condition. This 0.9 m s^{-1} air flow velocity was found to have the lowest back surface temperature profile average heating rates for both the leading and middle zones from Section 3.1.3. Therefore, this low air flow velocity may be insufficient to cause the increased heating rates noted from the two increased air flow velocities with the larger 0.16 g cm^{-2} coverage density. Faster ignition times were found with an increase in the air flow velocity. The 0.16 g cm^{-2}, 1.4 m s^{-1} condition revealed the longest burn duration, as well as having the highest ignition probability. The longer burn durations of the "WRC Surface Ignitions" allow for further flame spread across the substrate, which could increase the likelihood of siding and soffit materials of homes, described in Section 1.1.3, to ignite.

Given that both the "Firebrand Ignition on WRC" and "WRC Surface Ignitions" occurred during these WRC wind tunnel tests, a comparative analysis of these two ignitions scenarios may highlight if they are related to each other. Table 6 shows a comparison of flaming ignition statistics for the "Firebrand Ignition on WRC" and "WRC Surface Ignitions" for all five testing conditions.

Table 6: Comparison of ignition statistics for "Firebrand Ignition on WRC" and "WRC Surface Ignitions" for all five testing conditions.

Testing Condition	Probability [%]		Time to Ignition [s]		Burn Duration [s]	
	Firebrand	Surface	Firebrand	Surface	Firebrand	Surface
0.06 g cm^{-2}, 1.4 m s^{-1}	0	11	No Ignitions	13	No Ignitions	20
0.06 g cm^{-2}, 2.4 m s^{-1}	100	11	5 ± 4	5	56 ± 15	75
0.16 g cm^{-2}, 0.9 m s^{-1}	22	11	22 ± 20	74	59 ± 29	43
0.16 g cm^{-2}, 1.4 m s^{-1}	89	56	9 ± 6	28 ± 20	58 ± 22	135 ± 56
0.16 g cm^{-2}, 2.4 m s^{-1}	78	56	4 ± 1	7 ± 5	108 ± 55	55 ± 45

From Table 6, there was a systematic decrease in ignition probability and an increase in time to ignition for "WRC Surface Ignitions" compared to the "Firebrand Ignition on WRC." This is due to the glowing brands being at a higher temperature than the WRC when deposited, as well as having the most exposure to the air flow inside of the wind tunnel. Excluding the 0.06 g cm^{-2} coverage density 2.4 m s^{-1} air flow velocity condition, a higher surface ignition probability was paired with a higher firebrand ignition probability. Additionally, if the firebrands ignited faster, the WRC surface also took less time to ignite. Although it was difficult to visually identify with the DSLR video recordings if the flaming ignition of firebrands cause the WRC surface to ignite, this analysis of data presented in Table 6 suggests that the presence of a flaming firebrand acted almost as a pilot flame, aiding in the flaming ignition of the WRC board.

After the video analysis of all 45 WRC tests, the total consumption of the wooden specimen was qualitatively found to vary across testing conditions, shown in Figure 40. An increase in either the coverage density or air flow velocity increased the total consumption of the board. It was difficult to recognize, qualitatively, if one had more of an effect than the other, however the board was consumed the most during the 0.16 g cm^{-2} coverage density, 2.4 m s^{-1} air flow velocity tests.

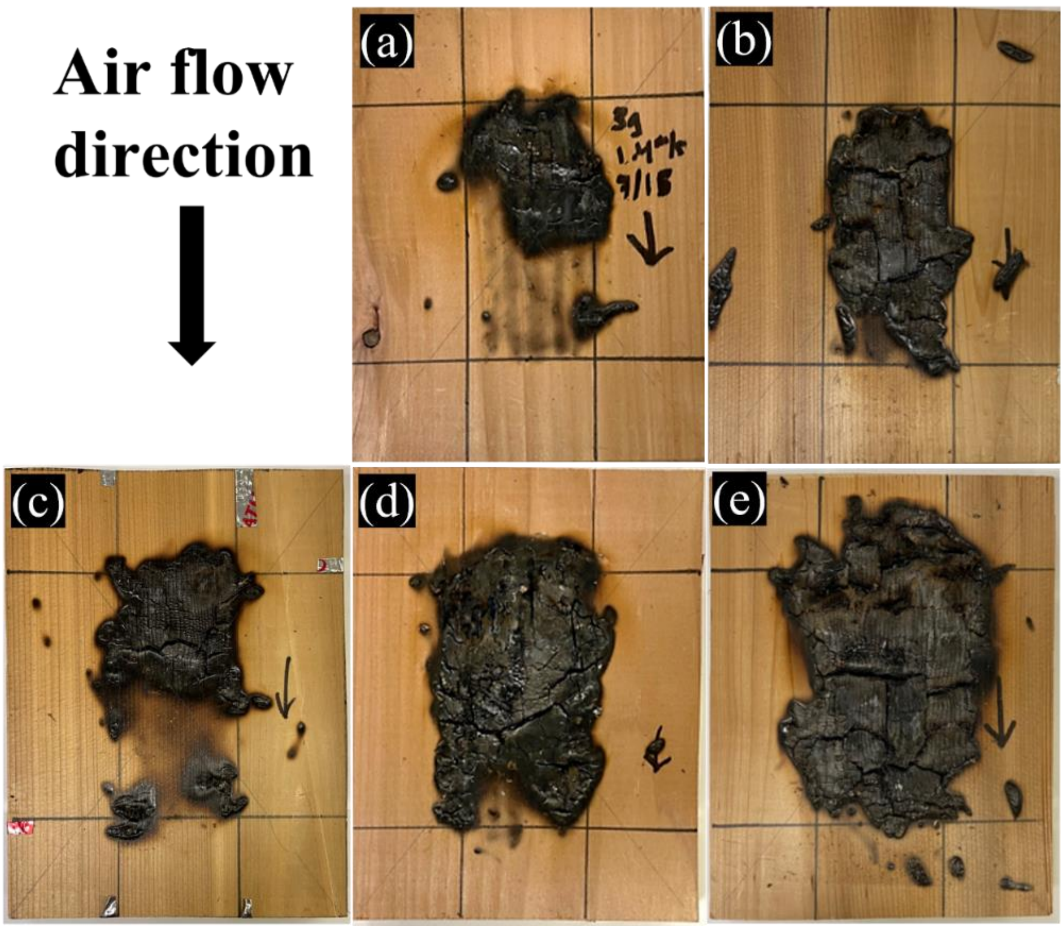

Figure 40: Representative WRC test specimens from (a) 1.4 m s^{-1} and (b) 2.4 m s^{-1} for the 0.06 g cm^{-2} coverage density and (c) 0.9 m s^{-1}, (d) 1.4 m s^{-1}, and (e) 2.4 m s^{-1} for the 0.16 g cm^{-2} coverage density, qualitatively illustrating effects of coverage density and air flow velocity on the total consumption of the wooden specimen.

3.3 Thermal Analysis of Common Flaming Ignition Zone

3.3.1 Analysis Procedures

From the flaming ignition study in Section 3.2, it was observed that most of the ignitions occurred 0.5 cm before the deposition area, and 1 cm into the pile at the leading edge. Since the leading zone, the zone first exposed by the wind tunnel air flow, began 0.5 cm after the leading edge of the 50 cm^2 deposition area, the back–surface temperature of this common ignition zone was not completely captured. Therefore, to better quantify the region where ignitions commonly occurred, a third zone, labeled as a “pre–leading” zone, was analyzed using the back–surface IR temperature measurements. This zone was also 4 cm along the width of the test specimens, however, was only 1.5 cm along the length of the specimen and was positions such that it covered both the 0.5 cm and 1 cm regions where ignitions were noted to frequently occur. Figure 41 shows a diagram of the back surface of a prepared specimen for these pre–leading tests. Note that a similar analysis to that shown in Figure 23 was conducted and found that 24 spot measurements accurately represented this zone.

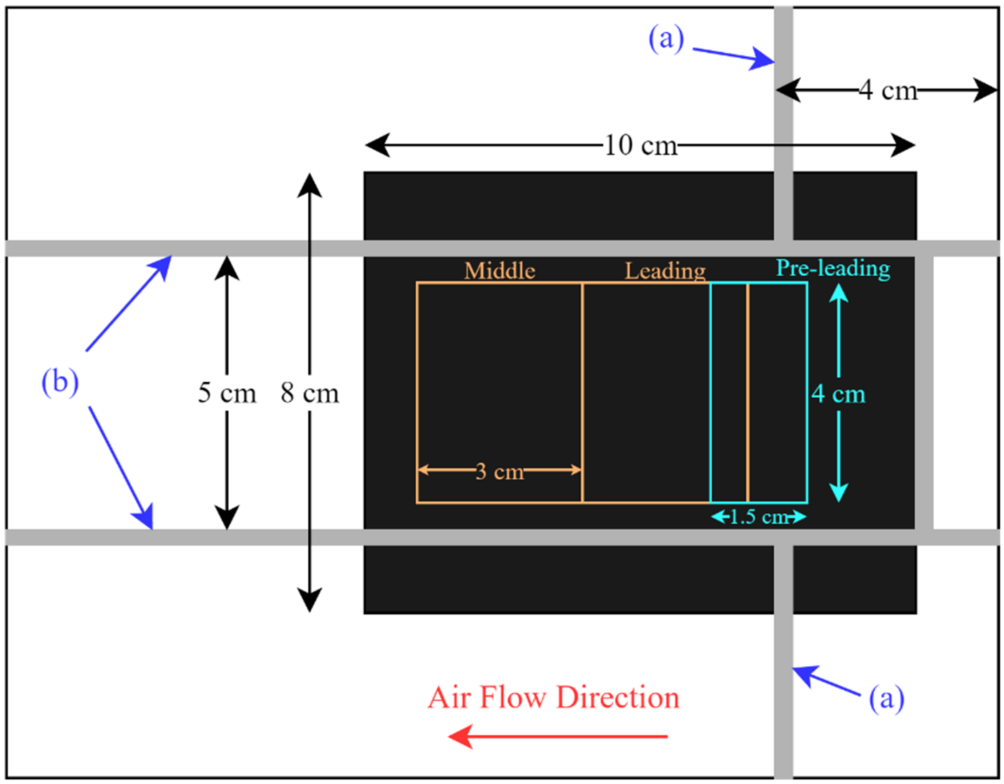

Figure 41: Diagram of prepared specimen for pre–leading zone tests. Aluminum foil tape outlining, leading edge (a) and sides (b) of 50 cm^2 deposition area. Note that the sampling area extends 0.5 cm past the leading edge of the deposition area (against the air flow).

Three tests were conducted for each of the five conditions on both the Kaowool and WRC substrates to quantify this "pre–leading" zone, note that these tests were used in the ignition study in Section 3.2 and gas analysis data was also collected during these tests. The temperature data from each individual test was binned every 12 seconds to smooth out the profiles. The average temperature profile for each set of conditions was taken as the average back surface temperature considering each individual back surface temperature profiles (i.e., three in total for each testing scenario). The variation for all average temperature profiles was calculated using Equation (3).

3.3.2 Kaowool–Inert Substrate Tests

Three tests were conducted at each of the five testing conditions on the Kaowool substrate. Figure 42 shows the average pre–leading zone back surface temperature profiles for the 0.06 g cm^{-2} coverage density at 1.4 and 2.4 m s^{-1} air flow velocities, Figure 43 for the 0.16 g cm^{-2}, 0.9 m s^{-1} condition, and Figure 44 for the 0.16 g cm^{-2} coverage density at an air flow velocity of 1.4 and 2.4 m s^{-1}. Note that each condition's average leading back surface temperature profile on the Kaowool substrate is plotted in gold to allow for a direct comparison of these two zones. A time of zero seconds is when the top piece of borosilicate glass was slid over the top opening, completely sealing the wind tunnel.

All five average pre–leading zone back surface temperature profiles rapidly increased to a peak value, and then quickly decreased after reaching this peak. The 0.06 g cm^{-2} coverage density tests decreased in temperature much quicker than that of its 0.16 g cm^{-2} counterpart. This is likely due to the decreased mass of glowing firebrands present in this pre–leading region (i.e., lower coverage density), which could cause the temperature to quickly decline as the brands oxidize.

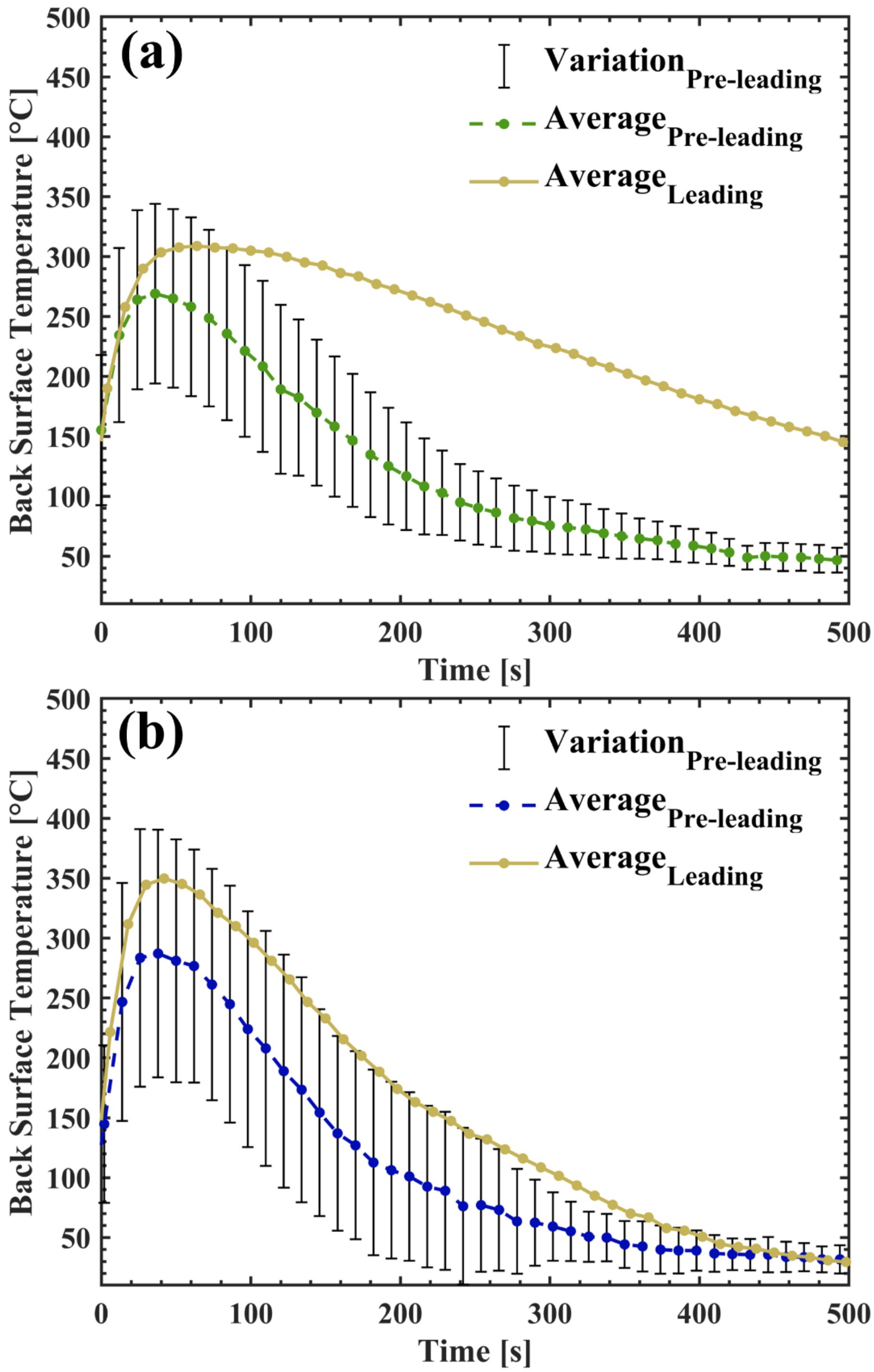

Figure 42: Average pre–leading zone temperature profiles, considering three tests, for the 0.06 g cm^{-2} coverage density at 1.4 m s^{-1} (a) and 2.4 m s^{-1} (b) air flow velocity on the Kaowool substrate. Each condition's average leading zone profile is plotted in gold.

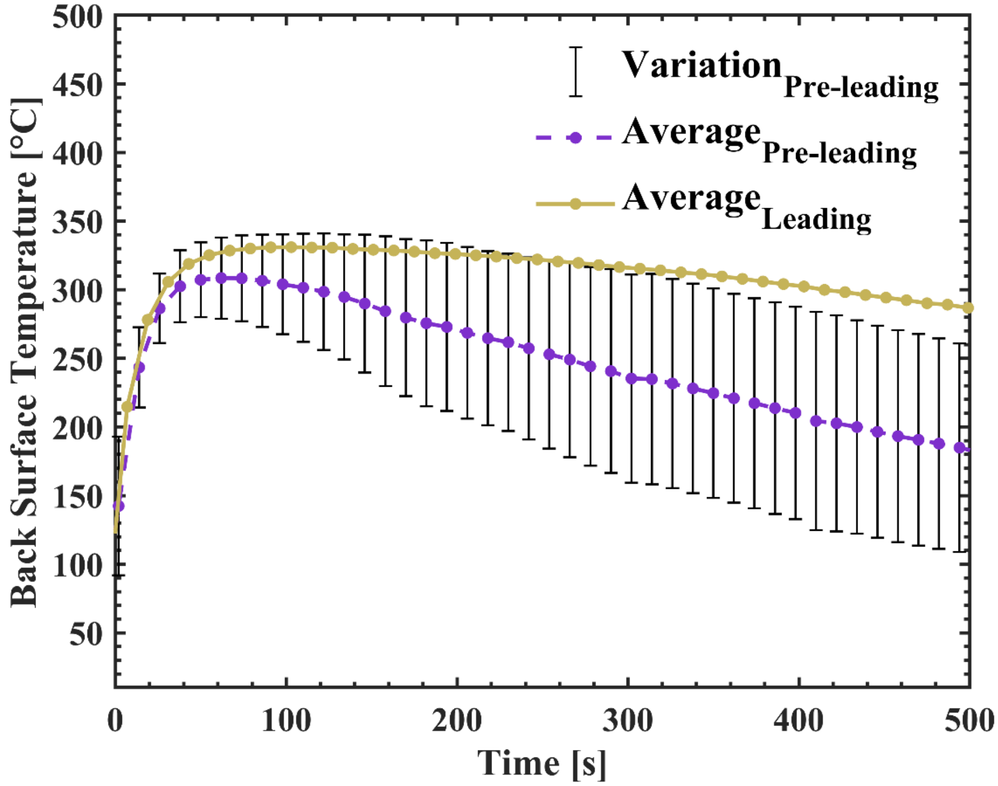

Figure 43: Average pre–leading zone temperature profile, considering three tests, for the 0.16 g cm^{-2} coverage density at the 0.9 m s^{-1} air flow velocity on the Kaowool substrate. The condition's average leading zone profile is plotted in gold.

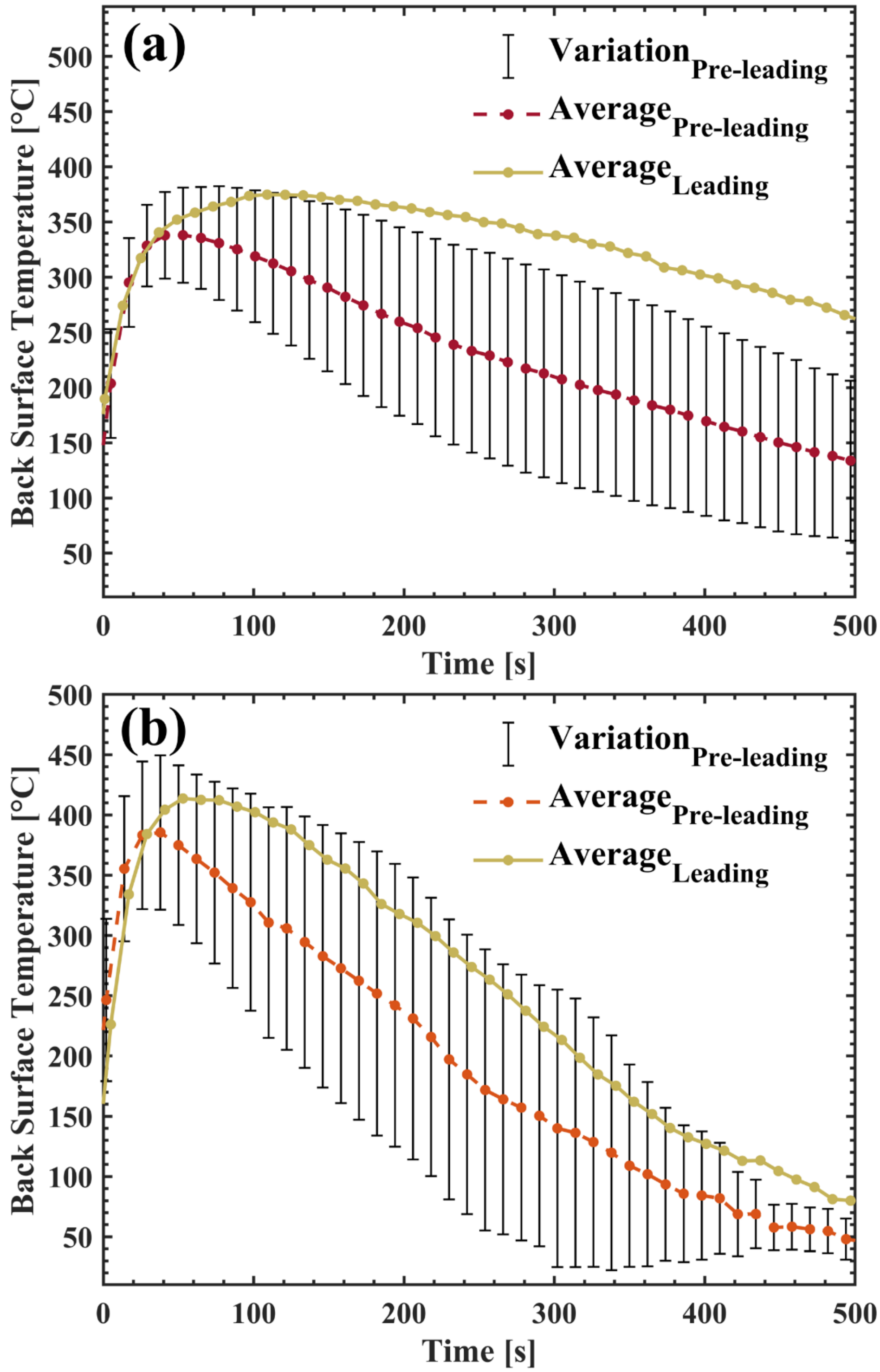

Figure 44: Average pre–leading zone temperature profiles, considering three tests, for the 0.16 g cm^{-2} coverage density at 1.4 m s^{-1} (a) and 2.4 m s^{-1} (b) air flow velocity on the Kaowool substrate. Each condition's average leading zone profile is plotted in gold.

Similar to Section 3.1.2, an average peak temperature was taken as the mean of all peak back surface temperatures across each individual test at that set of conditions. Table 7 provides the average peak back surface temperatures of the pre–leading and leading zones for all five conditions from the Kaowool substrate tests.

Table 7: Average peak back surface temperatures of pre–leading and leading zones from the Kaowool substrate tests for all five sets of conditions.

Testing Condition	Average Back Surface Peak Temperature [˚C]	
	Pre–leading	Leading
0.06 g cm^{-2}, 1.4 m s^{-1}	269 ± 25	309 ± 18
0.06 g cm^{-2}, 2.4 m s^{-1}	288 ± 52	353 ± 36
0.16 g cm^{-2}, 0.9 m s^{-1}	309 ± 4	332 ± 10
0.16 g cm^{-2}, 1.4 m s^{-1}	339 ± 12	378 ± 15
0.16 g cm^{-2}, 2.4 m s^{-1}	386 ± 20	417 ± 18

An increase in either the coverage density or air flow velocity increased the average back surface peak temperature of the pre–leading zone. Increasing the coverage density, by a factor of ⁸⁄₃, increased the average back surface temperature of the pre–leading zone by 84 ± 28 ˚C, whereas an increase in the air flow velocity by a factor of ¹²⁄₇, increased the peak temperature by 33 ± 28 ˚C. Although the coverage density seems to have the stronger influence, both the coverage density and air flow velocity affected the peak temperature of this region where ignitions commonly occurred. Also, the coverage density likely has the stronger effect because of the increased mass of firebrands falling off of the pile and into the 0.5 cm region, in the pre–leading zone, before the firebrand deposition area. The average peak back surface temperatures of the pre–leading zone across all five testing conditions' profiles were 40 ± 14 ˚C lower than the average peak temperatures of the leading zone from Section 3.1.2. This was interesting since this pre–leading zone is where the ignitions commonly occurred, however is likely due to the decreased mass of firebrands in this region compared to the region underneath the pile in the leading zone. Nonetheless, it is important to note that this common ignition zone experienced a different thermal environment than the leading and middle zones under the same testing conditions. Also, the pre–leading zone did have a similar dependence on both coverage density and air flow velocity as the leading and middle zones.

3.3.3 Western Red Cedar Substrate Tests

Three tests were conducted at each of the five testing conditions on the WRC substrate. Figure 45 shows the average pre–leading zone back surface temperature profiles for the 0.06 g cm^{-2} coverage density at 1.4 and 2.4 m s^{-1} air flow velocity, Figure 46 for the 0.16 g cm^{-2}, 0.9 m s^{-1} condition, and Figure 47 for the 0.16 g cm^{-2} coverage density at an air flow velocity of 1.4 and 2.4 m s^{-1}. Note that each condition's average leading back surface temperature profile on the WRC substrate is plotted in gold to allow for a direct comparison of these two zones. A time of zero seconds is when the top piece of borosilicate glass was slid over the top opening, completely sealing the wind tunnel.

All five average pre–leading zone back surface temperature profiles took about 100 – 200 seconds, similar to that of the leading zone in Section 3.1.3, before they began to gradually increase to a peak value. The peak temperatures of each condition's pre–leading zone back surface temperature was lower than the leading zone profile of that respective condition. This was also observed during the pre–leading zone Kaowool tests in Section 3.3.2, however the average heating rate would again better represent the conditions at the surface of the WRC board.

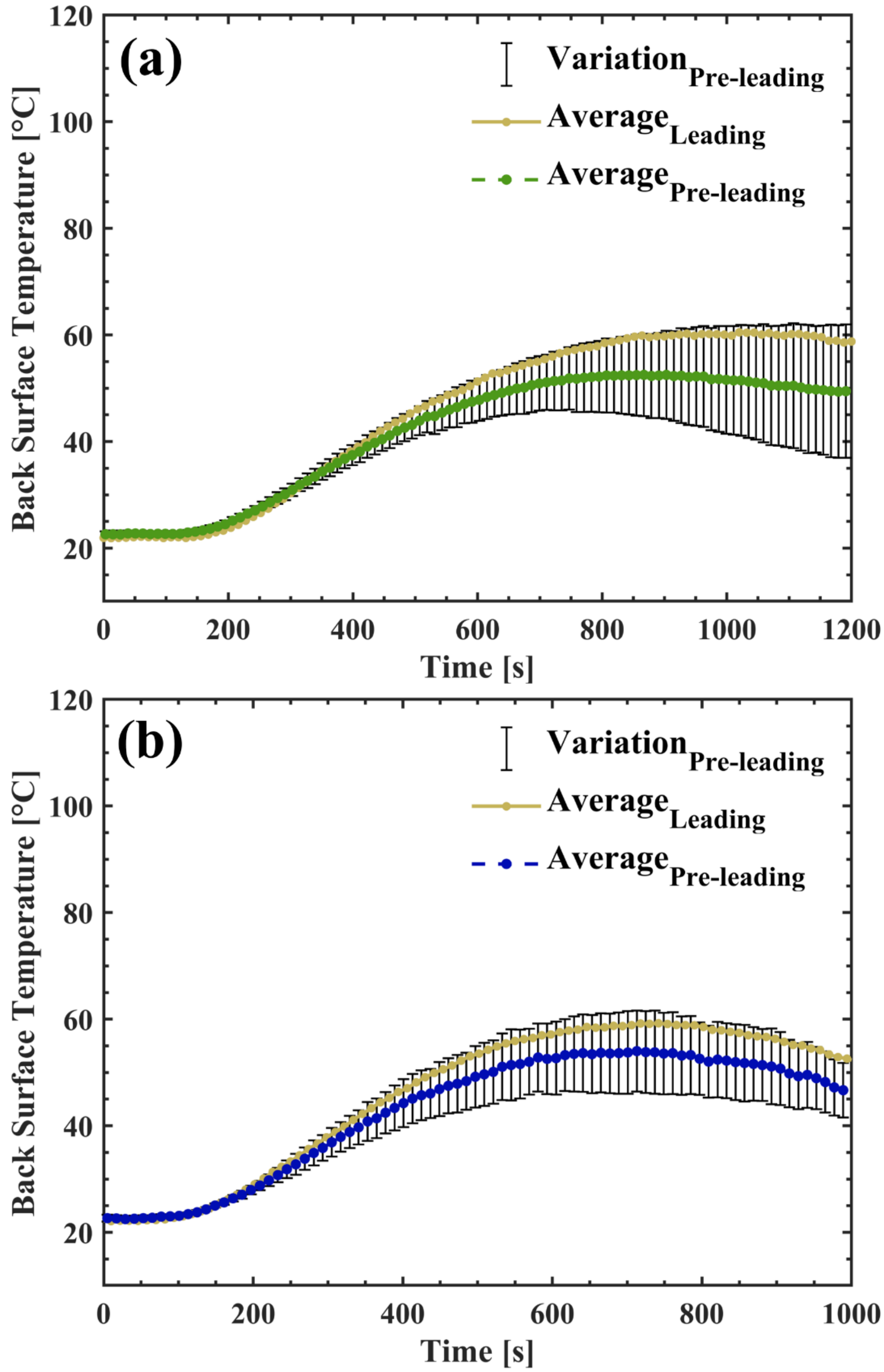

Figure 45: Average pre–leading zone temperature profiles, considering three tests, for the 0.06 g cm^{-2} coverage density at 1.4 m s^{-1} (a) and 2.4 m s^{-1} (b) air flow velocity on the WRC substrate. Each condition's average leading zone profile is plotted in gold.

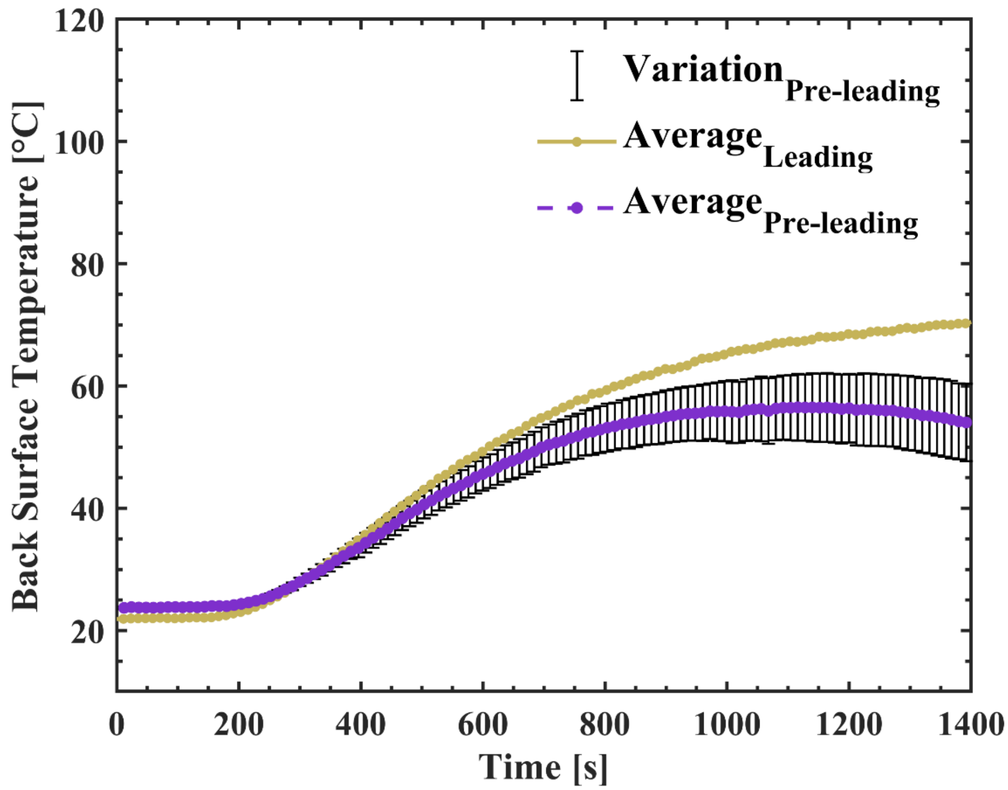

Figure 46: Average pre–leading zone temperature profile, considering three tests, for the 0.16 g cm^{-2} coverage density at 0.9 m s^{-1} air flow velocity on the WRC substrate. The condition's average leading zone profile is plotted in gold.

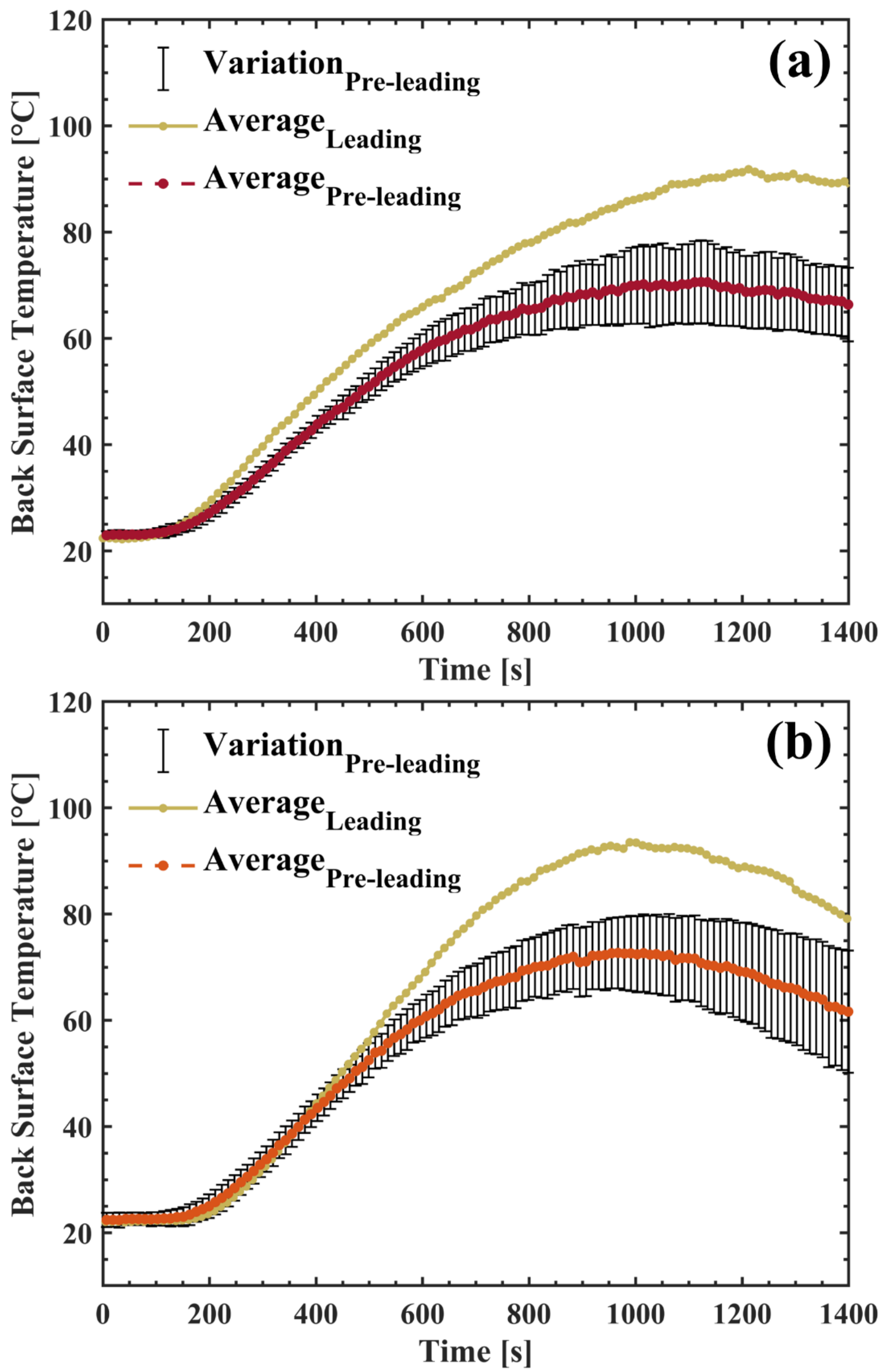

Figure 47: Average pre–leading zone temperature profiles, considering three tests, for the 0.16 g cm^{-2} coverage density at 1.4 m s^{-1} (a) and 2.4 m s^{-1} (b) air flow velocity on the WRC substrate. Each condition's average leading zone profile is plotted in gold.

As mentioned above, the average heating rate would better represent the conditions at the surface of the WRC board. This heating rate was calculated, the same as in Section 3.1.3, using the central difference theorem considering the temperature data starting when the respective average back surface temperature profile reaches 30 ˚C and 144 seconds after the temperature exceeded 30 ˚C. Table 8 provides the average heating rates of the pre–leading and leading zones for all five conditions on the WRC substrate.

Table 8: Average heating rates of the pre–leading and leading zones from the average back surface temperature profiles of WRC substrate tests for all five sets of conditions.

Testing Condition	Average Heating Rates [˚C s^{-1}]	
	Pre–leading	Leading
0.06 g cm^{-2}, 1.4 m s^{-1}	$(67 \pm 3) \times 10^{-3}$	$(81 \pm 3) \times 10^{-3}$
0.06 g cm^{-2}, 2.4 m s^{-1}	$(82 \pm 4) \times 10^{-3}$	$(92 \pm 3) \times 10^{-3}$
0.16 g cm^{-2}, 0.9 m s^{-1}	$(63 \pm 3) \times 10^{-3}$	$(76 \pm 2) \times 10^{-3}$
0.16 g cm^{-2}, 1.4 m s^{-1}	$(85 \pm 4) \times 10^{-3}$	$(103 \pm 6) \times 10^{-3}$
0.16 g cm^{-2}, 2.4 m s^{-1}	$(97 \pm 4) \times 10^{-3}$	$(120 \pm 5) \times 10^{-3}$

Similar to the average heating rates of the leading and middle zones found in Section 3.1.3, an increase in either the coverage density or air flow velocity increased the average heating rate of the pre–leading zone during the WRC substrate tests. Increasing the coverage density, by a factor of ⁸⁄₃, increased the heating rate by (17 ±

3) × 10^{-3} ˚C s^{-1}, whereas an increase in the air flow velocity, by a factor of 12⁄7, increased the heating rate by (14 ± 3) × 10^{-3} ˚C s^{-1}, again suggesting air flow velocity has the stronger influence. The difference in the effects of coverage density versus air flow velocity on the average heating rate in the pre–leading zone is similar to that found in the leading and middle zone heating rates in Section 3.1.3. The average heating rate of a pre–leading zone was (16 ± 4) × 10^{-3} ˚C s^{-1} lower than that respective condition's leading zone average heating rate. A similar difference was seen with the average peak temperatures of the leading versus pre–leading zones on the Kaowool substrate tests in Section 3.3.2. These lower heating rates are likely due to the decreased mass of firebrands in this pre–leading zone compared to the region underneath the pile in the leading zone.

Nonetheless, it is important to note that this common ignition zone experienced a different thermal insult from the firebrand pile than the leading and middle zones under the same testing conditions. Understanding these differences in heating rates of the WRC board from the firebrand pile between the pre–leading, leading, and middle zones would be crucial when using these heating rates for modeling purposes. If the large heating rate of the leading zone was used in a pyrolysis model to predict the behavior of the pre–leading or middle zones of the WRC specimen, the model might over predict the decomposition of the wooden specimen in these specific zones and would not accurately describe the physics present during such an event.

The slightly higher heating rates from the 0.16 g cm^{-2} coverage density, compared to the 0.06 g cm^{-2} coverage density, under the 1.4 and 2.4 m s^{-1} air flow velocities are indicative of the increased probability for this WRC specimen to ignite. Given an increase of the "WRC Surface Ignition" probability from 11% to 56% for the 0.06 to 0.16 g cm^{-2} coverage density increase, and no change from this 56% when increasing from 1.4 to 2.4 m s^{-1} under the 0.16 g cm^{-2} coverage density, found in Section 3.2.3, this $(85 \pm 4) \times 10^{-3}$ ˚C s^{-1} heating rate may be indicative of critical ignition conditions for WRC. Also, the peak back surface temperatures observed during the Kaowool substrate tests in Section 3.3.2 successfully differentiates the low and high probability ignition conditions (i.e., the testing conditions where the 11% "WRC Surface Ignition" probability was found had lower peak temperatures than the conditions with 56% probability). Note that these peak back surface temperatures from the Kaowool tests are not completely representative of the peak temperatures at the top surface where the brands are sitting but are adequate for a qualitative analysis with ignition probability of the WRC substrate.

Given the thickness of the WRC test specimens and the larger time scale of heat transfer through the board versus flaming ignition events, correlations between shape of these pre–leading zone temperature profiles and the formation of a flame on the surface of the specimen could not be made. The increased coverage density did have a higher "WRC Surface Ignition" probability, found in Section 3.2.3, and the heating rates of this pre–leading zone were higher with an increase in the coverage density. Despite this, it is difficult to correlate this larger heating rate to the presence of a flame, and not simply to the increased thermal mass of the larger firebrand coverage density.

3.4 Wind Tunnel Exhaust Flow Analysis

3.4.1 HRR and MCE Calculation Procedure

During the calibration of the NDIR gas analysis system in Section 2.3.2, the delay time of the system was measured to be 13 ± 1 s. To validate the accuracy of the CO/CO_2 voltage to vol.% calibrations preformed, a Bunsen burner controlled by an Alicat Scientific MC–10SLPM–D/5M mass flow controller, was inserted through the bottom of a Kaowool sample mounted in the wind tunnel. The wind tunnel was set to an air flow velocity of 1.4 m s^{-1} and once this wind velocity stabilized, recording on LabVIEW of the vol.% for CO and CO_2 began. Recording of the background CO and CO_2 concentrations continued for 30 seconds, and then a 1.5 LPM flow of methane (CH_4) gas was introduced into the Bunsen burner and ignited at the top. Once the burner was ignited, the wind tunnel was sealed, and the methane Bunsen burner was allowed to burn for 75 seconds. This process was repeated for a total of three methane flame validation tests. Note that the temperature in the room the day of these tests was 23 ˚C, and the RH was 46%. Although the moisture in the air is removed by the Drierite before entering the NDIR Gas Analyzer, this ambient water contributes to the velocity measurement made by the anemometer. This contribution however was within the uncertainty of the anemometer (± 5%) and thus the 1.4 m s^{-1} measurement was used.

An average vol.% value over the beginning 30 seconds was taken to represent ambient CO and CO_2 volume concentrations, $CO^{a}_{Vol.\%}$ and $CO_2{}^{a}_{Vol.\%}$, before the methane was introduced. Average exhaust vol.% values for CO and CO_2 were taken over the steady region representative of the presence of the methane flame within the tunnel $CO^{e}_{Vol.\%}$ and ${CO_2}^{e}_{Vol.\%}$. The difference between the ambient and steady methane flame values then gives the vol.% of CO and CO_2 produced from the steady burning of this methane flame. The average steady vol.% of CO_2 measured in the exhaust flow was 8% higher than the theoretical 0.068%–by volume value calculated considering complete–stoichiometric combustion of methane. Also, from these CO and CO_2 profiles, the response time of the NDIR Gas Analyzer, defined as the time for the respective profile to reach 63% of its peak value, was found to be 14 ± 2 s.

The average ambient and exhaust CO and CO_2 vol.% values from each respective validation tests were then used in Carbon Oxide Calorimetry [100] to measure the Heat Release Rate (HRR) of the methane flame. The expression for calculating HRR by Carbon Oxide Calorimetry can be found in Equation (6) [100]. The average uncertainty of this method, for methane, is about 30% [101].

$$HRR = E'\left(\dot{m}^{e}_{CO_2}\right) + E''\left(\dot{m}^{e}_{CO}\right) \tag{6}$$

where E' is the heat released per unit mass of CO_2 (13.3 kJ g^{-1} [102]), E'' is the heat released per unit mass of CO (11.1 kJ g^{-1} [102]), and $\dot{m}^{e}_{CO_2}$, $\dot{m}^{e}_{CO}$ are mass flow rates in the exhaust of CO_2 and CO produced from the combustion of methane, respectively. The NDIR Gas Analyzer measured the concentrations of CO and CO_2 on a volume basis, therefore Equation (7) and Equation (8) were used to calculate the CO_2 and CO mass production rates.

$$\dot{m}^{e}_{CO_2} = \rho_{CO_2}\, \dot{V}_e \left(\phi^{e}_{CO_2} - \phi^{a}_{CO_2}\right) \tag{7}$$

with ρ_{CO_2} being the gas density of CO_2 at 23 ˚C (1824 g m^{-3} [94]), $\dot{V}_e$ is the volumetric flow rate in the exhaust, taken as the cross–sectional area of the wind tunnel test section (0.26 m x 0.10 m) multiplied by the air flow velocity in the wind tunnel (1.4 m s^{-1}), and $\phi^e_{CO_2}$, $\phi^a_{CO_2}$ are the steady state exhaust and ambient volumetric fractions of CO_2, respectively.

$$\dot{m}^e_{CO} = \rho_{CO}\, \dot{V}_e\, (\phi^e_{CO} - \phi^a_{CO}) \tag{8}$$

with ρ_{CO} being the gas density of CO at 23 ˚C (1160 g m^{-3} [94]), $\dot{V}_e$ defined above, and ϕ^e_{CO} and ϕ^a_{CO} are the steady state exhaust and ambient volumetric fractions of CO, respectively.

From the three respective methane flame tests, the HRR measured by Carbon Oxide Calorimetry was estimated as 0.71 ± 0.03 kW. The HRR of the methane flame can also be estimated by Equation (9) [103],

$$HRR = \Delta h^{CH_4}_c\, \dot{m}_{CH_4} \tag{9}$$

where $\Delta h^{CH_4}_c$ is the heat of combustion of methane (55.60 ± 0.02 kJ g^{-1} [104]), and $\dot{m}_{CH_4}$ is the mass flow rate of methane into the Bunsen burner taken as (2.55 ± 0.15) × 10^{-5} m^3 s^{-1} (1.5 LPM) multiplied by the gas density of methane (660 g m^{-3} [94]). This method of calculating HRR yields a value of 0.92 ± 0.06 kW.

The heat of combustion method of calculating HRR uses thermochemistry to estimate the rate of energy released when a gram of fuel is burned. It has been noted that the Carbon Oxide Calorimetry method underpredicts the HRR for methane by about 30% [101]. Knowing this, with the 23% underprediction of the HRR by the NDIR Gas Analyzer using Carbon Oxide Calorimetry, and the 8% difference in theoretical to measured $CO_{2_{Vol.\%}}$ of this methane flame, this system accurately measures the vol.% of CO and CO_2 in the exhaust duct of the wind tunnel.

A Modified Combustion Efficiency (MCE) is widely used to characterize the smoldering and flaming combustion of a burning material [105 – 112] and is defined in Equation (10). This is calculated by measuring the excess mole fractions of CO_2 and CO within the smoke, χ_{CO_2} and χ_{CO}, respectively. Note that Δ symbolizes the subtraction of a baseline measurement of the CO_2 and CO mole fractions in the ambient environment prior to combustion. This MCE is used in unison with emission factor correlations, as well as to identify canopy fire activity in actual wildland fires [105].

$$MCE = \frac{\Delta\chi_{CO_2}}{\Delta\chi_{CO} + \Delta\chi_{CO_2}} \tag{10}$$

Previous lab studies have found an MCE of at least 0.90 for pure flaming combustion [106, 107], and a range of 0.65 – 0.80 for smoldering [107, 108]. Akagi *et al*. [108] suggested that smoldering is often near an MCE of 0.8, and a value of 0.9 suggests close to equal amounts of flaming and smoldering. Although the MCE gives some quantification to flaming/smoldering criteria, these values can be dependent on the fuel [105, 106]. Reviews have shown that the MCE is partially misunderstood and is highly sensitive to unknown field variables [110]. Hu *et al*. [111] found that the MCE fails to capture the transient combustion dynamics of smoldering peat fires; however, a later study by the same group [112] found that the transient MCE of peat fires was generally high for flaming, 0.91 – 0.98 which agrees with Stockwell *et al*. [107], while smoldering was 0.79 (dry, MC = 0 %) and 0.67 (MC = 25 %).

Despite the variability in the values indicative of smoldering and flaming combustion, the MCE from these methane tests can also be calculated using the $\left(\phi_{CO_2}^{e} - \phi_{CO_2}^{a}\right)$ and $(\phi_{CO}^{e} - \phi_{CO}^{a})$ values. Note that the MCE uses the molar fractions of CO and CO_2, χ_{CO} and χ_{CO_2}, however by assuming ideal exhaust gases, the volume fraction of a respective gas is equal to the molar fraction of that gas (i.e., $\phi_{CO_2} = \chi_{CO_2}$ and $\phi_{CO} = \chi_{CO}$). From the three respective methane flame tests, the MCE was estimated as 0.98, which strongly agrees with previous lab studies that have found an MCE ≅ 0.99 for pure flaming combustion [106, 107].

3.4.2 Kaowool–Inert Substrate Tests

The CO mass production rate from Equation (8), CO_2 mass production rate from Equation (7), HRR from Equation (6), and MCE from Equation (10) of the firebrands for each of the nine individual tests at all five testing conditions on the Kaowool substrate were calculated. This was done to investigate qualitative and possibly quantitative trends representative of smoldering and flaming combustion of these firebrand piles when exposed to the respective air flow velocities. After considering the profiles for CO and CO_2 mass production rate, HRR, and MCE from all individual tests, it was concluded that the flaming ignition of the firebrands could not be identified. The small blue flames noted on the surface of the firebrand pile during the “Firebrand Ignition on Kaowool” scenario from Section 3.2.2 do not produce enough CO_2 to stand out from the overall CO/CO_2 production of the entire smoldering pile. From this however, average profiles for CO/CO_2 mass production rates, HRR, and MCE across all nine individual tests, despite flaming ignition occurring or not, can be taken to represent the time evolution of the four quantities from a firebrand pile under the respective testing condition as each of these profiles were very reproducible.

The average profiles for each of these four quantities at each testing condition were taken as the averages between all nine respective profiles, after a 5 s moving average was applied to the individual test's profiles. Given that the NDIR analyzer response time is > 10 seconds, these moving averages could be used without significant loss of information on the trends of each profile. These average profiles represent the contribution of the pile where only the firebrands are smoldering/burning, when exposed to the predetermined air flow velocity. The variation was calculated using Equation (3). A time of zero seconds was defined as the time when the top piece of borosilicate glass was slid over the top opening, completely sealing the wind tunnel. Note that the HRR profiles were divided by the surface area of the specimen exposed to the firebrand pile (50 cm^2). Although the HRR in these systems likely do not scale linearly with the coverage area, normalizing HRR by the exposed surface area facilitates comparisons with burning intensities measured by standard flammability instruments such as the cone calorimeter [113].

The average profiles of CO mass production rate, and CO_2 mass production rate for the 0.16 g cm^{-2} coverage density at the 2.4 m s^{-1} air flow velocity considering nine tests on the Kaowool substrate can be found in Figure 48. The average HRR and MCE profiles for this same testing condition can be found in Figure 49. Similar plots for the other four conditions can be found in Figures C.1 – C.8 in Appendix C.

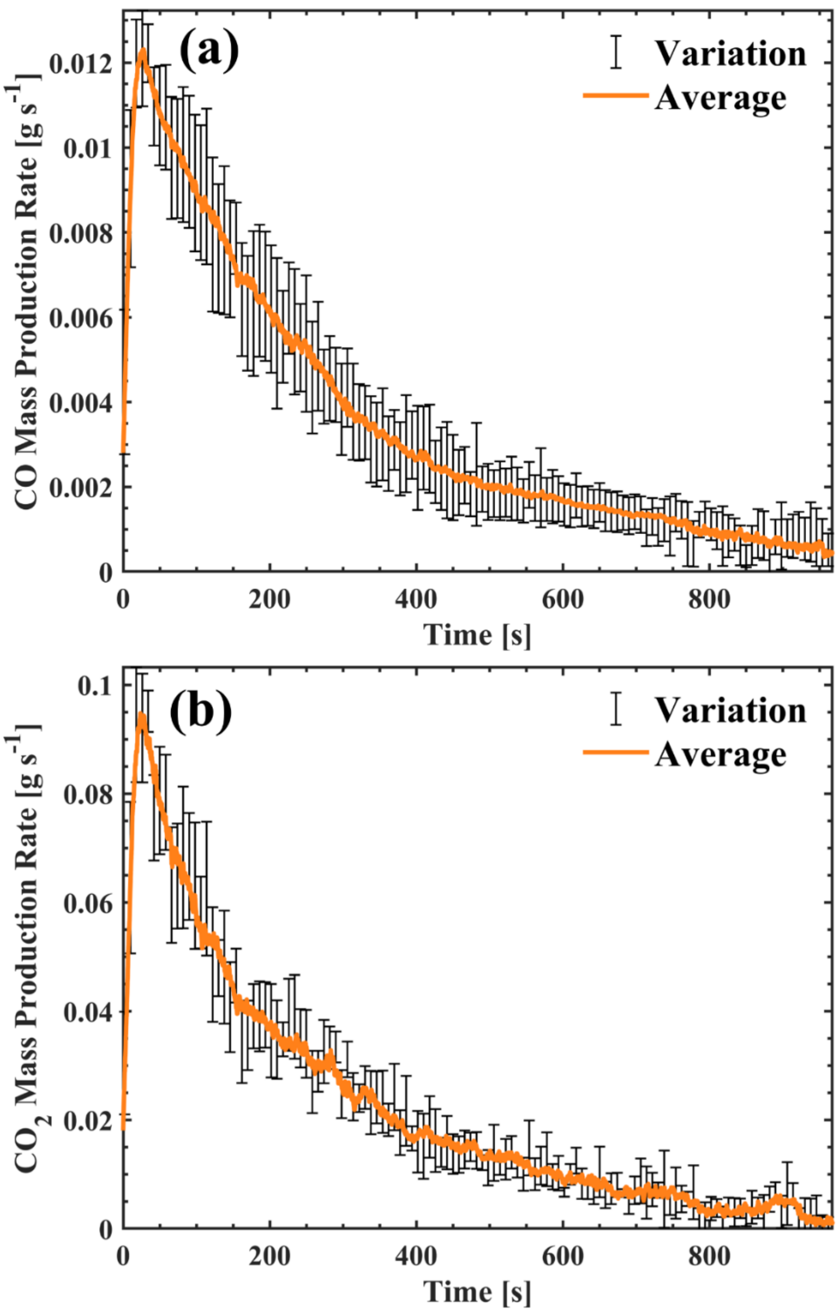

Figure 48: Average CO (a) and CO_2 (b) mass production rate profiles for the 0.16 g cm^{-2} coverage density, 2.4 m s^{-1} air flow velocity condition on the Kaowool substrate. These profiles consider nine tests.

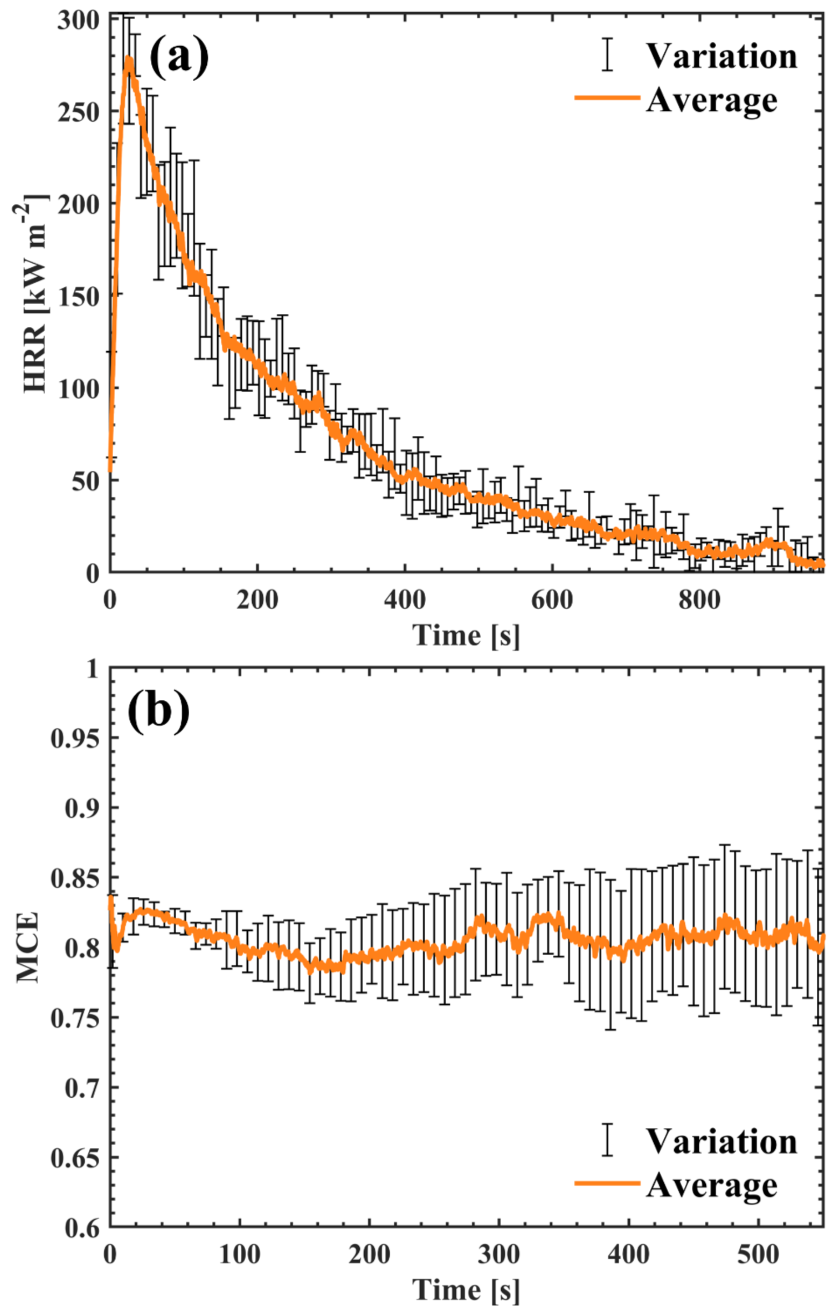

Figure 49: Average Heat Release Rate (a) and Modified Combustion Efficiency (b) profiles for the 0.16 g cm^{-2} coverage density, 2.4 m s^{-1} air flow velocity condition on the Kaowool substrate. These profiles consider nine tests.

For all average CO, CO_2, and HRR profiles across all five testing conditions, the respective profile rapidly increased to a peak value after the wind tunnel was completely sealed. Qualitatively, the dynamics of exposing the firebrands to the fresh oxidizer are captured in these drastically increasing profiles, followed by the decrease of these profiles shortly after the peak. It is worth noting that the variation for the MCE profiles during the higher air flow velocity profiles increased as the test progressed, which can be seen in Figure 49(b). This is likely due to the reduction in CO and CO2 voltage signals, and a corresponding decrease in the signal–to–noise ratio.

To quantitatively highlight the effects of coverage density and air flow velocity for the CO and CO_2 mass production rates, HRR, and MCE of these firebrand piles, an average value for each respective peak was obtained considering each of the nine individual CO, CO_2, and HRR profiles at that respective testing condition. Also, a single MCE value was calculated as the mean value from the average MCE profile for each respective testing condition. Note that the time ranges at which the MCE was plotted and subsequently averaged over varied across testing condition. The ranges were selected as they represented decomposition of the firebrands before the CO/CO_2 vol.% measurements become very low, which resulted in unrealistic–rapid changes in the MCE calculation (i.e., the MCE would randomly spike or drop, then continue back to the steady value). Table 9 gives the average peak CO, CO_2 mass production rates, average peak HRR, and mean MCE values for all five testing conditions during the Kaowool substrate tests.

Table 9: Average peak CO and CO_2 mass production rates, average peak HRR, and mean MCE values from the exhaust flow analysis during the Kaowool substrate tests for all five testing conditions.

Testing Condition	Average Peak CO Mass Production Rate [mg s^{-1}]	Average Peak CO_2 Mass Production Rate [mg s^{-1}]	Average Peak HRR [kW m^{-2}]	Mean MCE [–]
0.06 g cm^{-2}, 1.4 m s^{-1}	5 ± 1	48 ± 6	139 ± 14	0.82 ± 0.06
0.06 g cm^{-2}, 2.4 m s^{-1}	10 ± 1	62 ± 7	186 ± 20	0.77 ± 0.08
0.16 g cm^{-2}, 0.9 m s^{-1}	5 ± 1	43 ± 3	127 ± 9	0.84 ± 0.02
0.16 g cm^{-2}, 1.4 m s^{-1}	8 ± 1	60 ± 4	178 ± 13	0.83 ± 0.03
0.16 g cm^{-2}, 2.4 m s^{-1}	13 ± 1	102 ± 9	299 ± 25	0.81 ± 0.03

An increase in either the coverage density or air flow velocity increased both the peak CO and CO_2 mass production rates, which subsequently increased the average peak HRR. When increasing the coverage density, by a factor of ⁸⁄₃, at the same air flow velocity, the average peak CO and CO_2 production rates increased by 3 mg s^{-1} and 26 ± 14 mg s^{-1}, respectively. While an increase in air flow velocity, by a factor of ¹²⁄₇, at the same coverage density increased the peak CO and CO_2 production rates by 5 mg s^{-1} and 28 ± 14 mg s^{-1}, respectively. The air flow velocity has a stronger influence on the CO and CO_2 mass productions, as opposed to the coverage density. It is assumed that increasing the number of firebrands present in the wind tunnel would cause a large increase in CO and CO_2 mass production, however increasing air flow velocity has a much stronger effect. This is likely associated with the stronger influence air flow velocity has on the peak temperatures during the Kaowool substrate tests in Section 3.1.2 and 3.3.2 (i.e., all of the firebrands in the pile do not burn simultaneously, but are controlled by the amount of fresh oxidizer being delivered to the firebrand pile). This also explains the smoldering front of the pile shifting from the leading edge to the middle of the deposition area as the test continued, observed during the analysis of the DSLR video recordings in Section 3.2. From these observations, air flow velocity affected the rate of CO and CO_2 production more than the coverage density.

There was a 56% increase in firebrand ignition probability during the Kaowool substrate tests when the coverage density was increased from 0.06 to 0.16 g cm^{-2} for the 1.4 m s^{-1} air flow velocity, shown in Figure 35. There was also an increase in the average peak back surface temperature by 70 ˚C in the pre–leading zone where these firebrand ignitions commonly occurred when the coverage density was increased for this 1.4 m s^{-1} air velocity, seen in Section 3.3.2. Therefore, although the air flow velocity affected the peak CO and CO_2 mass production rates of the firebrand pile more than the coverage density, the brands are more likely to ignite due to the absolute increase in temperatures of the pile when more brands are deposited.

The mean MCE for the five testing conditions all stayed around a value of 0.81 ± 0.02. The MCE did seem to decrease slightly when air flow velocity was increased, which is indicative of increased smoldering of the brands occurring. This can be confirmed with the increased peak back surfaces temperatures in the middle zone of the deposition area in Section 3.1.2 knowing that no flaming combustion occurred late in the tests, and that an ash layer commonly formed over the pile late into the tests, shown in Figure 26. Note that this 0.81 value is on the upper end of the smoldering MCE ranges [107, 108], which suggests a hybrid–smoldering/flaming combustion mode. Therefore, from these observations, the deposition and subsequent combustion of glowing firebrand pile masses on an inert substrate in a flat–configuration consists of a hybrid–smoldering/flaming combustion and holds an MCE value of 0.81 ± 0.02, despite the mass of the firebrand pile or air flow velocity the pile is exposed to.

3.4.3 Western Red Cedar Substrate Tests

The CO mass production rate from Equation (8), CO_2 mass production rate from Equation (7), HRR from Equation (6), and MCE from Equation (10) of the firebrands for 37 total WRC substrate tests, between all five testing conditions, were calculated. The average CO and CO_2 mass production rate profiles from the Kaowool tests from Section 3.4.2 where only the firebrands were decomposing were subtracted from each individual WRC tests at that respective testing condition. This was done so that the contribution from only the WRC board to either flaming or smoldering combustion could be identified from each CO and CO_2 mass production rate and HRR profile. Note that doing so assumes that the pile behaves the same when deposited on either Kaowool or WRC. The MCE profiles were calculated based on the total CO and CO_2 production from firebrand and WRC because MCE is a global descriptor of the combustion process.

The average profiles for each of these four quantities at each testing condition were taken as the averages between all respective–individual profiles, after a 5 s moving average was applied to the individual test's profiles. Given that the NDIR analyzer response time is > 10 seconds, these moving averages could be used without significant loss of information on the trends of each profile. The variation was calculated using Equation (3). A time of zero seconds was defined as the time when the top piece of borosilicate glass was slid over the top opening, completely sealing the wind tunnel. Note that the HRR profiles were again normalized by the exposed surface area so comparisons with burning intensities measured by standard flammability instruments could be facilitated.

The average profiles of CO mass production rate, and CO_2 mass production rate of the WRC for the 0.16 g cm^{-2} coverage density at the 2.4 m s^{-1} air flow velocity considering seven tests can be found in Figure 50. The average HRR profile of the WRC and the MCE profile of the firebrand and WRC system, for this same testing condition, can be found in Figure 51. Note that the mean MCE of just firebrands from the Kaowool tests, found in Section 3.4.2, is plotted in gold. Similar plots for the other four conditions can be found in Figures D.1 – D.8 in Appendix D.

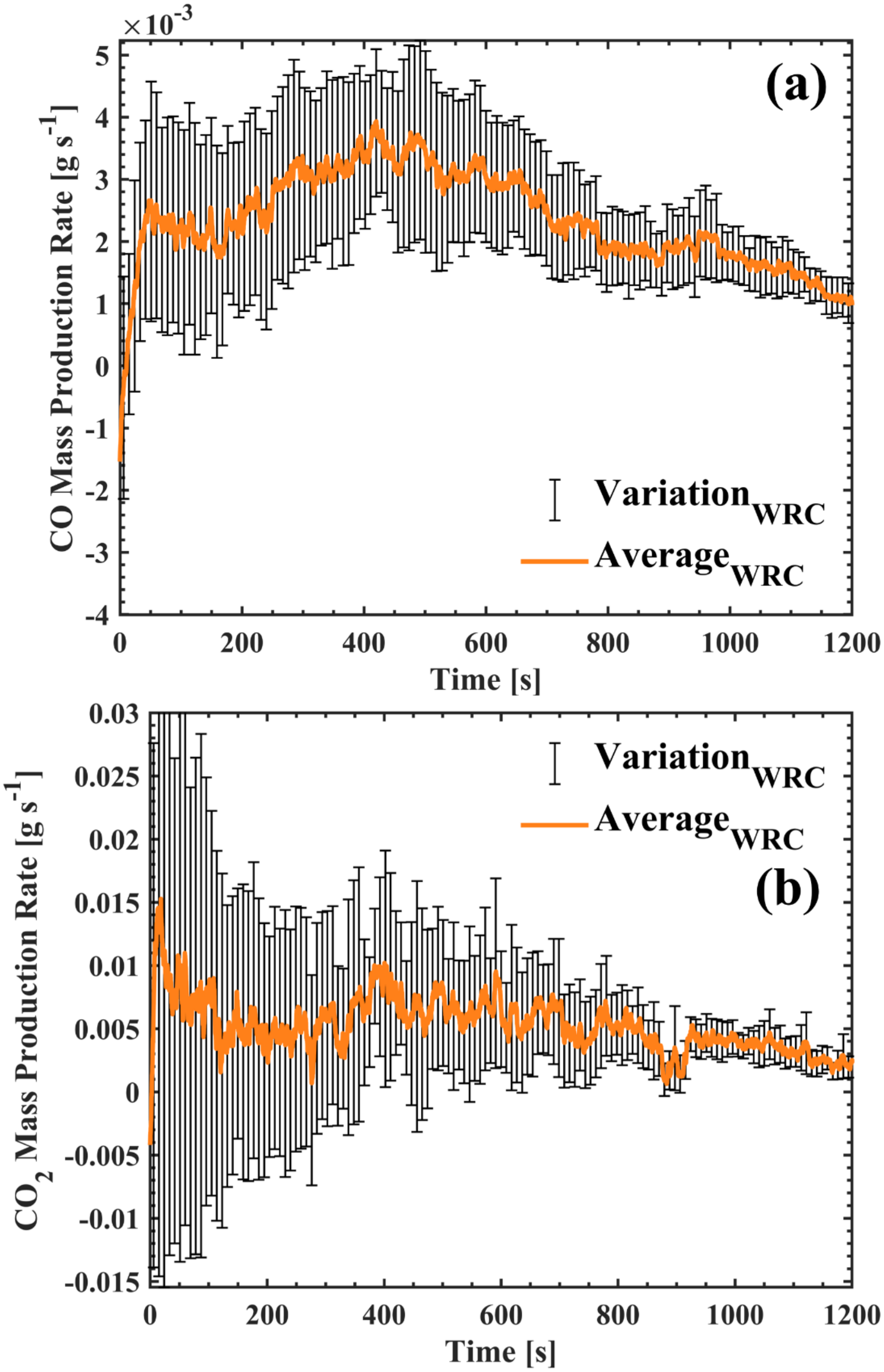

Figure 50: Average CO (a) and CO_2 (b) mass production rate profiles of the WRC substrate for the 0.16 g cm^{-2} coverage density, 2.4 m s^{-1} air flow velocity condition, considering seven tests.

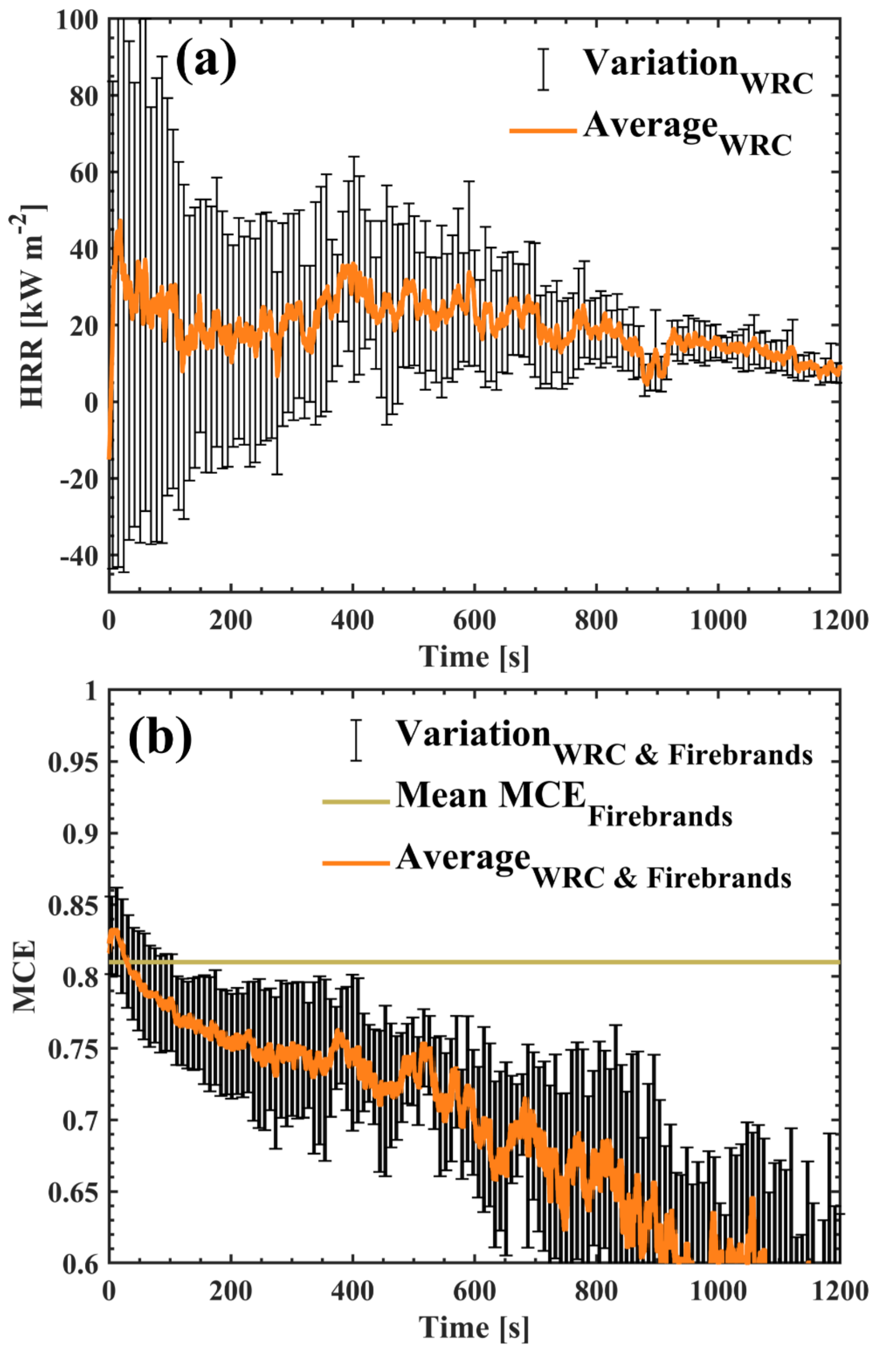

Figure 51: Average Heat Release Rate (a) of the WRC board, and Modified Combustion Efficiency (b) profiles for the 0.16 g cm^{-2} coverage density, 2.4 m s^{-1} air flow velocity condition, considering seven tests. Note the MCE is for contribution of both the firebrands and WRC, and the mean MCE of the firebrands from the Kaowool tests is plotted in gold.

The average CO, CO_2, and HRR profiles for both the 0.06 and 0.16 g cm^{-2} coverage densities at the 1.4 and 2.4 m s^{-1} air flow velocities started at negative values and increased to a value above zero. These three profiles for the 0.16 g cm^{-2}, 0.9 m s^{-1} condition also started at negative values and increased as the time progressed, however remained at values below zero. Given that these average CO, CO_2, and HRR profiles are of only WRC contribution (i.e., the average contribution from the pile was subtracted out), these initially negative profiles confirm that the initial smoldering of the firebrand pile is reduced with the presence of WRC. This was first suggested when comparing the firebrand ignitions on both substrates in Table 5. It was also qualitatively observed that the 2.4 m s^{-1} air flow velocity for both coverage densities increased at a faster rate than the respective density's 1.4 m s^{-1} air flow velocity. For all testing conditions except the 0.16 g cm^{-2} coverage density 1.4 m s^{-1} air flow velocity, the average MCE profiles started at values within 0.80 – 0.85, and then decreased below the respective testing condition's mean–firebrand MCE within the first 60 seconds after the wind tunnel was sealed. The 0.16 g cm^{-2} coverage density 1.4 m s^{-1} air flow velocity began at a value below the mean–firebrand MCE and remained below this mean MCE for the full duration of the tests. These five average MCE profiles dropping below the MCE value representative of the firebrand pile suggests that the FB–WRC system, on average under all testing conditions, initially contributes to heat production in a hybrid–smoldering/flaming state, however transitions into more intense smoldering as the test progresses. Note that a quantitative comparison of the effects of coverage density versus air flow velocity could not be made, as the shapes of each of the four quantities' average profiles varied across testing condition.

Since the average MCE profiles from the WRC tests decreased below the respective condition's mean–firebrand MCE within the first 60 seconds, and this time frame was when all of the "WRC Surface Ignition" events first initiated, observed in Section 3.2.3, a secondary analysis of the tests where the WRC board ignited was conducted to investigate possible identification of these ignitions. Figure 52 gives the HRR profiles for 10 of the 13 total tests where "WRC Surface Ignition" was observed. Note that three of these tests' gas analysis data could not be used as the zero and span calibrations were not correctly executed on the day these tests were conducted.

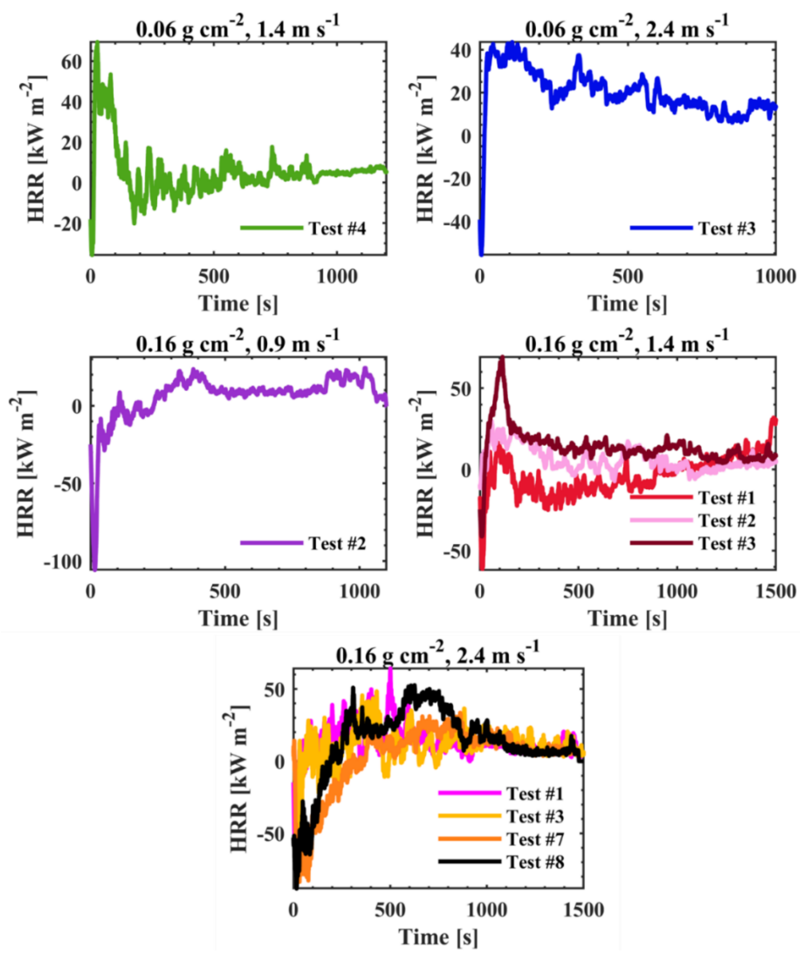

Figure 52: Individual Heat Release Rate profiles of WRC from 10 of the 13 total tests where "WRC Surface Ignition" was observed.

Each of the ten HRR profiles where the WRC board ignited began at values below zero and increased above zero has the test progressed. Therefore, from this observation, the possible identification of a WRC surface ignition event was defined using these HRR profiles that was generated considering only the CO and CO_2 mass production rates from the WRC board. The criterion that was used to possible identify the event indicative of surface ignition of the WRC board considered the HRR profile for a single test increasing above 0 kW m^{-2} within the first 60 seconds after the wind tunnel was sealed as depicted in Figure 53. Note again that the first 60 seconds was selected as this was the range when all the “WRC Surface Ignition” events occurred, as well as when the average MCE profiles from the WRC tests decreased below the respective condition’s mean–firebrand MCE.

Of these 10 tests, ignition on the surface of the WRC board was analytically confirmed by the HRR profiles for eight tests, 80%. The two tests where the “WRC Surface Ignition” event, identified visually, could not be identified analytically was caused by the firebrand pile from the Kaowool tests in Section 3.4.2 producing more CO and CO_2, when compared to these specific WRC tests. The thick WRC board absorbs more heat from the firebrands then the thin Kaowool insulation board, therefore the temperature of the brands is lower, thus the decomposition and subsequent production of CO and CO_2 of the firebrand pile is reduced when deposited on the WRC board. Therefore, the flames from these WRC board ignitions did not produce enough CO and CO_2 to be detected with this criterion (i.e., the flame from the WRC ignition was too small to overcome the signals from the Kaowool average profile for that testing condition).

The time to ignition was defined as the time when the HRR profile exceeded the 0–kW m^{-2} threshold. This method of estimating the ignition time was on average 18 ± 17 s different when compared to the times found in the visual analysis in Section 3.2.3. Note that this method both over and underpredicted the time to ignition. The variability in estimating the ignition time is due to the subjectivity in how the time when the wind tunnel was sealed was identified and set for each individual test. Figure 53 provides representative HRR profiles of tests where ignition was identified and time to ignition was estimated for the 0.06 and 0.16 g cm^{-2} coverage densities at both the 1.4 and 2.4 m s^{-1} air flow velocities. The one "WRC Surface Ignition" visually identified in Section 3.2.3 for the 0.16 g cm^{-2}, 0.9 m s^{-1} could not be analytically identified.

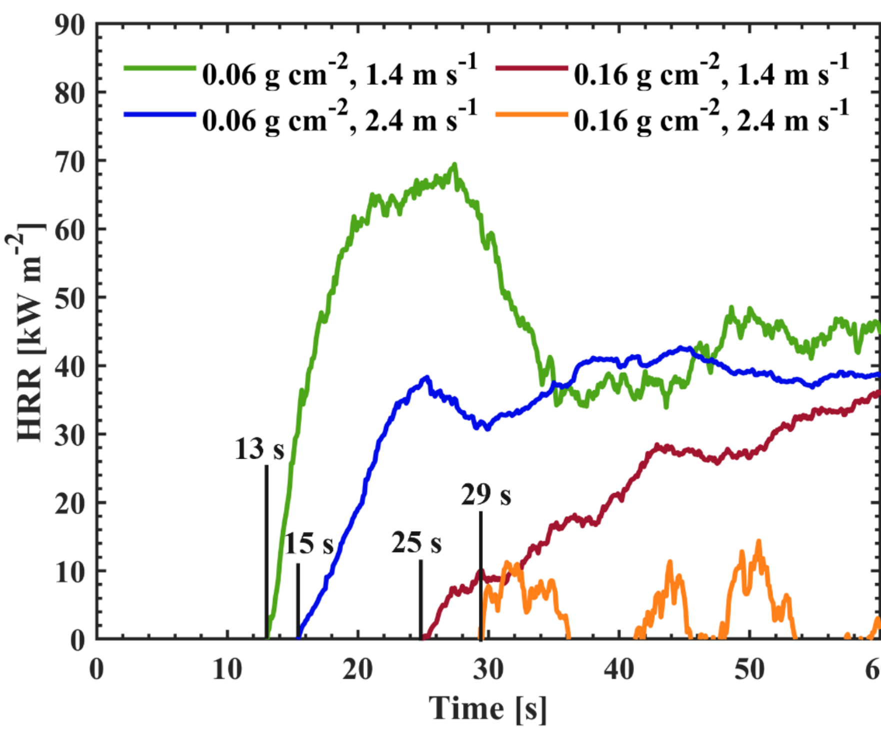

Figure 53: Heat Release Rate profiles from one test at each testing condition where "WRC Surface Ignition" was identified. Note the one 0.16 g cm^{-2}, 0.9 m s^{-1} ignition could not be analytically identified.

This ability to identify smoldering or flaming combustion of the WRC specimen, although not fully quantified here nor contains adequate accuracy when investigating flaming ignition, could serve as a pathway to quantitatively identify and characterize the flammability of common WUI decking materials when exposed to accumulated firebrand pile masses. Visual–qualitative analysis of the WRC specimens after each test found that the total consumption of the wooden specimen was found to vary across testing conditions, shown in Figure 40. Although this can be qualitatively observed, quantitatively describing the effects of coverage density and air flow velocity on the total consumption of the board by means of CO and CO_2 mass production rates or HRR would better represent the controlling factors for smoldering and flaming ignition of combustible materials used in the Wildland–Urban Interface.

Chapter 4: Conclusions

4.1 Summary

The Wildland–Urban Interface (WUI) is the zone of transition between developed community structures and undeveloped wildland areas including all the vegetative fuels found in these undeveloped areas [1]. Due to the close proximity of structures to the combustible–vegetative fuels, the building materials of these structures are susceptible to ignition during a WUI fire event. Specifically, the deposition of small pieces of smoldering or flaming embers generated from the burning of vegetative fuels or structures during fires, known as firebrands, onto combustible materials ahead of the fire front has been identified as being the prime means of fire spread during a wildland fire event [13 – 15, 25, 30 – 33]. Previous studies have investigated firebrands from actual wildland fires and have found that many are < 1 g, < 10 cm^2, and 1 – 3 cm in length [53]. This knowledge has then been used to create firebrands in a laboratory setting for small–scale studies on the thermal characterization of firebrands [43, 58 – 61]. As well as in firebrand accumulation studies that have found that when firebrands land on exterior decks, which have been found to be a common target fuel [4, 41 – 43] and major cause of property loss in the Waldo Canyon Fire [3, 13, 44], they can accumulate on top of the decking board surface, in–between the crevices of each board, within the gaps between a board and an exterior wall, and within a reentrant corner [63, 64].

To characterize the thermal behavior of accumulated firebrand piles of 0.06 and 0.16 g cm^{-2} coverage density and the flammability of a common WUI decking material, WRC, when exposed to these firebrand piles, a bench–scale wind tunnel was utilized. These firebrands were generated by burning 6.35 mm in diameter and 25.4 mm in length birch–wood cylindrical dowels, and were exposed to 0.9, 1.4, and 2.4 m s^{-1} air flow velocities after they were deposited on both non–combustible and combustible substrates. An infrared (IR) temperature measurement system was used to gather spatial and temporal back surface temperature profiles of the two substrates when exposed to the firebrand piles under the determined air flow velocities. The two substrates were a ⅛–inch (0.3175 cm) thickness Kaowool PM ceramic fiber board, and a western red cedar (WRC) board of ¾–inch (1.91 cm) thickness, selected for its low density. When considering the IR measurements, it was found that the leading edge of the firebrand pile, the edge first exposed to the flow of oxidizer into the tunnel, experienced the highest peak back surface temperatures and heating rates, compared to the region in the middle of the pile. The air flow velocity was found to have a stronger effect on the peak temperatures of the Kaowool specimen's back surface, and the heating rates of the WRC substrate when exposed to the firebrand piles, as opposed to the coverage density.

Video recording from two DSLR cameras was utilized to gather flaming ignition statistics like probability of ignition, time to ignition, and burn duration of the firebrand masses when deposited on both substrates. An increase in air flow velocity was found to be a primary driving force for the ignition of the firebrands when deposited on the Kaowool substrate, increasing the probability of ignition as well as yielding faster times to ignition and longer burn durations. This ignition probability of these firebrands when deposited on the Kaowool substrate, increased by 61 ± 56% when the air flow velocity was increased by a factor of $^{12}/_{7}$. Whereas an increase in coverage density, by a factor of $^{8}/_{3}$, increased the probability by 56% at the 1.4 m s^{-1} air flow velocity, and no increase for the 2.4 m s^{-1}. A systematic trend for ignition probability of these firebrands when deposited on the WRC specimen could not be found when analyzing the video recordings of this study. Despite this inability for a comparison of ignition probability, faster times to ignition and longer burn durations were found with an increase in air flow velocity when considering the 0.16 g cm^{-2} coverage density. Although trends in the ignition probability could not be identified, the air flow velocity is likely the primary driving force for the ignition of these firebrands, however more wind tunnel tests are required to uncover this conclusion.

The coverage density was found to be the primary driving force for ignition on the surface of the WRC board, increasing the ignition probability from 11% to 56% when coverage density was again increased by $^{8}/_{3}$. While there was no increase in probability when air flow velocity was increased. The pile of firebrands with a 0.16 g cm^{-2} coverage density exposed to an air flow velocity of 1.4 m s^{-1} revealed the longest burn duration, as well as having the increased ignition probability. The longer burn durations increase the propensity of flames spreading along the length of the WRC board which could pose a higher fire risk by increasing the likelihood of siding and soffit materials of homes to ignite.

The video recordings found that most ignitions occurred 0.5 cm before the deposition area, and 1 cm into the pile at the leading edge. Since this common ignition zone was not captured with the first two, a third zone, labeled as a “pre–leading” zone, was investigated using the back surface IR temperature measurement technique. This secondary experimental investigation found that coverage density controls the peak temperatures from the exposure of the firebrand piles, however the air flow velocity had a more apparent effect on the heating rates of the WRC specimens in this this common ignition zone. Slightly higher heating rates from the 0.16 g cm^{-2} coverage density under the 1.4 and 2.4 m s^{-1} air flow velocities were found, compared to the 0.06 g cm^{-2} coverage density at both velocities, and are indicative of the increased probability for this WRC specimen to ignite. Also, the peak back surface temperatures observed during the Kaowool substrate tests successfully differentiates the low and high probability ignition conditions (i.e., the testing conditions where the 11% of “WRC Surface Ignition” probability was found had lower peak temperatures than the conditions with 56% probability). However, it should be noted that these peak back surface temperatures from the Kaowool tests are not completely representative of the peak temperatures at the top surface where the brands are sitting but are adequate for a qualitative analysis with ignition probability of the WRC substrate.

The exhaust flow of the wind tunnel during all 90 tests was sampled and analyzed with a CAI ZPA Non–Dispersive Infrared (NDIR) Gas Analyzer. Carbon monoxide (CO) and Carbon Dioxide (CO_2) vol.% were measured with this analyzer and were used in Carbon Oxide Calorimetry to generate HRR profiles from both the firebrand pile during the Kaowool tests, and the WRC board. Profiles for the MCE, which is widely used to characterize the smoldering and flaming combustion of burning materials, were also generated for all tests.

Average profiles of CO mass production rate, and CO_2 mass production rate, HRR, and MCE for all testing conditions were generated from the Kaowool tests, which represent the contribution of the pile where only the firebrands are decomposing. When increasing the coverage density, by a factor of $^{8}/_{3}$, at the same air flow velocity, the average peak CO and CO_2 production rates increased by 3 mg s^{-1} and 26 ± 14 mg s^{-1}, respectively. While an increase in air flow velocity, by a factor of $^{12}/_{7}$, at the same coverage density increased the peak CO and CO_2 production rates by 5 mg s^{-1} and 28 ± 14 mg s^{-1}, respectively. From this comparison, the air flow velocity was found to have the stronger influence on the CO and CO_2 mass productions, as opposed to the coverage density.

The average CO and CO_2 production rate profiles from the Kaowool tests were used to subtract out the average contributions of CO and CO_2 from the firebrand pile during the WRC tests, to investigate only the contributions of the WRC board. On average, the WRC board was found contribute to either flaming or smoldering combustion when exposed to both firebrand piles in a 1.4 and 2.4 m s^{-1} air flow velocity environment. These observations were established if the average HRR profiles of the WRC increased from their initial values, illustrating that the board was contributing to the combustion process, alongside the firebrands. It was found however, that the initial smoldering of the firebrand pile is reduced when deposited on the WRC, as opposed to being deposited on the inert substrate. The MCE profiles from these WRC tests were calculated based on the total CO and CO_2 production from firebrand and WRC because MCE is a global descriptor of the combustion process. These MCE profiles either started below or quickly dropped to a value below the mean MCE value, calculated from the Kaowool tests, which represented the contribution of just the firebrands. This suggests that the FB–WRC system, on average under all testing conditions, initially contributes to heat production in a hybrid–smoldering/flaming state, however transitions into more intense smoldering as the test progresses. The decrease in the average MCE profiles occurred within the first 60 seconds of a test, which was also the time range when the flaming ignitions of the WRC board were visually observed to initiate. Knowing this, a secondary analysis of the tests where the WRC board ignited was conducted to investigate possible identification of these ignitions.

Criterion for the identification of flaming ignition of the WRC board was defined as the HRR profile for a single test increasing above 0 kW m^{-2} within the first 60 seconds after the wind tunnel was sealed. Of the tests where gas analysis data was accurately collected and ignition of the WRC board was observed, 80% were identified with this criterion. Despite this, the time of ignition could not be accurately determined therefore it was difficult to conclude if this overall identification method using the HRR profiles was adequate to be used in future works.

4.2 Future Work

Based on the results of this study, future work could use the average back surface temperature profiles from both the Kaowool PM and WRC substrate tests for all five testing conditions in an inverse heat transfer analysis, such as a finite element analysis, to obtain average heat flux profiles from the firebrand pile onto the two substrates. The heat flux profiles from the WRC tests can then be used in pyrolysis models to predict the ignition and burning of the wooden decking material.

To improve the accuracy and reliability in the exhaust flow analysis, a better base line that represents the contribution of the firebrands when deposited on a thick specimen with similar heat transfer processes and similar thermal properties as the WRC board is needed. Some flaming ignition events on the surface of the WRC board could not be identified as the thick WRC board absorbed more heat from the firebrands then the thin Kaowool insulation. This then decreases the temperature of the brands, the decomposition rate and subsequent production CO and CO_2 of the firebrand pile when deposited on the WRC board. Since these average CO and CO_2 mass production rate profiles on the Kaowool substrate were used to subtract out the contributions of the firebrand pile from the WRC tests, this artificially created a minimum CO_2 mass production rate needed from the flames to be detected within the first 60 seconds.

Future studies should also investigate other WUI construction materials such as Douglas fir, Japanese Cedar, Oriented Strand Board (OSB), and Pressure–treated lumber. Understanding how these other materials behave under firebrand exposure, as compared to the WRC selected in this study, could highlight possible solutions to the ignition of structures by the exposure of firebrands in the WUI. Also, future studies should investigate the other three, more common, firebrand accumulation zones: in–between the crevices of each board, within the gaps between a board and an exterior wall, and within a reentrant corner. These other two accumulation zones, although likely more complex, could again highlight possible solutions to the ignition of structures by the exposure of firebrands.

Appendix A: Kaowool Back Surface Temperature Profiles

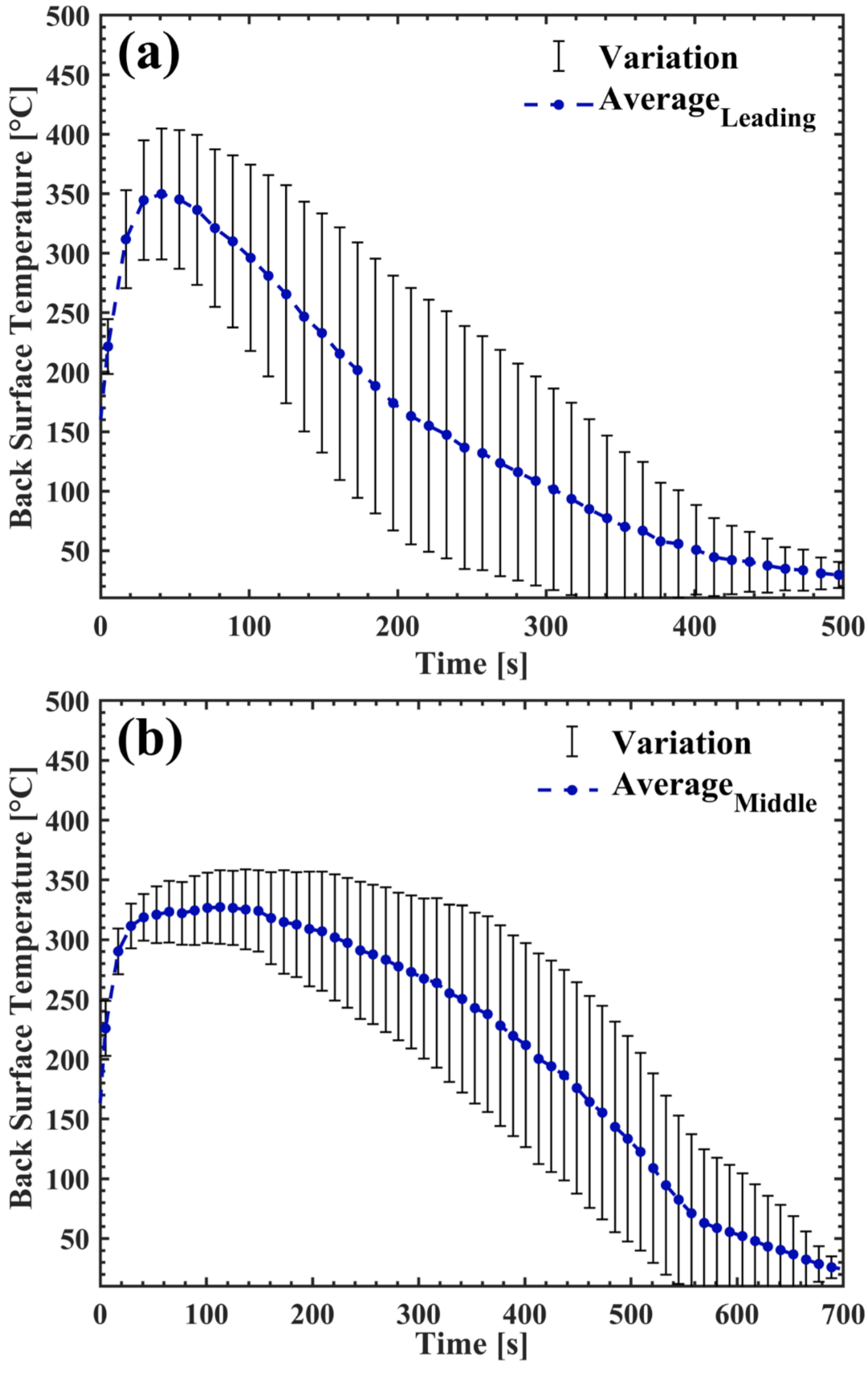

Figure A.1: Average leading (a) and middle (b) zone temperature profiles, considering six tests, for the 0.06 g cm^{-2} coverage density at the 2.4 m s^{-1} air flow velocity on the Kaowool substrate.

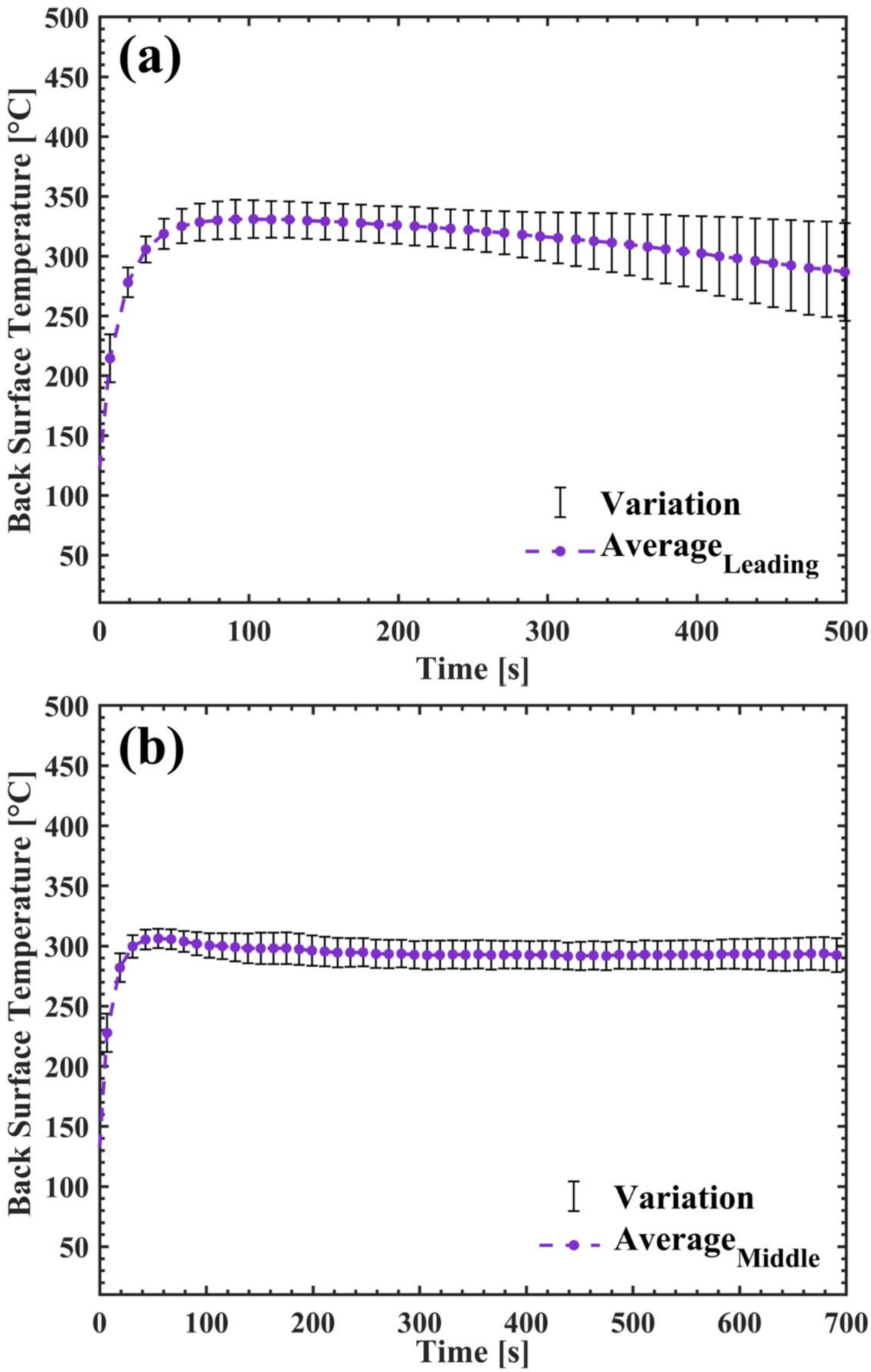

Figure A.2: Average leading (a) and middle (b) zone temperature profiles, considering six tests, for the 0.16 g cm^{-2} coverage density at the 0.9 m s^{-1} air flow velocity on the Kaowool substrate.

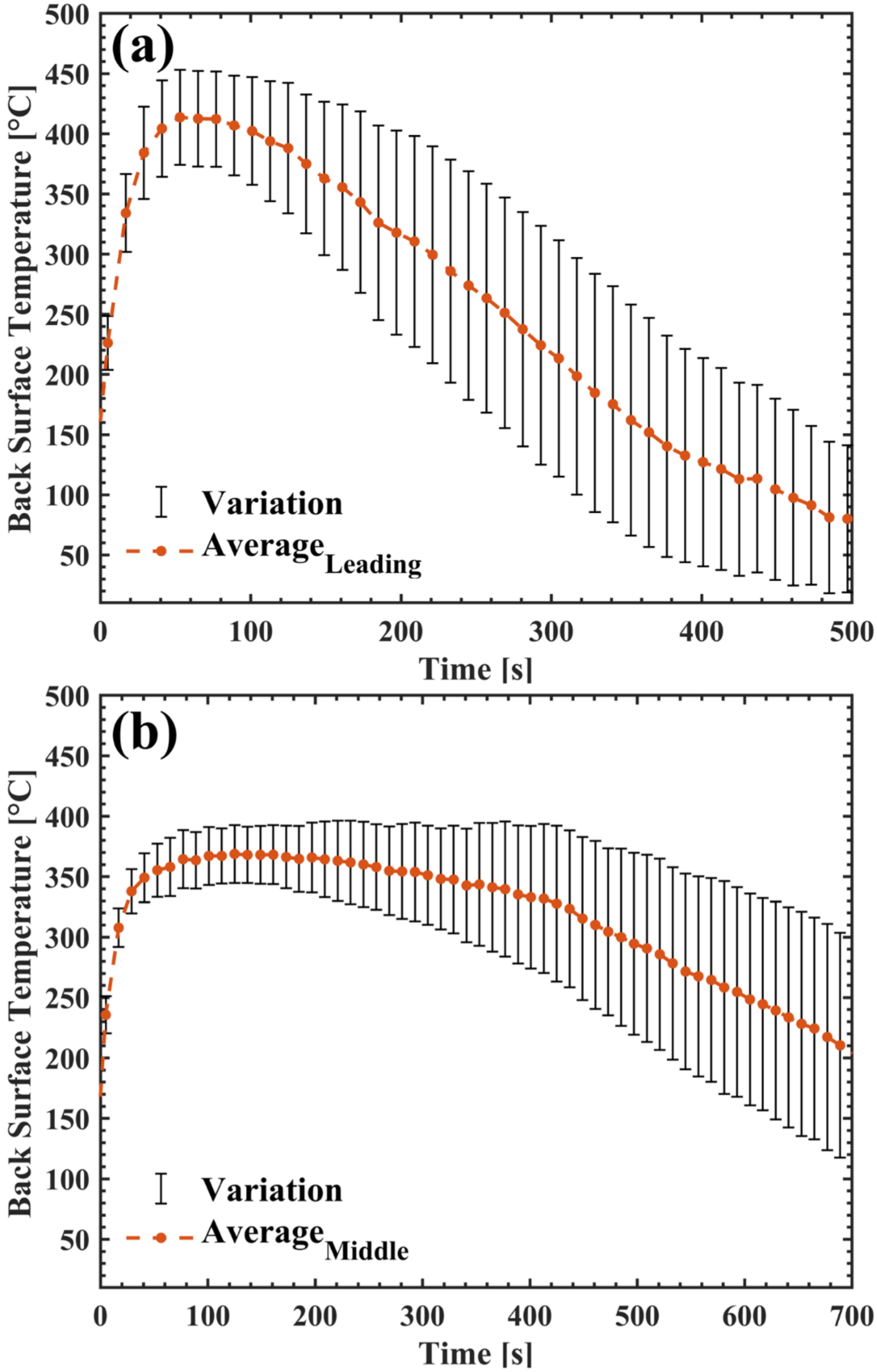

Figure A.3: Average leading (a) and middle (b) zone temperature profiles, considering six tests, for the 0.16 g cm^{-2} coverage density at the 2.4 m s^{-1} air flow velocity on the Kaowool substrate.

Appendix B: WRC Back Surface Temperature Profiles

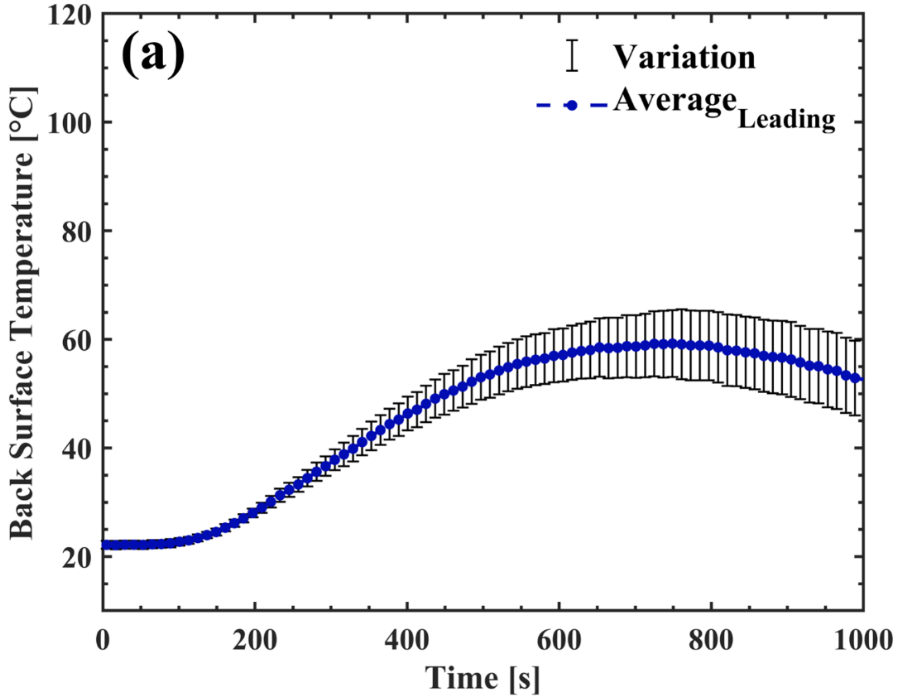

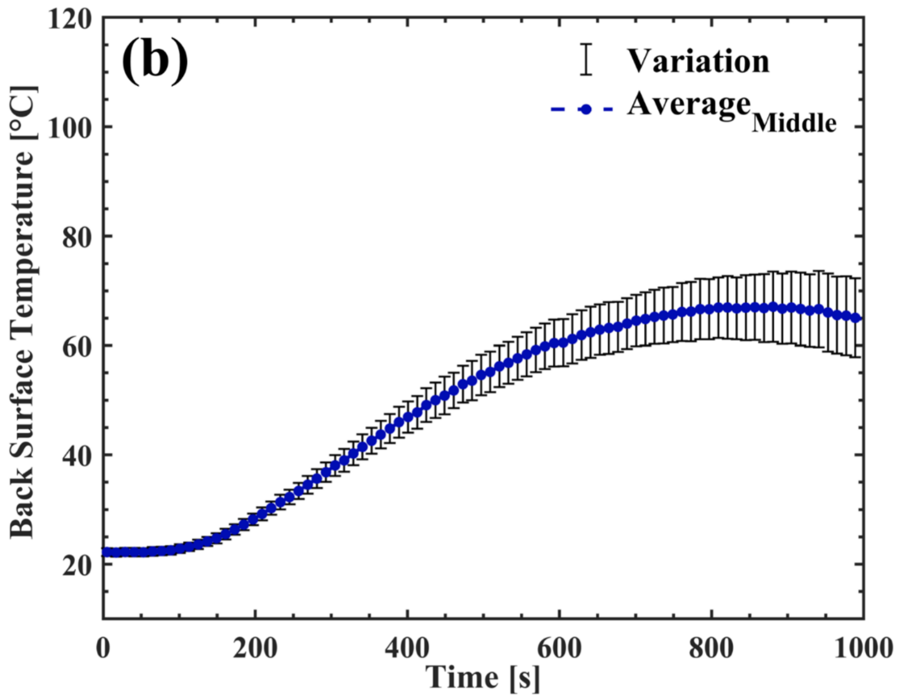

Figure B.1: Average leading (a) and middle (b) zone temperature profiles, considering six tests, for the 0.06 g cm^{-2} coverage density at the 2.4 m s^{-1} air flow velocity on the WRC substrate.

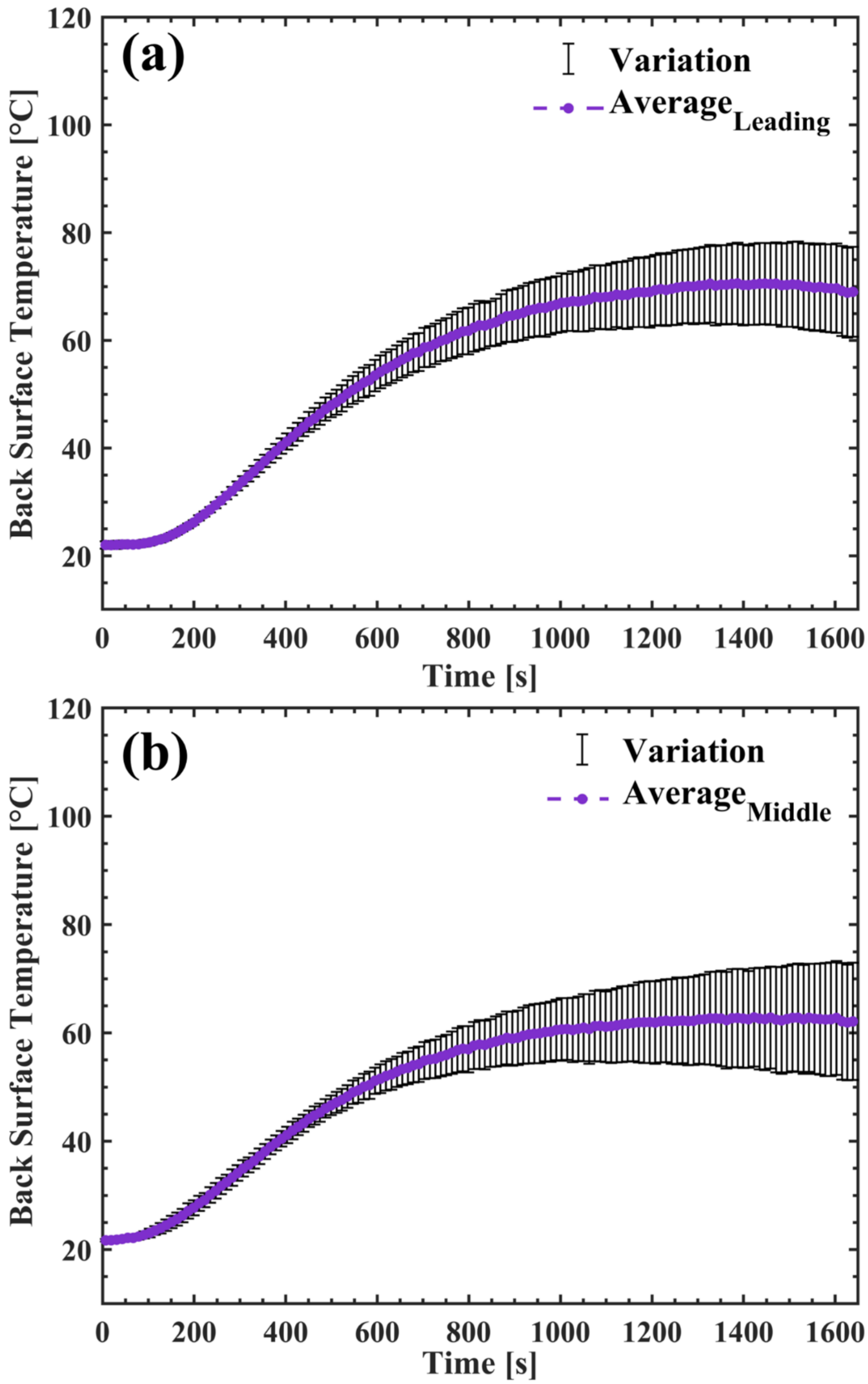

Figure B.2: Average leading (a) and middle (b) zone temperature profiles, considering six tests, for the 0.16 g cm^{-2} coverage density at the 0.9 m s^{-1} air flow velocity on the WRC substrate.

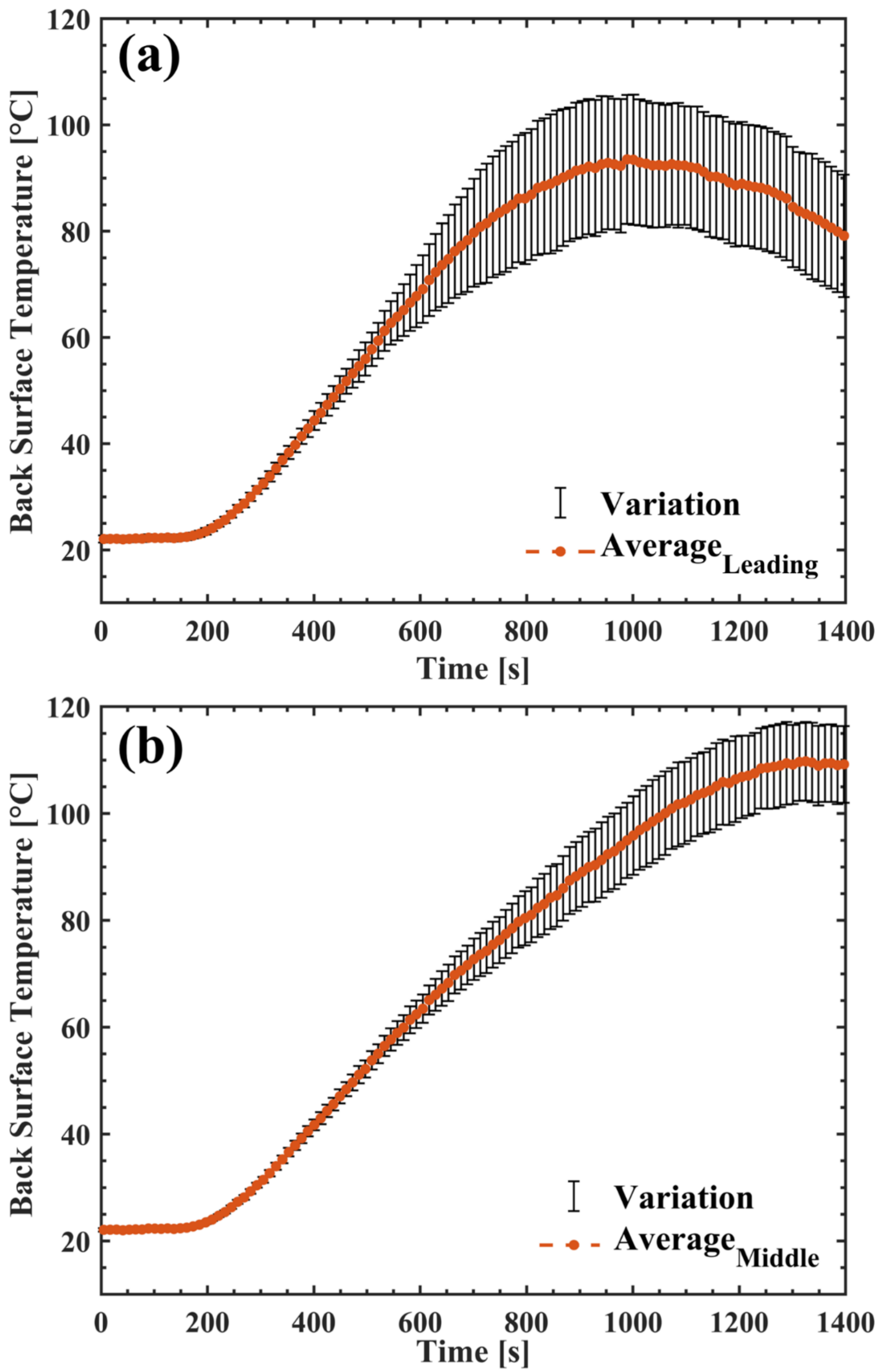

Figure B.3: Average leading (a) and middle (b) zone temperature profiles, considering six tests, for the 0.16 g cm^{-2} coverage density at the 2.4 m s^{-1} air flow velocity on the WRC substrate.

Appendix C: Kaowool Exhaust Flow Analysis Profiles

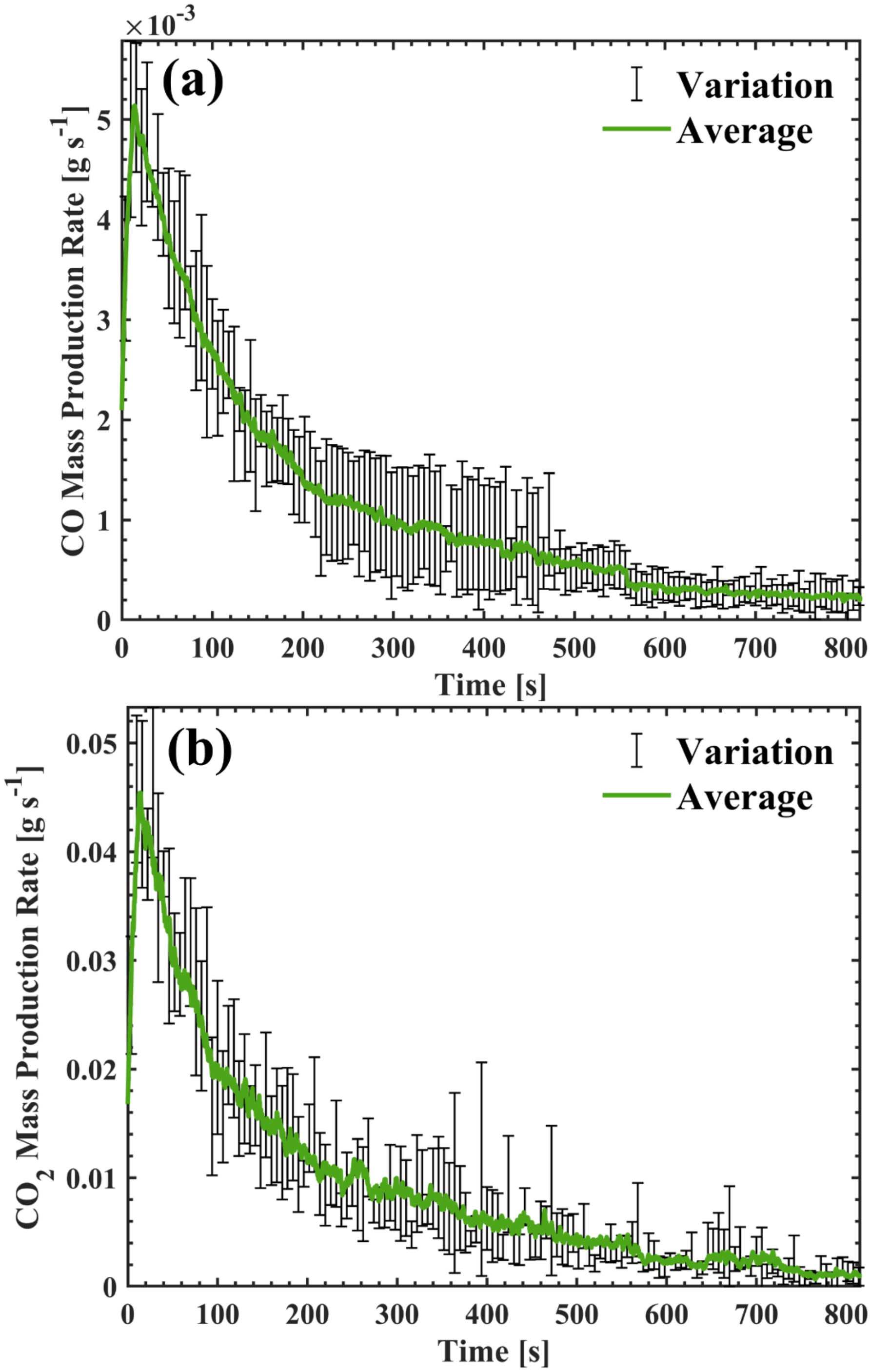

Figure C.1: Average CO (a) and CO_2 (b) mass production rate profiles for the 0.06 g cm^{-2} coverage density, 1.4 m s^{-1} air flow velocity condition on the Kaowool substrate. These profiles consider nine tests.

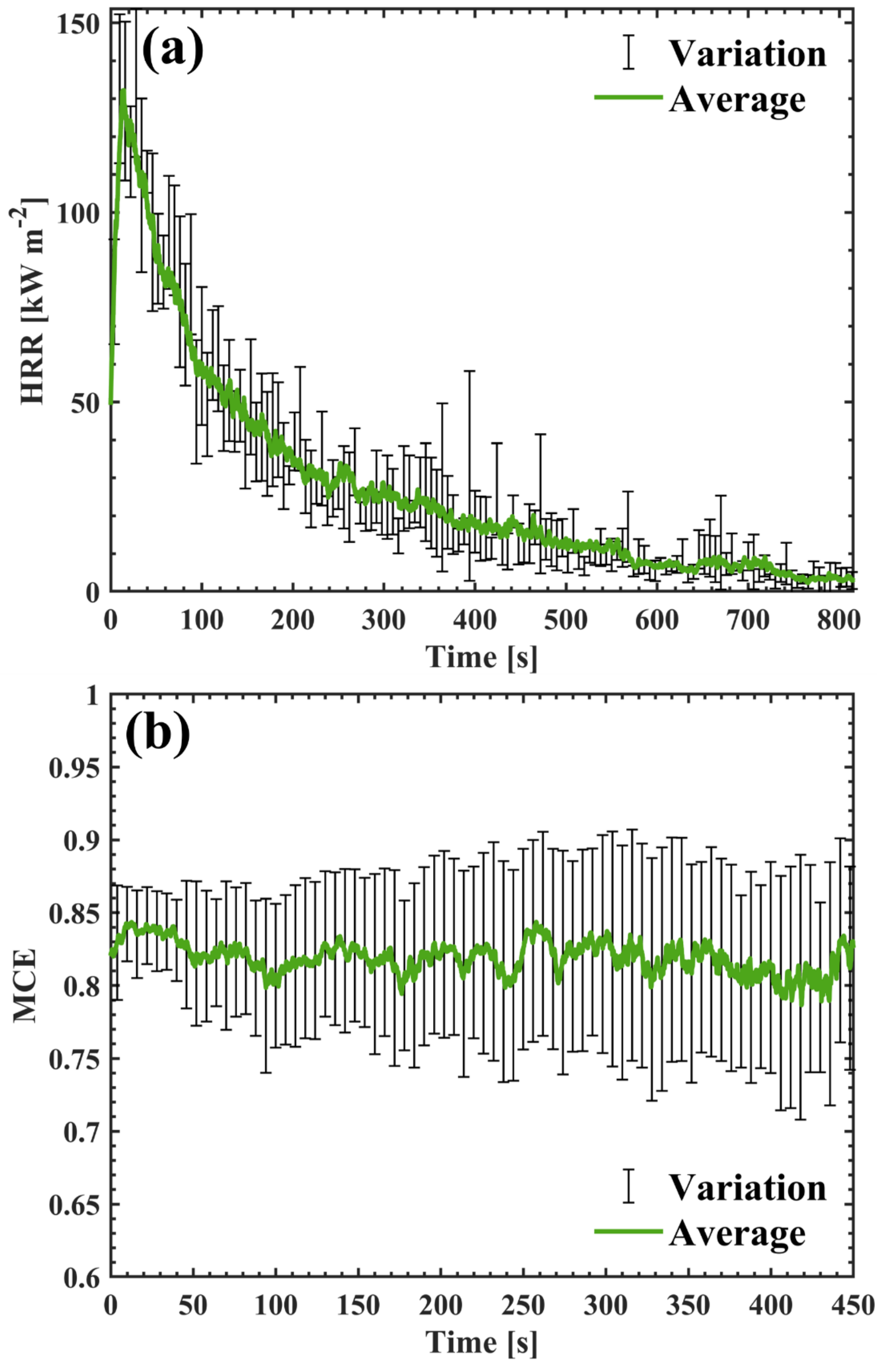

Figure C.2: Average Heat Release Rate (a) and Modified Combustion Efficiency (b) profiles for the 0.06 g cm^{-2} coverage density, 1.4 m s^{-1} air flow velocity condition on the Kaowool substrate. These profiles consider nine tests.

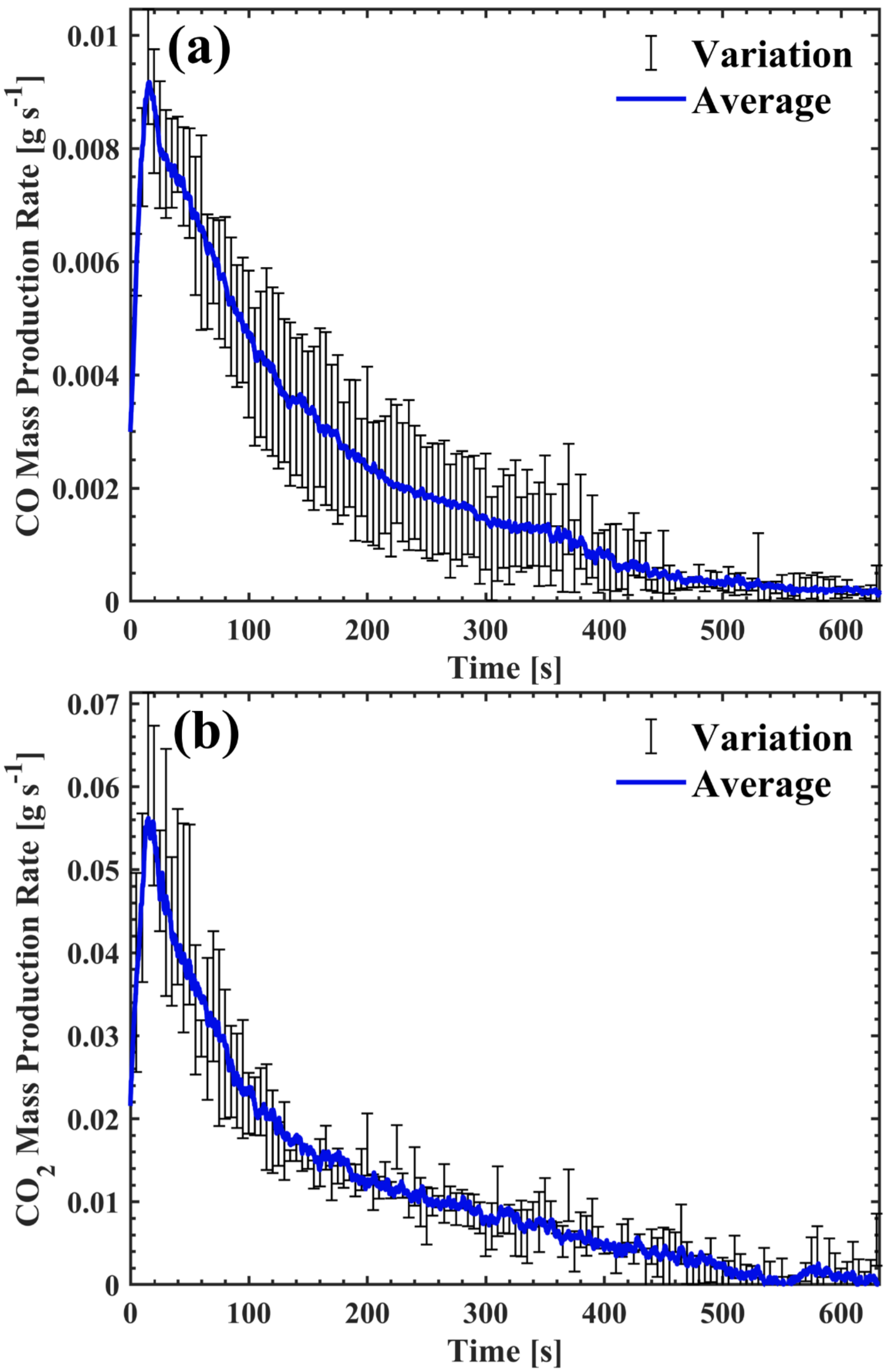

Figure C.3: Average CO (a) and CO_2 (b) mass production rate profiles for the 0.06 g cm^{-2} coverage density, 2.4 m s^{-1} air flow velocity condition on the Kaowool substrate. These profiles consider nine tests.

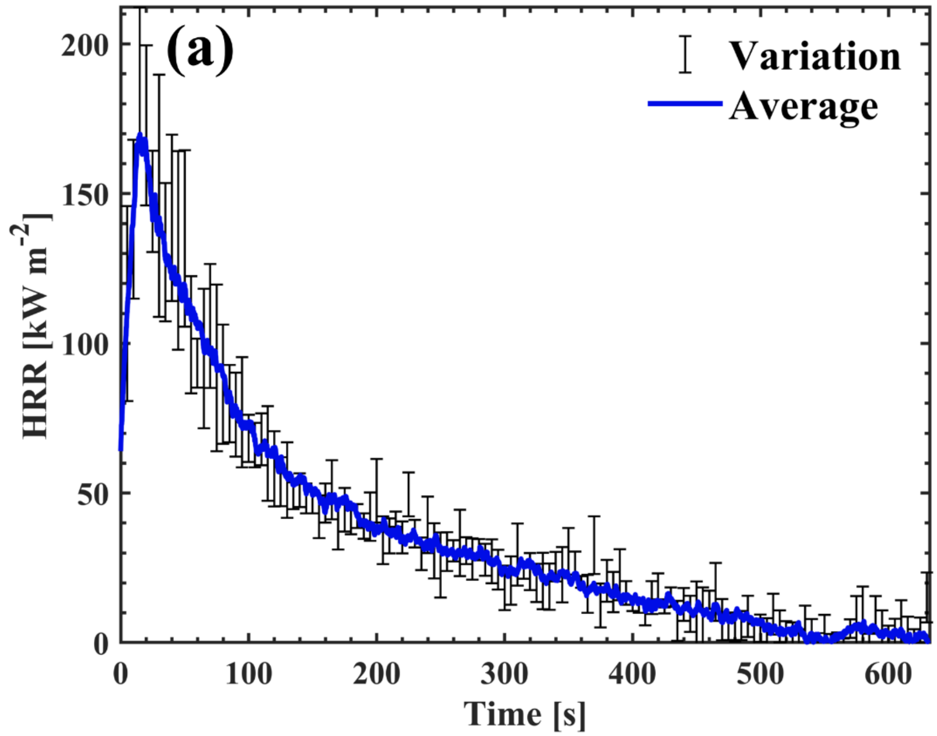

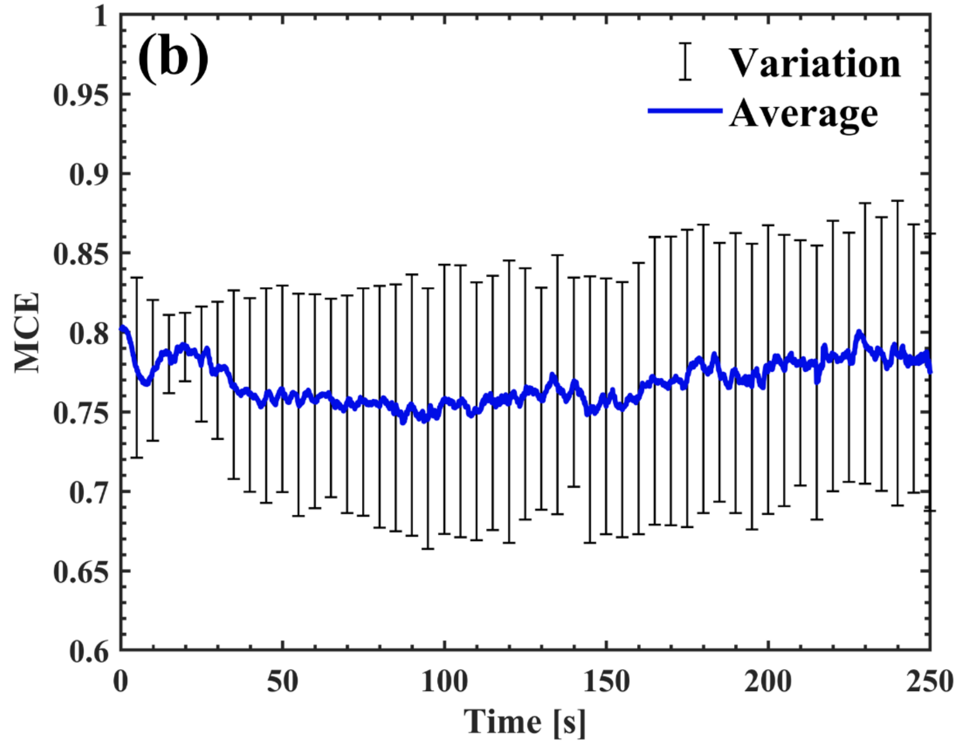

Figure C.4: Average Heat Release Rate (a) and Modified Combustion Efficiency (b) profiles for the 0.06 g cm^{-2} coverage density, 2.4 m s^{-1} air flow velocity condition on the Kaowool substrate. These profiles consider nine tests.

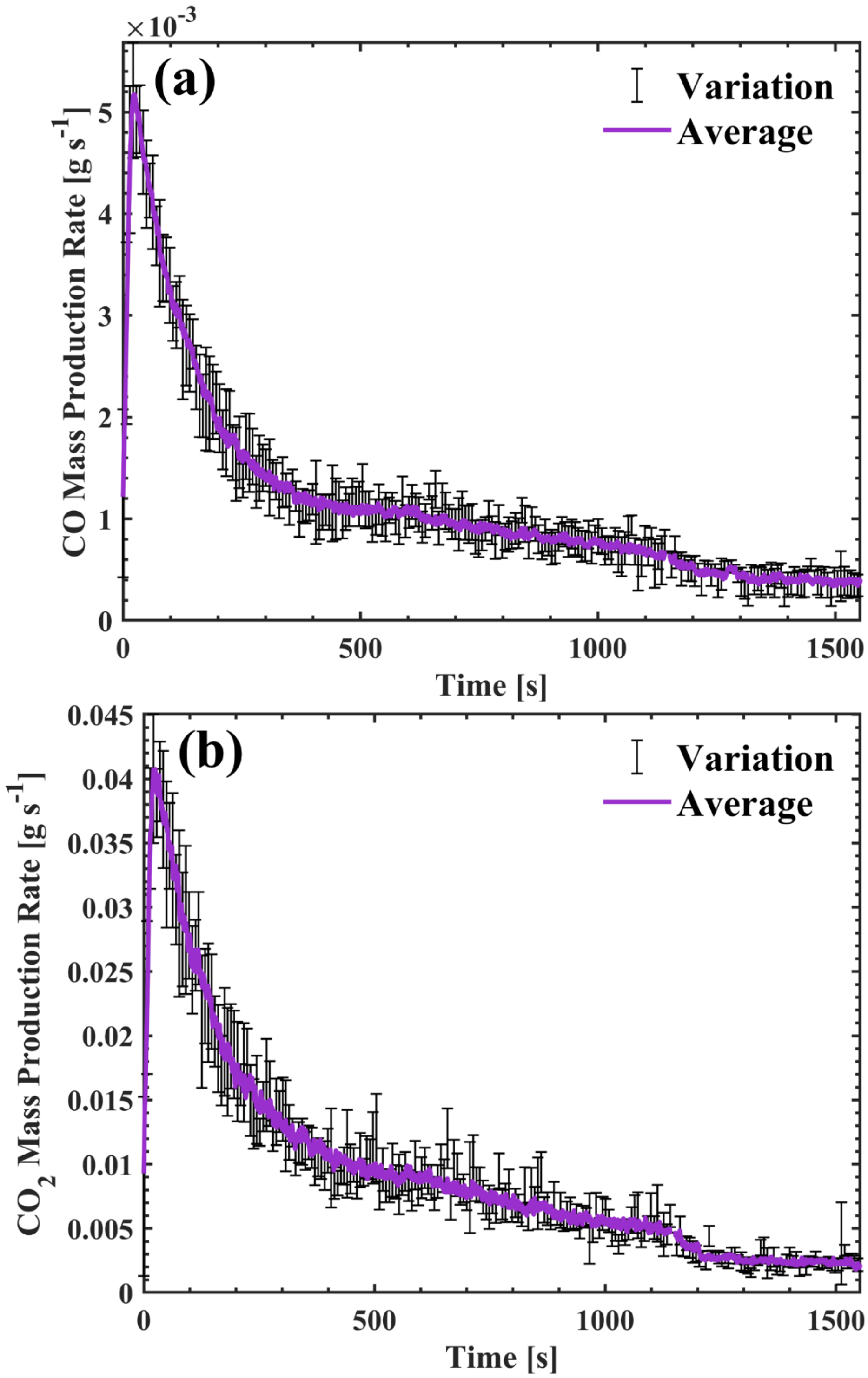

Figure C.5: Average CO (a) and CO_2 (b) mass production rate profiles for the 0.16 g cm^{-2} coverage density, 0.9 m s^{-1} air flow velocity condition on the Kaowool substrate. These profiles consider nine tests.

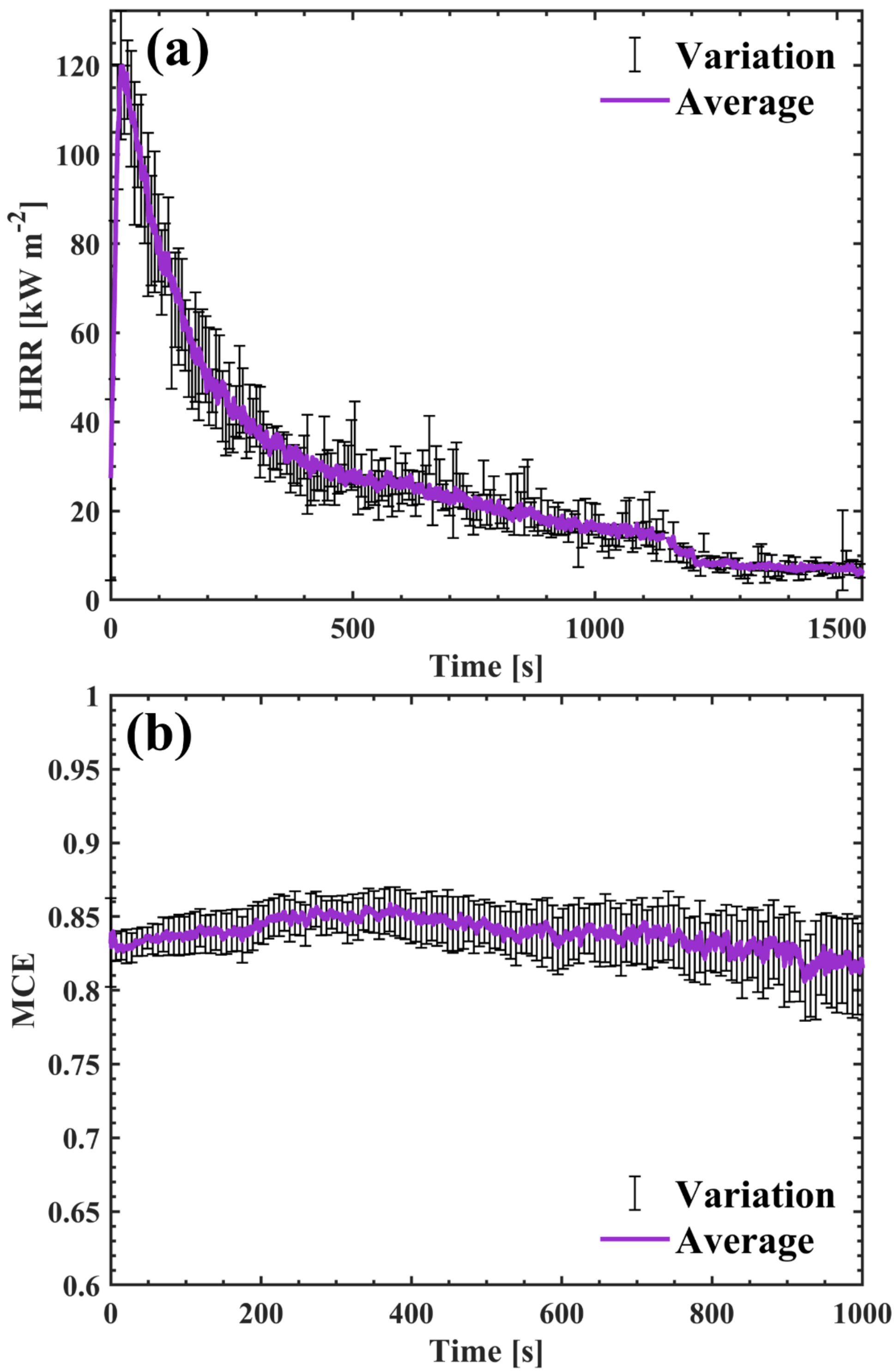

Figure C.6: Average Heat Release Rate (a) and Modified Combustion Efficiency (b) profiles for the 0.16 g cm^{-2} coverage density, 0.9 m s^{-1} air flow velocity condition on the Kaowool substrate. These profiles consider nine tests.

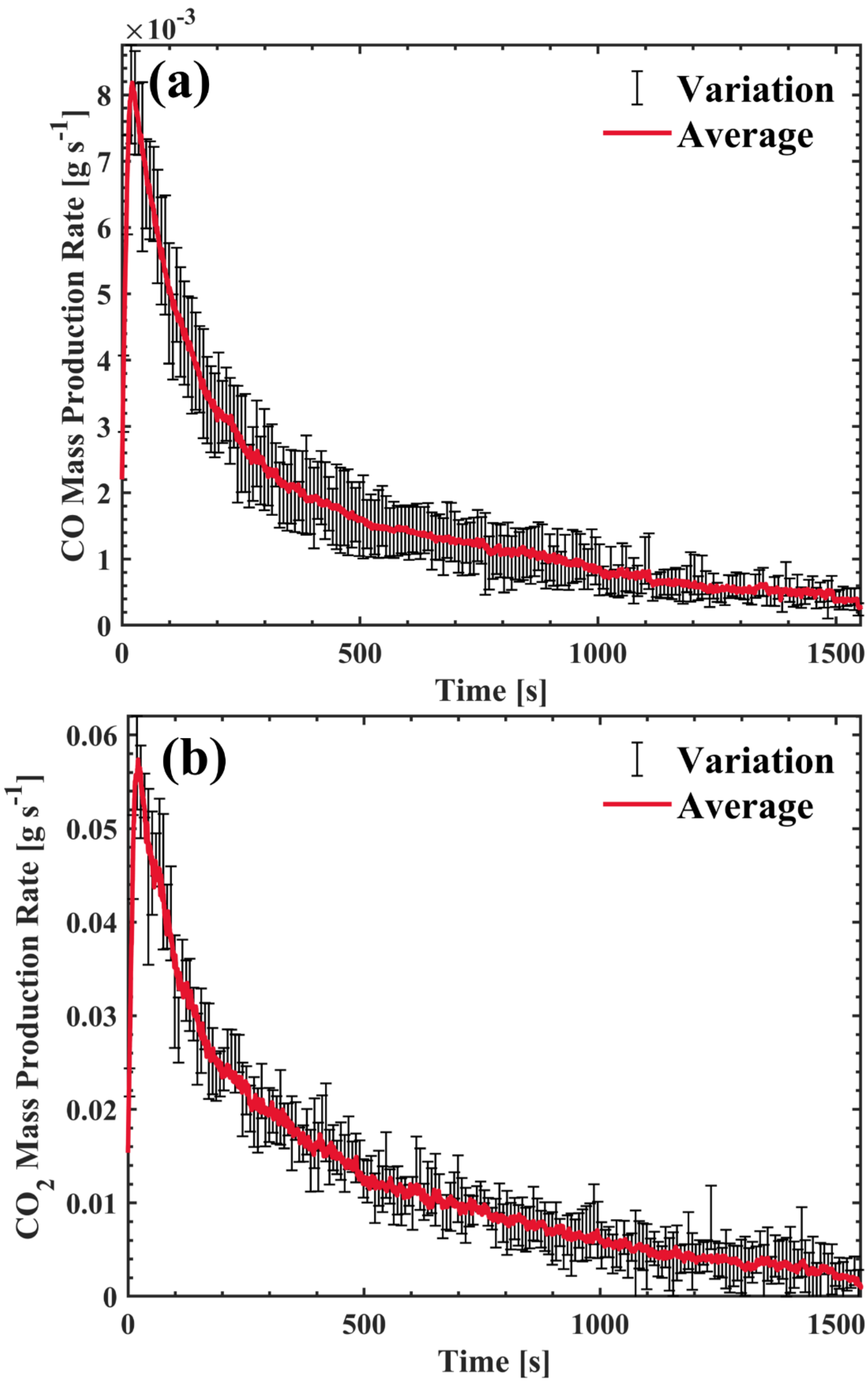

Figure C.7: Average CO (a) and CO_2 (b) mass production rate profiles for the 0.16 g cm^{-2} coverage density, 1.4 m s^{-1} air flow velocity condition on the Kaowool substrate. These profiles consider nine tests.

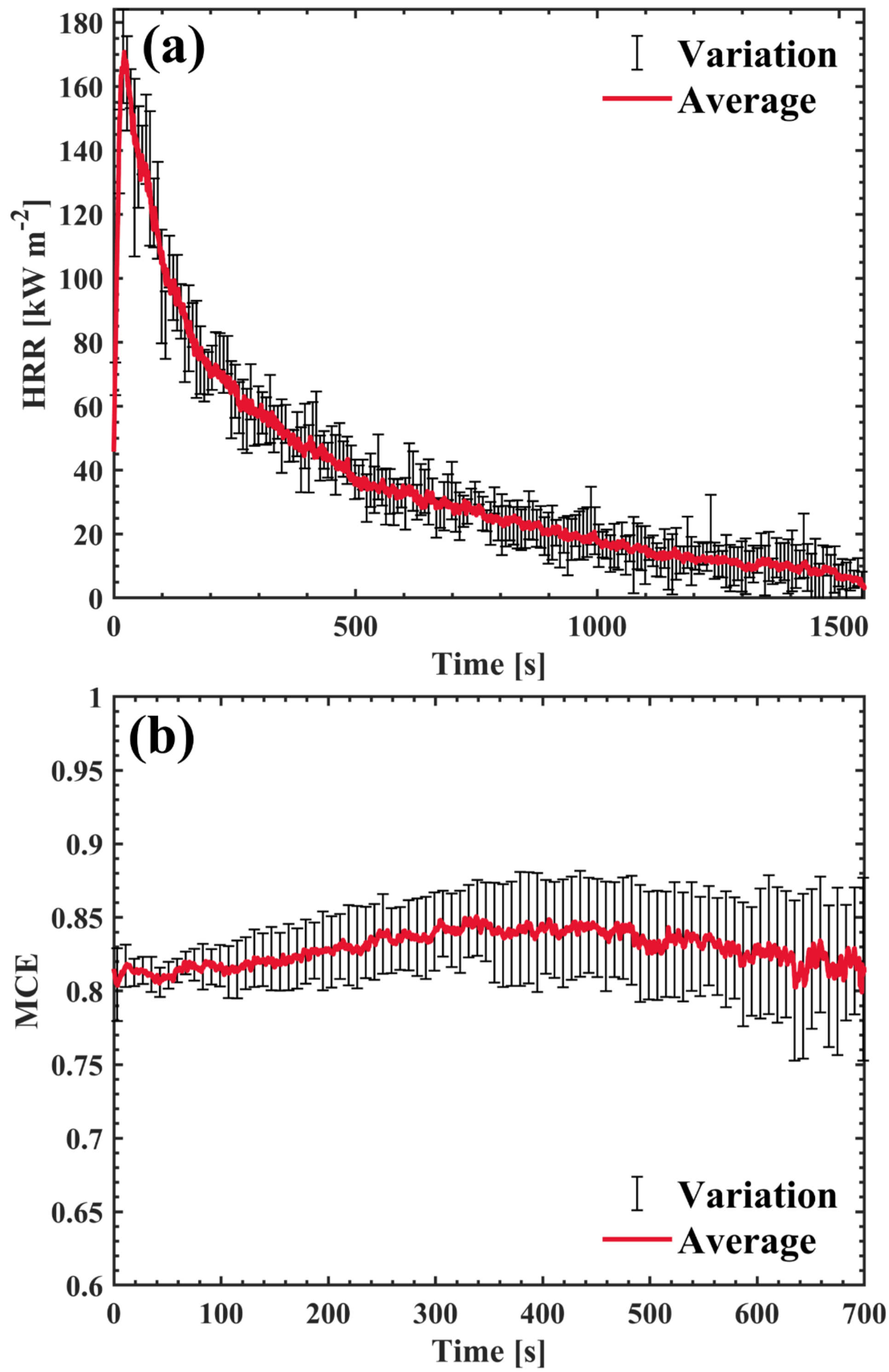

Figure C.8: Average Heat Release Rate (a) and Modified Combustion Efficiency (b) profiles for the 0.16 g cm^{-2} coverage density, 1.4 m s^{-1} air flow velocity condition on the Kaowool substrate. These profiles consider nine tests.

Appendix D: WRC Exhaust Flow Analysis Profiles

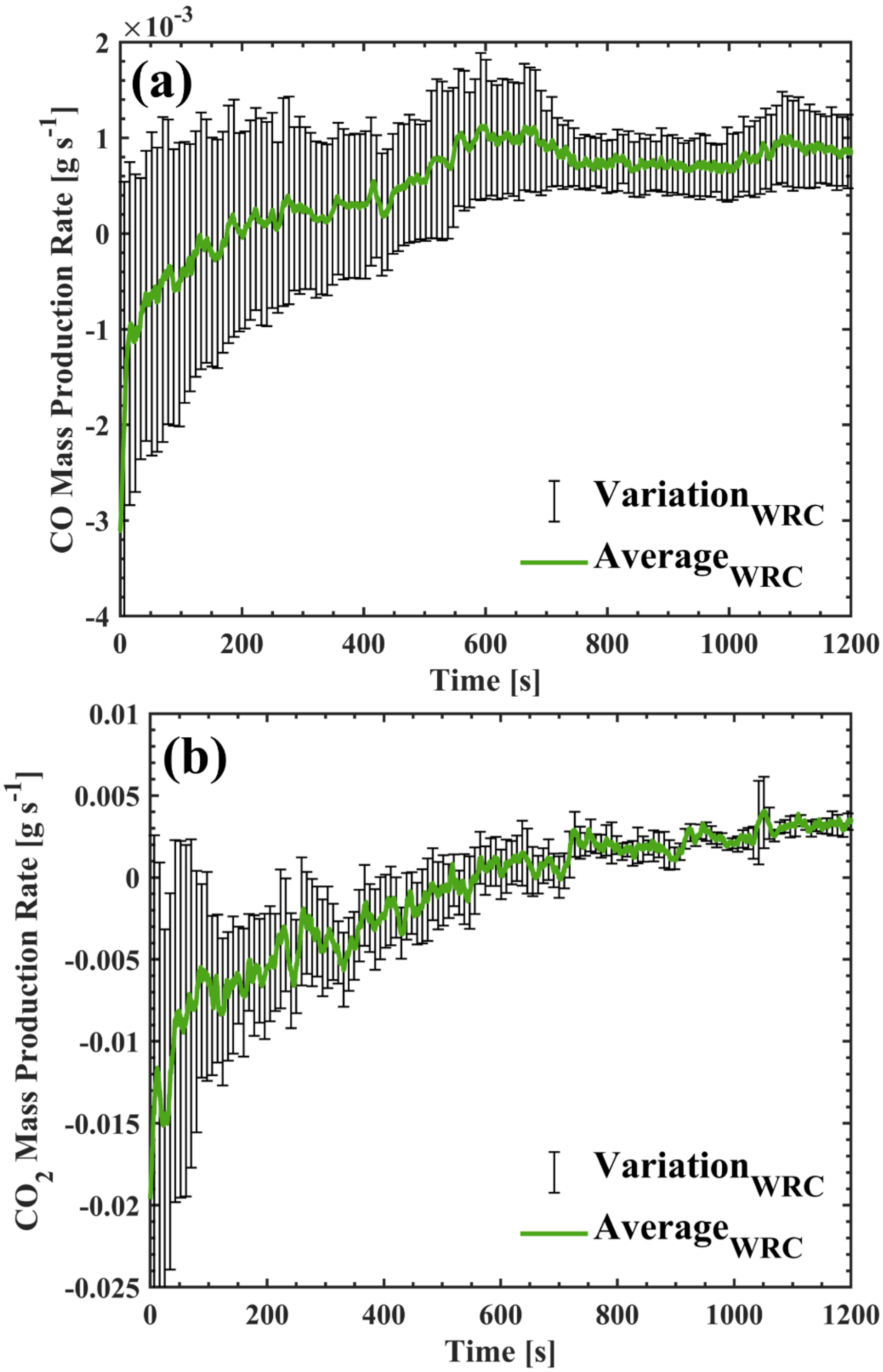

Figure D.1: Average CO (a) and CO_2 (b) mass production rate profiles of the WRC substrate for the 0.06 g cm^{-2} coverage density, 1.4 m s^{-1} air flow velocity condition, considering seven tests.

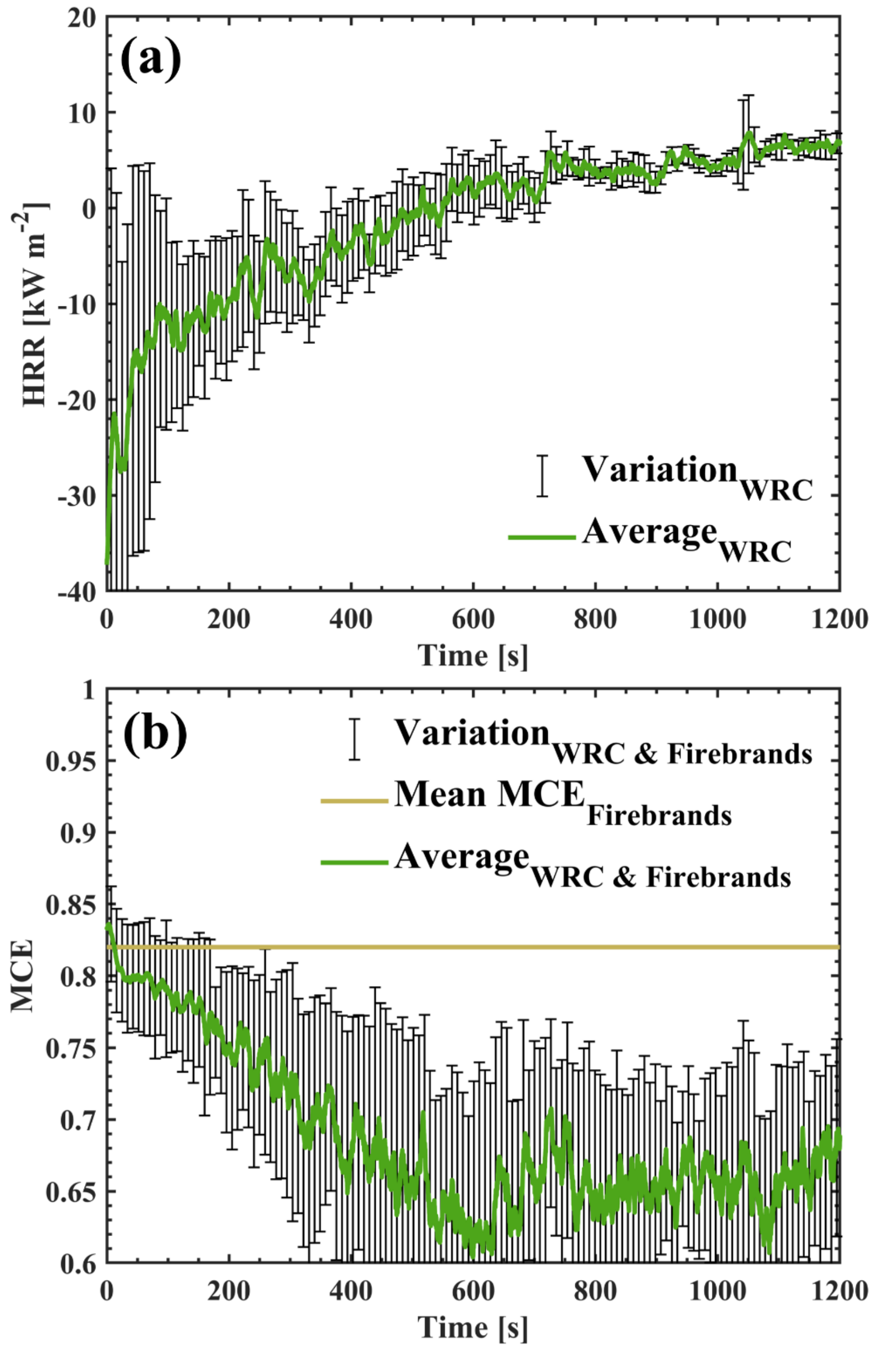

Figure D.2: Average Heat Release Rate (a) of the WRC board, and Modified Combustion Efficiency (b) profiles for the 0.06 g cm^{-2} coverage density, 1.4 m s^{-1} air flow velocity condition, considering seven tests. Note the MCE is for contribution of both the firebrands and WRC, and the mean MCE of the firebrands from the Kaowool tests is plotted in gold.

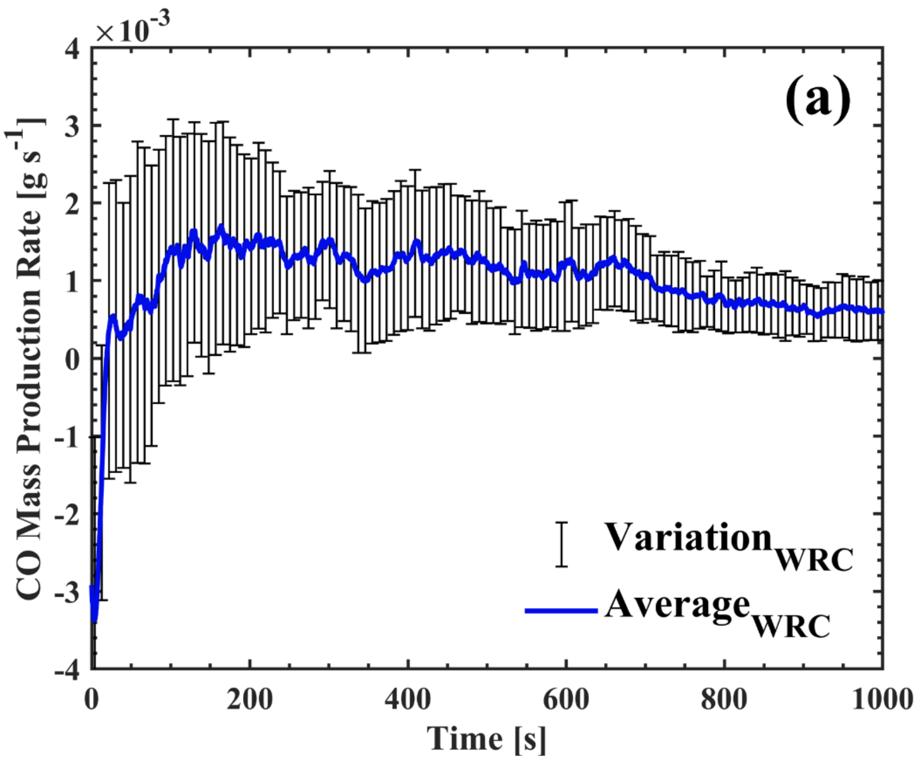

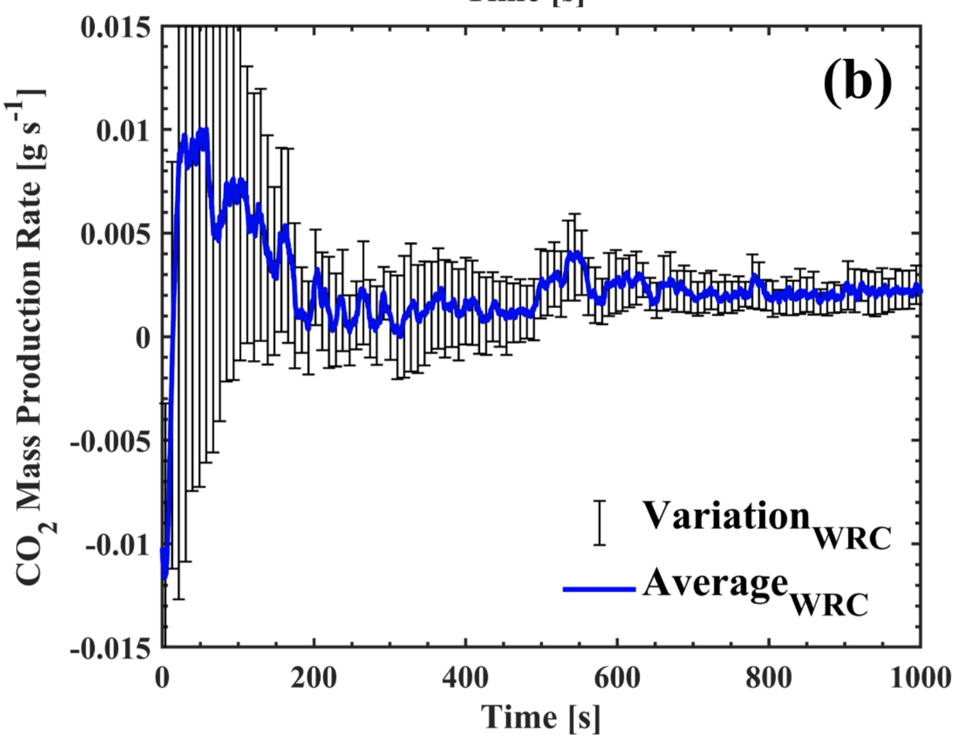

Figure D.3: Average CO (a) and CO_2 (b) mass production rate profiles of the WRC substrate for the 0.06 g cm^{-2} coverage density, 2.4 m s^{-1} air flow velocity condition, considering seven tests.

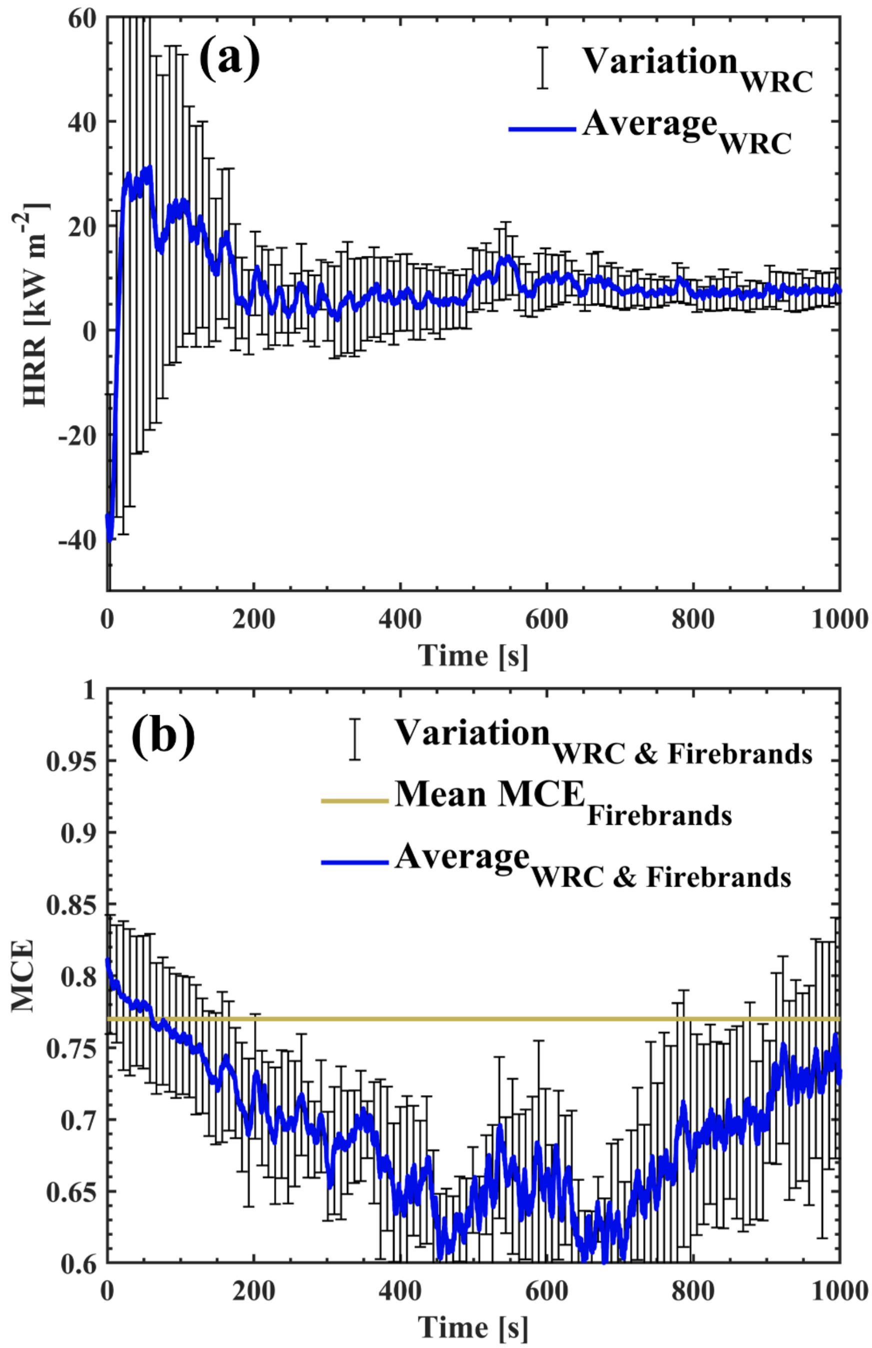

Figure D.4: Average Heat Release Rate (a) of the WRC board, and Modified Combustion Efficiency (b) profiles for the 0.06 g cm^{-2} coverage density, 2.4 m s^{-1} air flow velocity condition, considering seven tests. Note the MCE is for contribution of both the firebrands and WRC, and the mean MCE of the firebrands from the Kaowool tests is plotted in gold.

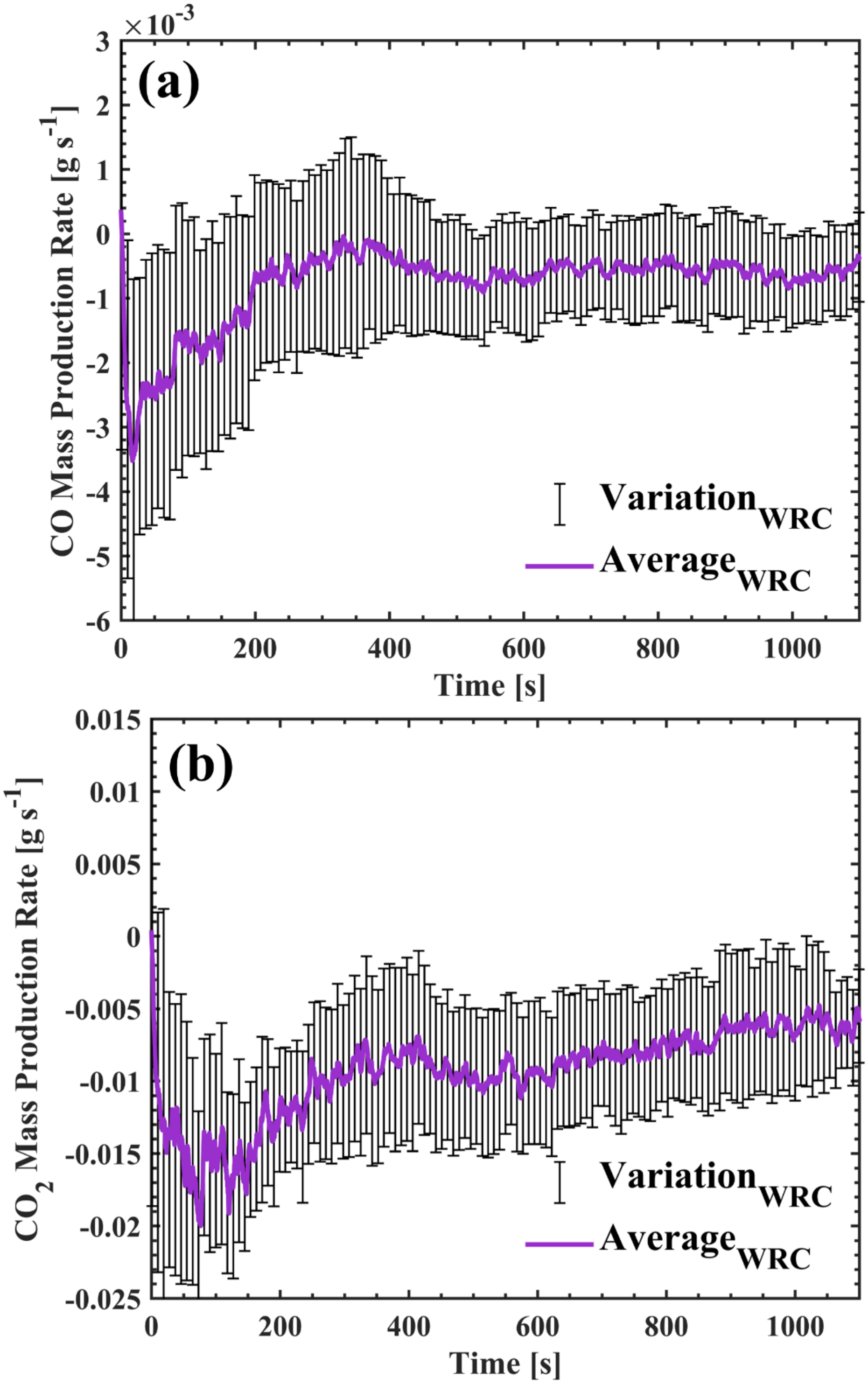

Figure D.5: Average CO (a) and CO_2 (b) mass production rate profiles of the WRC substrate for the 0.16 g cm^{-2} coverage density, 0.9 m s^{-1} air flow velocity condition, considering nine tests.

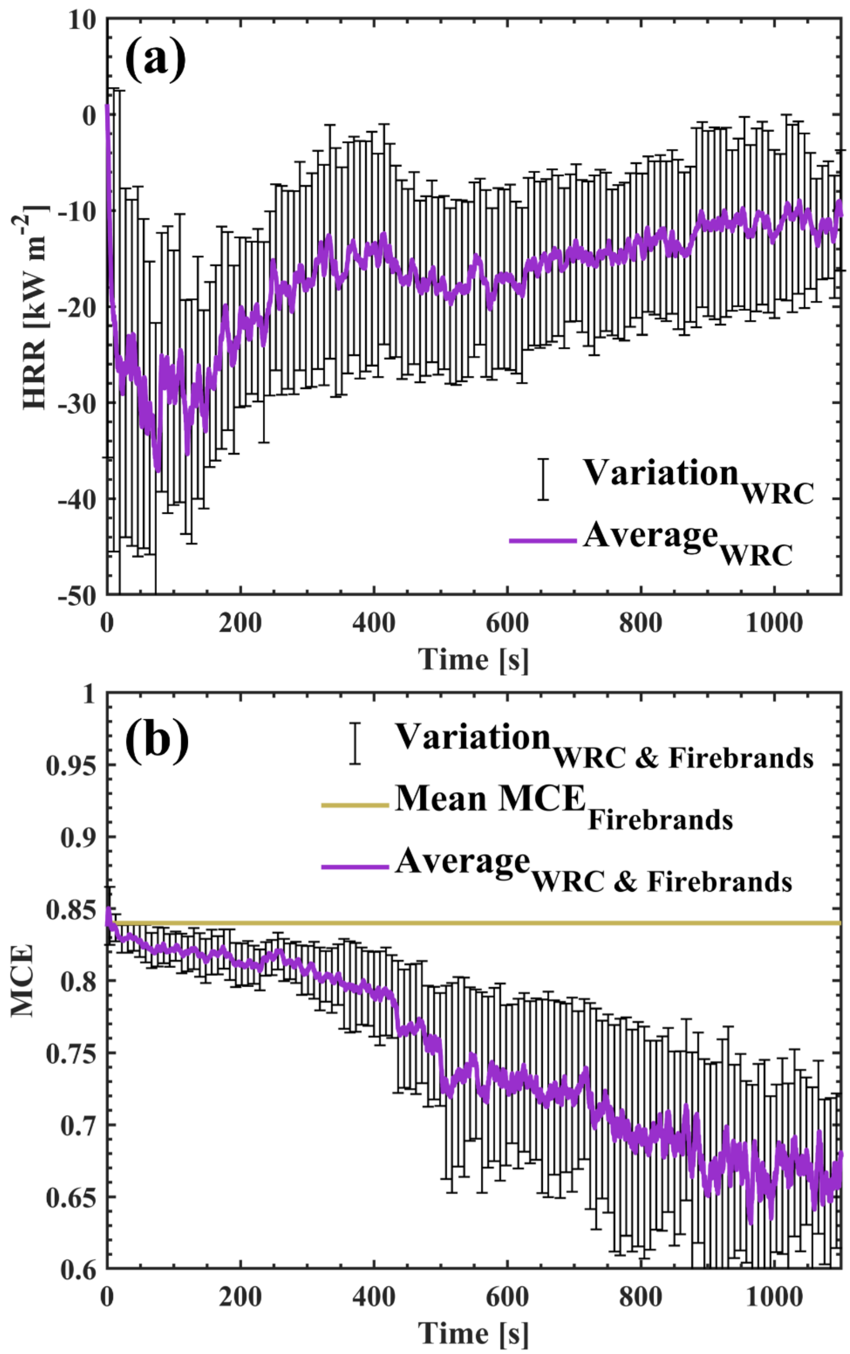

Figure D.6: Average Heat Release Rate (a) of the WRC board, and Modified Combustion Efficiency (b) profiles for the 0.16 g cm^{-2} coverage density, 0.9 m s^{-1} air flow velocity condition, considering nine tests. Note the MCE is for contribution of both the firebrands and WRC, and the mean MCE of the firebrands from the Kaowool tests is plotted in gold.

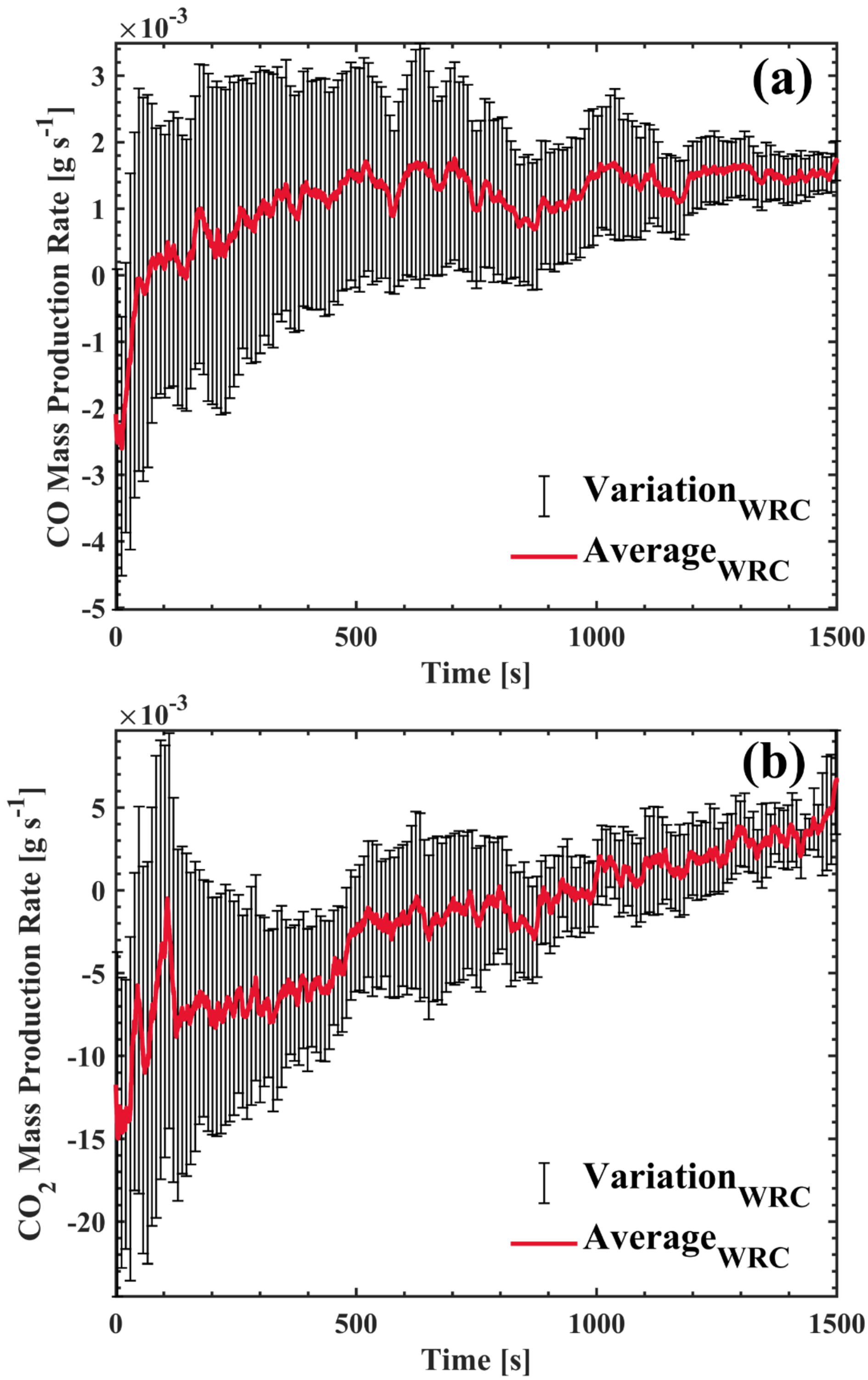

Figure D.7: Average CO (a) and CO_2 (b) mass production rate profiles of the WRC substrate for the 0.16 g cm^{-2} coverage density, 1.4 m s^{-1} air flow velocity condition, considering seven tests.

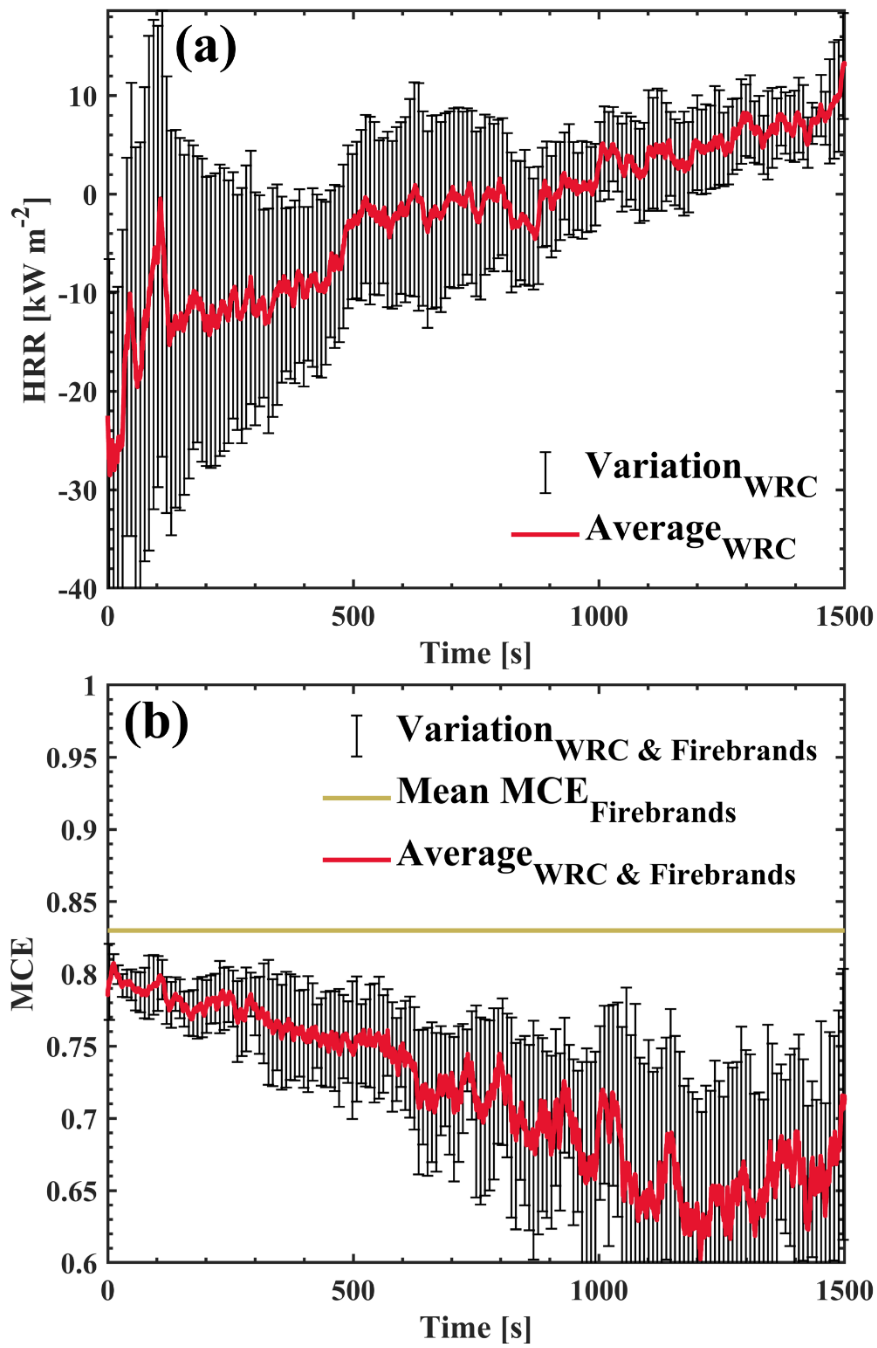

Figure D.8: Average Heat Release Rate (a) of the WRC board, and Modified Combustion Efficiency (b) profiles for the 0.16 g cm^{-2} coverage density, 1.4 m s^{-1} air flow velocity condition, considering seven tests. Note the MCE is for contribution of both the firebrands and WRC, and the mean MCE of the firebrands from the Kaowool tests is plotted in gold.

Bibliography

[1] U.S. Fire Administration. (2021). What is the WUI? [online] Available at: https://www.usfa.fema.gov/wui/what-is-the-wui.html.

[2] Thompson, C. (2001) *Urban Wildland Interface Communities Within the Vicinity of Federal Lands That Are at High Risk From Wildfire*. Fed Reg 66(3):751-777.

[3] Quarles, S. L. (2012) Vulnerabilities of Buildings to Wildfire Exposures. pp 1–13. https://surviving-wildfire.extension.org/vulnerabilities-of-buildings-to-wildfire-exposures/

[4] Caton, S.E. *et al*. (2017) "Review of Pathways for Building Fire Spread in the Wildland Urban Interface Part I: Exposure Conditions," *Fire Technology*, 53(2), pp. 429–473. doi: 10.1007/s1069410.3801/IAFSS.FSS.9–1165016–0589–z.

[5] Hoover, K. (2021) Wildfire Statistics. [online] Crsreports.congress.gov. Available at: https://crsreports.congress.gov/product/pdf/IF/IF10244.

[6] Donovan, G. H. and Brown, T. C. (2007) "Be Careful What You Wish for: The Legacy of Smokey Bear," *Frontiers in Ecology and the Environment*, 5(2), pp. 73–79.

[7] Weise *et al.* (2018) “Surface to Crown Transition,” *Encyclopedia of Wildfires and Wildland-Urban Interface (WUI) Fires*, [online] pp.1–5. Available at: https://escholarship.org/content/qt3rf9w6x3/qt3rf9w6x3_noSplash_a6e6daf6561fcf71e20d06b68b970880.pdf?t=ptcrd8#:~:text=Ground%20fires%20burn%20the%20matted [Accessed 14 Sep. 2021].

[8] Kraaij, T., Baard, J. A., Arndt, J., Vhengani, L. and van Wilgen, B. W. (2018) An Assessment of Climate, Weather, and Fuel Factors Influencing a Large, Destructive Wildfire in the Knysna Region, South Africa. *Fire Ecology*, 14(2).

[9] Hollingsworth, Lawen (2012) *Structures Lost to Wildfire 1999–2011*. 10.13140/RG.2.1.2330.6724.

[10] www.fire.ca.gov. (2021) *Dixie Fire - Update for September 13, 2021, | Welcome to CAL FIRE*. [online] Available at: https://www.fire.ca.gov/incidents/2021/7/13/dixie-fire/updates/1d8c6ebf-d3ae-4692-a781-0b43b03bc585/ [Accessed 13 Sep. 2021].

[11] Maranghides, A., Link, E., Mell, W. "Ruddy, Hawks, S., Wilson, M., Brewer, W., Brown, C., Vihnaneck, B. and Walton, W. D. (2021). A Case Study of the Camp Fire – Fire Progression Timeline. [online] Available at: https://nvlpubs.nist.gov/nistpubs/TechnicalNotes/NIST.TN.2135.pdf.

[12] Quarles, S., Leschak, P., Cowger, R., Worley, K., Brown, R. and Iskowitz, C. (2012) Lessons Learned from Waldo Canyon: Fire Adapted Communities

Mitigation Assessment Team Findings. Insurance Institute for Business and Home Safety.

[13] Maranghides, A., McNamara, D., Vihnanek, R., Restaino, J. and Leland, C. (2015) A Case Study of a Community Affected by the Waldo Fire Event Timeline and Defensive Actions. NIST Technical Note 1910. National Institute of Standards and Technology.

[14] Cohen, J. D. and Stratton, R. D. (2008) Home Destruction Examination: Grass Valley Fire, Lake Arrowhead, CA. United States Department of Agriculture, R5–TP–026b, (June).

[15] Maranghides, A. and Mell, W. (2009) A Case Study of a Community Affected by the Witch and Guejito Fires. Technical Note (TN 1635). National Institute of Standards and Technology, Gaithersburg, Maryland.

[16] Michael J. Karter, Jr. NFPA Reports: U.S. Fire Loss for 2007 NFPA, www.nfpa.org.

[17] B. Bankoff, U. Lubken, J. Sand (2012) Flammable Cities: Urban Conflagration and the Making of the Modern World, University of Wisconsin Press, Madison, WI.

[18] Thousands Flee South Korea Wildfire, Wildland firefighter. http://www.wildlandfirefighter.com/2019/04/05/thousands-flee-south-korea-wildfire/#gref [Accessed 20 May 2021]

[19] Walls, R., Oliver, G. and Eksteen, R. (2017) "Informal Settlement Fires in South Africa: Fire Engineering Overview and Full–Scale Tests on 'shacks,'" *Fire Safety Journal*, 91, pp. 997–1006. doi: 10.1016/j.firesaf.2017.03.061.

[20] DMFRS (2015) Western Cape Strategic Framework for Fire and Burn Injury Prevention, Western Cape Disaster Management & Fire Rescue Services.

[21] AP NEWS. (2021) Fire on Cape Town's Table Mountain under control, smoldering. [online] Available at: https://apnews.com/article/sports-mountains-general-news-fires-cape-town-834fa0886893575d7e6c6671daf3f426.

[22] Table Mountain fire: Historic buildings destroyed in Cape Town (2021) *BBC News*. [online] 18 Apr. Available at: https://www.bbc.com/news/world-africa-56793317.

[23] NPR.org. (n.d.) Fast–Moving Fire on Table Mountain Destroys South African Landmarks, History. [online] Available at: https://www.npr.org/2021/04/19/988640656/fast-moving-fire-on-table-mountain-destroys-south-african-landmarks-history.

[24] Tedim, F. *et al*. (2013) "Exploring the Occurrence of Mega–Fires in Portugal," *Forest Ecology and Management*, 294, pp.86–96. doi: 10.1016/j.foreco.2012.07.031.

[25] Viegas, D.X. (2018) "Wildfires in Portugal." *Fire Research*, 2, 52.

[26] CNN, Elinda Labropoulou and Amy Woodyatt (2021) *Greece Faces "Disaster of Unprecedented Proportions" as Wildfires Ravage the Country*. [online] CNN. Available at: https://www.cnn.com/2021/08/09/europe/greece-wildfire-warning-climate-intl/index.html [Accessed 12 Aug. 2021].

[27] Calkin, D. E., Cohen, J. D., Finney, M. A. and Thompson, M. P. (2014) How Risk Management Can Prevent Future Wildfire Disasters in the Wildland–Urban Interface. *Proceedings of the National Academy of Sciences*, USA, 111, pp.746–751. doi:10.1073/pnas.1315088111.

[28] Pellegrino J. L., Bryner N. P. and Johnsson, E. L. (2013) Wildland–urban Interface Fire Research Needs: Workshop Summary Report. doi: 10.6028/NIST.SP.1150.

[29] S. E. Caton and M. J. Gollner, "Laboratory Studies on the Generation of Firebrands from Cylindrical Wooden Dowels."

[30] Cohen, J. D. (1995) "Structure Ignition Assessment Model (SIAM)," *Biswell Symp. Fire Issues Solut. Urban Interface Wildl. Ecosyst.*, pp. 85–92.

[31] Ganteaume, A., Guijarro, M., Jappiot, M., Hernando, C., Lampin–Maillet, C., Pérez–Gorostiaga, P., Vega, J. A. (2011) Laboratory Characterization of Firebrands Involved in Spot Fires, *Annals of Forest Science*, 68: 531–541, doi: 10.1007/s13595–011–0056–4

[32] Potter, M. and Leonard, J. (2010) Spray System Design for Firebrand Attack–Research Findings and Discussion Paper. CSIRO–Sustainable Ecosystems, Report No. EP103159, pp. 1–27.

[33] Frontline. (2019) *Most Wildfire Damage Caused by Embers*. [online] Available at: https://www.frontlinewildfire.com/why-embers-cause-the-most-damage-in-wildfires/.

[34] Mell, W. E. *et al*. (2010) "The Wildland–Urban Interface Fire Problem – Current Approaches and Research Needs," *International Journal of Wildland Fire*, 19(2), pp. 238–251. doi: 10.1071/WF07131.

[35] Manzello, S. L. *et al*. (2020) "Role of Firebrand Combustion in Large Outdoor Fire Spread," *Progress in Energy and Combustion Science*, 76. doi: 10.1016/j.pecs.2019.100801.

[36] www.nwcg.gov. (n.d.). *Spotting Fire Behavior | NWCG*. [online] Available at: https://www.nwcg.gov/publications/pms437/crown-fire/spotting-fire-behavior.

[37] Cruz, M. G., Gould, J. S., Alexander, M. E., Sullivan, A. L., McCaw, W. L. and Matthews, S. (2015) *A Guide to Rate of Fire Spread Models for Australian Vegetation, CSIRO Land and Water*. ACT and AFAC Malborne, Vic, Australasian Fire and Emergency Service Authorities Council Limited, Commonwealth Scientific and Industrial Research Organization, Canberra, Australia, p.125.

[38] Hadden, R. M. *et al*. (2011) "Ignition of Combustible Fuel Beds by Hot Particles: An Experimental and Theoretical Study," *Fire Technology*, 47(2), pp. 341–355. doi: 10.1007/s10694–010–0181–x.

[39] Gollner, M. J. and Hakes, Raquel Sara Pilar (2017) *Thermal characterization of firebrand piles*. Dissertation. University of Maryland (College Park, Md.). doi: 10.13016/M2H70814D.

[40] Warey, A. (2018) "Influence of Thermal Contact on Heat Transfer from Glowing Firebrands," *Case Studies in Thermal Engineering*, 12, pp. 301–311. doi: 10.1016/j.csite.2018.04.018.

[41] Quarles, S. and Standohar, C. (2018) "Ignition Potential of Decks Subject to Ember Exposure."

[42] Hasburgh, L. E., Stone, D. S. and Zelinka, S. L. (2017) "Laboratory Investigation of Fire Transfer from Exterior Wood Decks to Buildings in the Wildland–Urban Interface," *Fire Technology*, 53(2), pp. 517–534. doi: 10.1007/s10694–016–0588–0.

[43] Manzello, S. L. and Suzuki, S. (2017) "Experimental Investigation of Wood Decking Assemblies Exposed to Firebrand Showers," *Fire Safety Journal*, 92, pp. 122–131. doi: 10.1016/j.firesaf.2017.05.019.

[44] Handy, R.M. (2012) WALDO CANYON FIRE: fire department releases home rebuilding guidelines. In: The gazette. Colorado Springs.

[45] Rein, G. (1984) “Smouldering Fires and Natural Fuels,” *Fire Phenomena and the Earth System: An Interdisciplinary Guide to Fire Science*, pp. 15–33, 2013, doi: 10.1002/9781118529539.ch2.

[46] Chien, Y. –C. *et al*. (2018) “Effects of Heat Treatment on the Chemical Compositions and Thermal Decomposition Kinetics of Japanese Cedar and Beech Wood,” *Polymer Degradation and Stability*, 158, pp. 220–227. doi: 10.1016/j.polymdegradstab.2018.11.003.

[47] Rein, G. (2009) “Smouldering Combustion Phenomena in Science and Technology,” *Int. Rev. Chem. Eng*., vol. 1, pp. 3–18.

[48] Shafizadeh, F., and DeGroot, W. F. (1976) “Combustion Characteristics of Cellulosic Fuels,” *Thermal Uses and Properties of Carbohydrates and Lignins* (F. Shafizadeh, K.V. Sarkanen, and D.A. Tillman, eds.). Academic Press, New York.

[49] Shafizadeh, F., and Chin, P. S. (1977) “Thermal Deterioration of Wood,” *Wood Technology: Chemical Aspects* (I.S. Goldstine, ed.), pp. 57–81. ACS Press, Washington, D.C.

[50] Tillman, D. A., Rossi, A. J. and Kitto, W. D. (1981) *Wood Combustion: Principles, Processes, and Economics*. New York: Academic Press.

[51] Ohlemiller, T. J. (2006) "Smoldering Combustion Propagation on Solid Wood," *Fire Safety Science Proc. Third Int. Symp*., pp. 565–574, doi: 10.4324/9780203973493.

[52] Rein, G. (2016) Smoldering Combustion. Chapter 19. In: *SFPE Handbook of Fire Protection Engineering*, 5th Ed., Ed: M.J. Hurley. pp. 581–603. Springer, New York.

[53] Suzuki, S. and Manzello, S. L. (2018) "Characteristics of Firebrands Collected from Actual Urban Fires," *Fire Technology*, 54(6), pp. 1533–1546. doi: 10.1007/s10694–018–0751–x.

[54] Manzello, S. L., Maranghides, A., Mell, W. E., Cleary, T. G., and Yang, J. C. (2006a) Firebrand Production from Burning Vegetation. *Forest Ecology and Management* 234: S119. doi: 10.1016/j.foreco.2006.08.160

[55] Manzello, S. L. and Foote, E. I. D. (2014) Characterizing Firebrand Exposure During Wildland–Urban Interface Fires: Results of the 2007 Angora Fire, *Fire Technology*, 50, 105–124.

[56] Vodvarka, F. J. (1969) Firebrand Field Studies—Final Report, IIT Research Institute, Chicago, IL

[57] Vodvarka, F. J. (1970) Urban Burns–Full–Scale Field Studies—Final Report, IIT Research Institute, Chicago, IL

[58] Hakes, R. S. P. *et al*. (2019) “Thermal Characterization of Firebrand Piles,” *Fire Safety Journal*, 104, pp. 34–42. doi: 10.1016/j.firesaf.2018.10.002.

[59] Gollner, M. J. and Salehizadeh, Hamed (2019) *Critical ignition conditions of structural materials by cylindrical firebrands.* Dissertation. University of Maryland (College Park, Md.).

[60] Tao, Z. *et al*. (2020) “Effect of Firebrand Size and Geometry on Heating from a Smoldering Pile Under Wind,” *Fire Safety Journal*. doi: 10.1016/j.firesaf.2020.103031.

[61] Gollner, M. J. and Babetta Duarte, Julia (2020) *Characterization of ignition conditions of decking assembly materials to smoldering firebrands*. dissertation. University of Maryland (College Park, Md.).

[62] Bearinger, E. D. *et al*. (2021) “Localized Heat Transfer from Firebrands to Surfaces,” *Fire Safety Journal*, 120. doi: 10.1016/j.firesaf.2020.103037.

[63] Manzello, S. L. and Suzuki, S. (2012) “The New and Improved NIST Dragon's Lair (Lofting and Ignition Research) Facility,” *Fire and Materials*, 36(8), pp. 623–635. doi: 10.1002/fam.1123.

[64] Hasburgh, L. E., Stone, D. S. and Zelinka, S. L. (2017) “Laboratory Investigation of Fire Transfer from Exterior Wood Decks to Buildings in the Wildland–Urban Interface,” *Fire Technology*, 53(2), pp. 517–534. doi: 10.1007/s10694–016–0588–0.

[65] Suzuki, S. and Manzello, S. L. (2021) "Ignition Vulnerabilities of Combustibles Around Houses to Firebrand Showers: Further Comparison of Experiments," *Sustainability*, 13(4), pp. 2136–2136. doi: 10.3390/su13042136.

[66] Manzello, S. L. and Suzuki, S. (2014) "Exposing Decking Assemblies to Continuous Wind–Driven Firebrand Showers," *Fire Safety Science*, vol. 11, pp. 1339–1352, doi: 10.3801/IAFSS.FSS.11–1339.

[67] Dowling, V. P. (1994) "Ignition of Timber Bridges in Bushfires," *Fire Safety Journal*, 22(2), pp. 145–168. doi: 10.1016/0379–7112(94)90070–1.

[68] Urban, J. L., Zak, C. D., and Fernandez–Pello, C. (2015) "Cellulose Spot Fire Ignition by Hot Metal Particles," *Proceedings of the Combustion Institute*, 35(3), pp. 2707–2714. doi: 10.1016/j.proci.2014.05.081.

[69] Fernandez–Pello, A. C. *et al*. (2015) "Spot Fire Ignition of Natural Fuel Beds by Hot Metal Particles, Embers, and Sparks," *Combustion Science and Technology*, 187(1–2), pp. 269–295. doi: 10.1080/00102202.2014.973953.

[70] Urban, J. L. *et al*. (2017) "Smoldering Spot Ignition of Natural Fuels by a Hot Metal Particle," *Proceedings of the Combustion Institute*, 36(2), pp. 3211–3218. doi: 10.1016/j.proci.2016.09.014.

[71] Urban, J. L., Zak, C. D., and Fernandez–Pello, C. (2018) "Spot Fire Ignition of Natural Fuels by Hot Aluminum Particles," *Fire Technology*, 54(3), pp. 797–808. doi: 10.1007/s10694–018–0712–4.

[72] Manzello, S. L. *et al*. (2006) “On the Ignition of Fuel Beds by Firebrands,” *Fire and Materials*, 30(1), pp. 77–87. doi: 10.1002/fam.901.

[73] Manzello, S. L. *et al*. (2006) “Ignition of Mulch and Grasses by Firebrands in Wildland – Urban Interface Fires,” *International Journal of Wildland Fire*, 15(3), pp. 427–427. doi: 10.1071/WF06031.

[74] Manzello, S. L., Park, S.–H. and Cleary, T. G. (2009) “Investigation on the Ability of Glowing Firebrands Deposited Within Crevices to Ignite Common Building Materials,” *Fire Safety Journal*, 44(6), pp. 894–900. doi: 10.1016/j.firesaf.2009.05.001.

[75] Manzello, S. L., Park, S.–H. and Cleary, T. G. (2010) “Development of Rapidly Deployable Instrumentation Packages for Data Acquisition in Wildland–Urban Interface (WUI) Fires,” *Fire Safety Journal*, 45(5), pp. 327–336. doi: 10.1016/j.firesaf.2010.06.005.

[76] Alexander, M. E., Cruz, M. G. (2006) Evaluating a Model for Predicting Active Crown Fire Rate of Spread Using Wildfire Observations. *Canadian Journal of Forest Research* 36, 3015–3028.

[77] Taylor, S. W., Wotton, B. M., Alexander, M. E., Dalrymple, G. N. (2004) Variation in Wind and Crown Fire Behavior in a Northern Jack Pine–black Spruce Forest. *Canadian Journal of Forest Research* 34(8), 1561–1576. doi:10.1139/X04–116.

[78] Garratt, J. R. (1992) *The Atmospheric Boundary Layer*. Cambridge: Cambridge University Press (Cambridge atmospheric and space science series).

[79] Stoliarov, S. I. and Said, Ahmed Osama Mohammed (2020) *Dynamics and hazards of cascading failure in lithium–ion cell arrays: analysis, passive mitigation, and active suppression*. Dissertation. University of Maryland (College Park, Md.).

[80] Karine (2013) *ICNIRP | Infrared (780 nm–1mm)*. [online] Icnirp.org. Available at: https://www.icnirp.org/en/frequencies/infrared/index.html.

[81] Swann, J. D. *et al*. (2017) "Controlled Atmosphere Pyrolysis Apparatus II (CAPA II): A New Tool for Analysis of Pyrolysis of Charring and Intumescent Polymers," *Fire Safety Journal*, 91, pp. 130–139. doi: 10.1016/j.firesaf.2017.03.038.

[82] Dukhan, N. *et al*. (2005) "One–Dimensional Heat Transfer Analysis in Open–Cell 10–Ppi Metal Foam," *International Journal of Heat and Mass Transfer*, 48(25), pp. 5112–5120. doi: 10.1016/j.ijheatmasstransfer.2005.07.012.

[83] Nakamura, H. (2009) "Frequency Response and Spatial Resolution of a Thin Foil for Heat Transfer Measurements Using Infrared Thermography," *International Journal of Heat and Mass Transfer*, 52(21–22), pp. 5040–5045. doi: 10.1016/j.ijheatmasstransfer.2009.04.019.

[84] Stoliarov, S. I. and McKinnon, Mark (2016) *A generalized methodology to characterize composite materials for pyrolysis models*. Dissertation. University of Maryland (College Park, Md.). doi: 10.13016/M2CB6S.

[85] WESTERN RED CEDAR QUICK FACTS (2013) *Real Cedar* [online]. Available at: https://www.jwlumber.com/wp-content/uploads/2020/10/WRC-Quick-Facts.pdf.

[86] Forest Products Laboratory (U.S.) (2010) *Wood handbook: Wood as an Engineering Material*. Centennial ed. Madison, Wis.: U.S. Dept. of Agriculture, Forest Service, Forest Products Laboratory (General technical report FPL, GTR-190). https://www.fpl.fs.fed.us/documnts/fplgtr/fpl_gtr190.pdf.

[87] Bergman, T. L. and Lavine, A. S. (2017). *Fundamentals of Heat and Mass Transfer*. 8th ed. New York: J. Wiley & Sons, Cop.

[88] Butler, K. *et al*. (2017) Flame Spread Along Fences Near a Structure in a Wind Field, Fire Safety 2017 – International Conference on Research and Advanced Technology in Fire Safety, Santander, –1, [online], https://tsapps.nist.gov/publication/get_pdf.cfm?pub_id=922111 (Accessed June 30, 2021)

[89] Butler, K. *et al*. (2020) Structure Vulnerability to Firebrands from Fences and Mulch, The Fire Continuum Conference, Missoula, MT, [online], https://tsapps.nist.gov/publication/get_pdf.cfm?pub_id=926248 (Accessed June 30, 2021)

[90] Maranghides, A. *et al*. (2021) Structure Separation Experiments Phase 1 Preliminary Test Plan, Technical Note (NIST TN), National Institute of Standards and Technology, Gaithersburg, MD. https://doi.org/10.6028/NIST.TN.2161.

[91] Yudong, Li and Drysdale, D. D. (1992) "Measurement of the Ignition Temperature of Wood," *AOFST 1*.

[92] Janssens, M. L., (1991) A Thermal Model For Piloted Ignition Of Wood Including Variable Thermophysical Properties. *Fire Safety Science 3*: 167–176. doi: 10.3801/IAFSS.FSS.3-167.

[93] American Society for Testing and Materials. ASTM D4442: *Standard Test Methods for Direct Moisture Content Measurement of Wood and Wood–Based Materials*, 2020.

[94] Çengel, Y. A. and Ghajar, A. J. (2015). *Heat and Mass Transfer Fundamentals and Applications*. 5th ed. New York: McGraw–Hill Education.

[95] Barlow, J. B., Rae, W. H. and Pope, A. (1999) *Low-Speed Wind Tunnel Testing*. 3rd ed. New York: Wiley.

[96] Gollner, M. J. et al. (2017) "The Effect of Flow and Geometry on Concurrent Flame Spread," *Fire Safety Journal*, 91, pp. 68–78. doi: 10.1016/j.firesaf.2017.05.007.

[97] Golabczak, M., Golabczak, A. and Konstantynowicz, A. (2017) “Calibration of Infrared (IR) Camera for Heat Generation Monitoring during Abrasive Electrodischarge Grinding (AEDG): kalibrierung Einer Ir–Kamera Für Die Wärmeerzeugungskontrolle Während des Abrasiven Elektroschleifens (aedg),” Materialwissenschaft und Werkstofftechnik, 48(5), pp. 335–341. doi: 10.1002/mawe.201600756.

[98] Bennett, G. A. and Briles, S. D. (1989) “Calibration Procedure Developed for IR Surface–Temperature Measurements,” *IEEE Transactions on Components, Hybrids, and Manufacturing Technology*, 12(4). doi: 10.1109/33.49034.

[99] Stolz, J., Boluk, Y. and Bindiganavile, V. (2019) “Wood Ash as a Supplementary Cementing Material in Foams for Thermal and Acoustic Insulation,” *Construction and Building Materials*, 215, pp. 104–113. doi: 10.1016/j.conbuildmat.2019.04.174.

[100] Janssens, M. (2016) Calorimetry. Chapter 27. In: *SFPE Handbook of Fire Protection Engineering*, 5th Ed., Ed: M.J. Hurley. pp. 905–951. Springer, New York.

[101] Biteau *et al*. (2008) Calculation Methods for the Heat Release Rate of Materials of Unknown Composition. *Fire Safety Science*: 1165–1176. doi: 10.3801/IAFSS.FSS.9–1165.

[102] Khan *et al*. (2016) Combustion Characteristics of Materials and Generation of Fire Products. Chapter 36. In: *SFPE Handbook of Fire Protection Engineering*, 5th Ed., Ed: M.J. Hurley. pp. 1143–1232. Springer, New York.

[103] Drysdale, D. D. (2016) Thermochemistry. Chapter 5. In: *SFPE Handbook of Fire Protection Engineering*, 5th Ed., Ed: M.J. Hurley. pp. 138–150. Springer, New York.

[104] National Institute of Standard and Technology (2021) NIST Chemistry WebBook. Methane. [online] Available at: https://webbook.nist.gov/cgi/cbook.cgi?Name=methane&Units=SI.

[105] S. P. Urbanski (2013) "Combustion Efficiency and Emission Factors for Wildfire–Season Fires in Mixed Conifer Forests of the Northern Rocky Mountains, Us," *Atmospheric Chemistry and Physics*, 13(14), pp. 7241–7262. doi: 10.5194/acp–13–7241–2013.

[106] Chen, L. W. *et al*. (2007) "Emissions from Laboratory Combustion of Wildland Fuels: Emission Factors and Source Profiles," *Environmental Science & Technology*, 41(12), pp. 4317–25.

[107] Stockwell, C. E. *et al*. (2016) "Field Measurements of Trace Gases and Aerosols Emitted by Peat Fires in Central Kalimantan, Indonesia, during the 2015 El Niño," *Atmospheric Chemistry and Physics*, 16, pp. 11711–11732. doi: 10.5194/acp–16–11711–2016.

[108] Akagi, S.K *et al*. (2011) “Emission Factors for Open and Domestic Biomass Burning for Use in Atmospheric Models,” *Atmospheric Chemistry and Physics*, 11(9), pp. 4039–4072. doi: 10.5194/acp–11–4039–2011.

[109] Urbanski, S. (2014) “Wildland Fire Emissions, Carbon, and Climate: Emission Factors,” *Forest Ecology and Management*, 317, pp. 51–60. doi: 10.1016/j.foreco.2013.05.045.

[110] Hu, Y. *et al*. (2018) “Review of Emissions from Smouldering Peat Fires and Their Contribution to Regional Haze Episodes,” *International Journal of Wildland Fire*, 27(5), pp. 293–312. doi: 10.1071/WF17084.

[111] Hu, Y. *et al*. (2019) “Transient Gas and Particle Emissions from Smouldering Combustion of Peat,” *Proceedings of the Combustion Institute*, 37(3), pp. 4035–4042. doi: 10.1016/j.proci.2018.06.008.

[112] Hu, Y *et al*. (2019) “Experimental Study of Moisture Content Effects on the Transient Gas and Particle Emissions from Peat Fires,” *Combustion and Flame*, 209, pp. 408–417. doi: 10.1016/j.combustflame.2019.07.046.

[113] ASTM E1354–17 (2017) *Standard Test Method for Heat and Visible Smoke Release Rates for Materials and Products Using an Oxygen Consumption Calorimeter*, ASTM International.